FIBRE DIFFRACTION REVIEW

THE CCP13 NEWSLETTER
Software Development for Fibre Diffraction

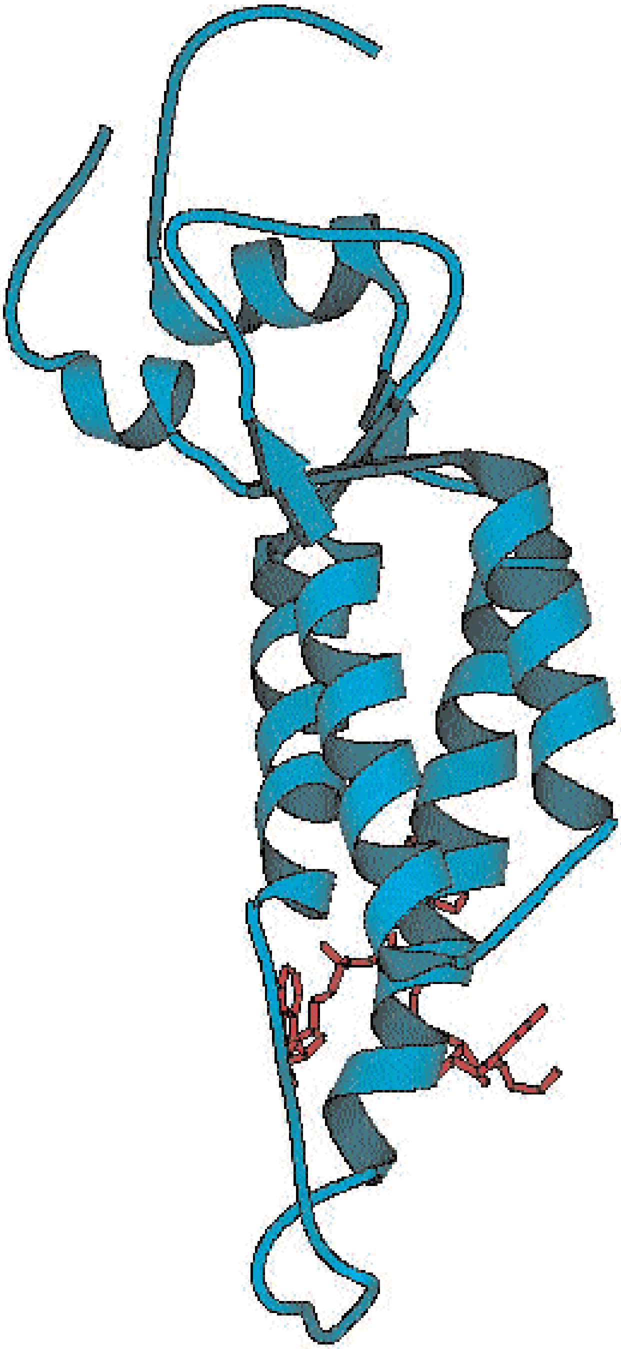

Issue 9

December 2000

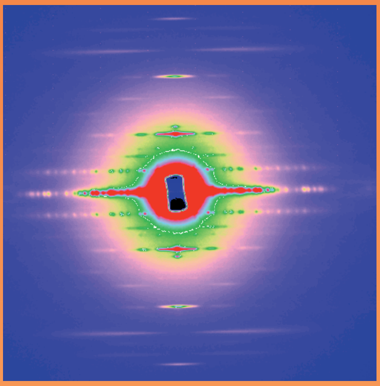

DARTS

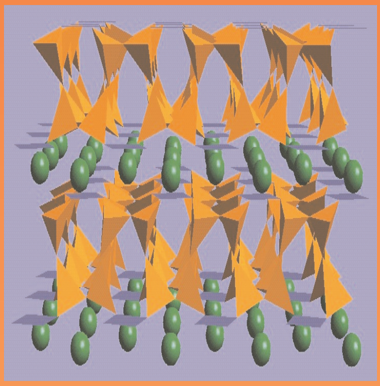

The Daresbury Synchrotron Radiation Service

Access to the unique properties of synchrotron radiation with a range of techniques

Rapid access and sample turn-round

Free for academic customers

Complete commercial confidentiality

Accelerated delivery of results

Service tailored to match your requirements

Support facilities available

DARTS Manager
Daresbury Laboratory
Warrington WA4 4AD, UK

phone +44 (0)1925 603141
FAX +44 (0)1925 603124
e-mail darts@dl.ac.uk

http://www.darts.ac.uk

DARTS

Daresbury Analytical Research and Technology Service

Contents

Technical Developments

Meeting Reports

Contributed Articles

Front Cover Image

Model of Tobacco Mosaic Virus (Gerald Stubbs)

Newsletter Production
Editor: Prof. J. Squire, Biological Structure and Function Section, Biomedical Sciences Division, Imperial College, London SW7 2AZ.
Production: Dr M.J. Rodman, Daresbury Laboratory, Warrington WA4 4AD.
Printer: Eaton Press Ltd, Westfield Road, Wallasey, Merseyside L44 7JB. (Tel. 0151-652 9111, Fax 0151-653 5936)

The CCP13 Committee Members (2000)

Chairman Dr Trevor Forsyth (to 2002)
Institut Laue-Langevin, BP 156 F-38042, Grenoble Cedex 9, France, and Physics Dept, Keele University, Staffordshire ST5 5BG
Phone +33 4 (0) 76207158 **Fax** +33 4 (0) 76483906 **Email** tforsyth@ill.fr

Research Assistant (Ex Officio) Dr Matthew Rodman (from January 2001)
Daresbury Laboratory, Daresbury, Warrington WA4 4AD
Phone 01925 603626 **Email** m.j.rodman@dl.ac.uk

Members

Dr David Blundell (to 2002)
Physics Department, Keele University, Keele, Staffordshire, ST5 5BG
Phone 01782 583330

Dr Patrick Fairclough (to 2002)
Department of Chemistry, The University of Sheffield, Dainton Building, Brookhill, Sheffield, S3 7HF
Phone 0114 2229411 **Fax** 0114 2229303 **Email** p.fairclough@sheffield.ac.uk

Dr Mike Ferenczi (to 2001)
National Institute for Medical Research, Ridgeway, Mill Hill, London NW7 1AA
Phone 0181 959 3666 **Email** m-ferenc@nimr.mrc.ac.uk

Dr Steve King (to 2001)
Rutherford Appleton Laboratory, Chilton, Didcot, OX11 0QX
Phone 01235 446437 **Fax** 01235 445720 **Email** s.m.king@rl.ac.uk

Prof. John Squire (to 2002)
Biomedical Sciences Division, Imperial College, London SW7 2AZ
Phone 0207 594 3185 **Fax** 0207 594 3169 **Email** j.squire@ic.ac.uk

Dr Tim Wess (to 2002)
Department of Biological and Molecular Sciences, University of Stirling, Stirling, FK9 4LA
Phone 01786 467775 **Fax** 01786 464994 **Email** tjw3@stir.ac.uk

Prof. Alan Windle FRS (to 2004)
Department of Materials Science and Metallurgy, University of Cambridge, Pembroke Street, Cambridge CB2 3QZ.
Phone 01223 334335 **Fax** 01223 335637 **Email** ahw1@cam.ac.uk

Members (Co-opted)

Dr Greg Diakun
Daresbury Laboratory, Daresbury, Warrington WA4 4AD
Phone 01925 603343 **Email** g.diakun@dl.ac.uk

Dr Tom Irving
CSRRI, Dept BCPS, Illinois Institute of Technology, 3101 s. Dearborn, Chicago IL. 60616, USA
Phone (312) 567-3489 **Fax** (312) 567-3494 **Email** irving@biocat1.iit.edu

Dr Rob Lewis
Daresbury Laboratory, Daresbury, Warrington WA4 4AD
Phone 01925 603544 **Email** r.a.lewis@dl.ac.uk

Dr Geoff Mant
Daresbury Laboratory, Daresbury, Warrington WA4 4AD
Phone 01925 603169 **Email** g.r.mant@dl.ac.uk

Prof. Rick Millane
Whistler Center, Purdue University, West Lafayette, Indiana 47907-1160 USA
Phone (765) 494-9272 **Email** rmillane@purdue.edu

Dr Keiichi Namba
Matsushita Electric Industrial Co. Ltd., 3-4 Hikaridai, Seika 619-0237, Japan
Phone 81-774-98-2543 **Fax** 81-774-98-2575 **Email** keiichi@crl.mei.co.jp

Prof. Gerald Stubbs
Dept of Molecular Biology, Vanderbilt University, 2200 West End Avenue, Nashville, TN 37235
Phone (615) 322-7311 **Email** stubbsgj@ctrvax.vanderbilt.edu

Chairman's Message

CCP13 has had a year of very mixed fortunes. It was extremely difficult to see the departure of Richard Denny and of Mark Shotton from the project, who have taken programming positions in industry. Both were graduates from the Keele fibre diffraction group. Richard was the first CCP13 RA and held the post for more than 6 years. Following his appointment to a position at Daresbury he remained a key influence both as a member of the Steering Committee and in the supervision of CCP13 activities at Daresbury. He will be remembered for the mathematical rigour that he built into CCP13 software and for his patience while helping a large number of users with software and data analysis. Mark Shotton, although involved for a much shorter period of time, also played a key role in the project. His attention to detail and sheer persistence in the face of difficult problems was extremely valuable for software development and for the user community. The expertise of both Richard and Mark will be badly missed in the academic sector and their recruitment into the private one reminds us of one of the major difficulties faced by all of the CCP projects: the fact that good scientific programmers are highly valued in industry. It is clear that individual CCPs and indeed funding agencies will need to bear this in mind if we are not to go through repeated cycles in which hard-earned years of experience in scientific research is lost to a vibrant commercial sector that pays well and offers better job security.

On the positive side we are extremely pleased to welcome Matthew Rodman as the new CCP13 postdoc, replacing Mark Shotton. Matthew is a physicist by training and has extensive expertise in procedural and object oriented programming. It is not easy at the best of times starting a new job, let alone starting one in which six months of programming, documentation and administrative tasks have accumulated. However, he has put himself to the task with enthusiasm and vigour and I am sure that we will all do everything we can to make this transition period pass as smoothly as possible.

Another major boost for CCP13 has been the excellent outcome of the latest grant renewal application. The application was submitted to the BBSRC Biomolecular Science Committee and was funded both by BBSRC and EPSRC. It will provide us with 3.5 postdoctoral posts to run along side half a post from the Non Crystalline Diffraction (NCD) group at Daresbury Laboratory. This amounts to a quadrupling of the manpower effort available.

This large enhancement of CCP13 funding could not have come at a better time. In addition to the seemingly relentless increase in computing power that we see from year to year, there are now massive changes on the horizon for the exploitation of a new high performance network (GRID) that promises vastly enhanced data access and transparency that will revolutionise the way we look at data management, data analysis and modelling. Now more than ever we need to recognise that programming initiatives such as CCP13 need to remain flexible and dynamic so that we can look to computational methods that were quite simply out of the question even just a few years ago. We also need to take a lead on establishing clear standards for the data that we use and produce. Such approaches will in the end have an enormous effect on the quality and throughput of our work.

Finally, I hope that you are all able to come to the CCP13/NCD workshop at Stirling University (13th-15th June). We have an excellent programme lined up and hope that the meeting will be as successful and as well attended as the previous meetings at St. Andrews and Sheffield Universities. Remember also that Fibre Diffraction Review, as well as containing invited papers presented at the annual workshop, is also open to submitted papers. All are thoroughly refereed and the distribution to colleagues within the field is highly effective. Please consider publishing your work here!

Trevor Forsyth
Institut Laue Langevin & Keele University Physics Department
May 2001

Summary of Available CCP13/NCD Software

Program	Description
XOTOKO	1-D data manipulation
BSL	2-D data manipulation
V2A	vax to unix data conversion
A2V	unix to vax data conversion
OTCON	ascii to otoko data conversion
RECONV	otoko to ascii data conversion
TIFF2BSL	image plate (tiff) to bsl conversion
BSL2TIFF	bsl to tiff conversion
I2A	ieee to ansi data conversion (DEC)
XCONV	file format conversion (GUI-driven)
XFIT	1-D fitting and plotting (GUI-driven)
XFIX	fibre pattern analysis (GUI-driven)
CONV	file format conversion (cmd line)
FTOREC	reciprocal space transformation
LSQINT	2-D integration and background fitting
CORFUNC	correlation function analysis
SAMPLE	Fourier-Bessel smoothing
FDSCALE	scaling and merging of intensities
FD2BSL	intensity to bsl conversion

The tables list the currently distributed CCP13/NCD programs, available as executable modules. The dates refer to the last creation of the executable.

A LOQ2BSL conversion program, for ISIS neutron data to BSL format, is also available for Solaris platforms.

Program	Solaris 2.7	Irix 6.2	OSF 3.2	Linux
XOTOKO	28/11/97	30/05/96	29/04/97	-
BSL	02/05/97	21/03/97	27/04/97	-
V2A	19/05/95	-	-	-
A2V	19/05/95	-	-	-
OTCON	06/06/95	08/07/94	-	08/05/97
RECONV	06/06/95	31/10/94	-	08/05/97
TIFF2BSL	17/03/97	-	-	-
BSL2TIFF	21/03/97	-	-	-
I2A	n/a	n/a	29/04/97	02/05/97
XCONV	04/06/99	04/06/99	-	04/06/99 *
XFIT	10/07/98	10/07/98	10/07/98	10/07/98 *
XFIX	09/04/99	09/04/99	09/04/99	09/04/99 *
CONV	09/04/99	09/04/99	09/04/99	09/04/99
FTOREC	12/04/99	12/04/99	12/04/99	12/04/99
LSQINT	12/04/99	12/04/99	12/04/99	12/04/99
CORFUNC	26/10/95	26/10/95	-	26/10/95
SAMPLE	05/11/96	04/11/96	04/11/96	04/11/96
FDSCALE	05/11/96	04/11/96	04/11/96	04/11/96
FD2BSL	05/11/96	04/11/96	04/11/96	04/11/96

* These programs have been tested on Slackware 3.4, SuSE 5.3 and RedHat 5.0 distributions of Linux.

Meeting Reports

CanSAS III, 17th-19th May 2001, Grenoble

The third annual 'Collective Action for Nomadic Small-Angle Scatterers' meeting was held at the ILL in the picturesque surroundings of Grenoble between May 17th to 19th. The meeting was convened in order for small-angle scatterers to share and extend data analysis tools and was composed of short talks as well as software demonstrations and group discussions.

Following lunch on the Thursday Wim Bras (DUBBLE) welcomed the delegates with an introduction to small-angle scattering. John Barnes (NIST) then presented a review of previous canSAS meetings before Ron Ghosh (ILL) briefly introduced use of simple XML in SAS data examples prepared for the meeting.

Elena Pourmal (NCSA) discussed the Hierarchical Data Format, listing the features of hdf5, such as the advances since hdf4 and the conversion technology that exists. She pointed out the limitations of hdf4 , such as its 2GB file limit, maximum object number, and multiple data models and explained how hdf5 was designed to rectify these and other shortcomings (including thread safety). Uwe Filges (PSI) then gave a brief account of porting NeXus to hdf5.

Following afternoon coffee, Trevor Forsyth (ILL & Keele University) spoke about using complementary X-ray and neutron techniques to observe both reversible and irreversible transitions between A,B,C,D and Z-type DNA. The day was drawn to a close by Dmitri Svergun (EMBL) who discussed solution scattering from mono-disperse and poly-disperse systems. He demonstrated a computational method of simulating the scattering from biological macromolecules using arrays of fixed-radius close-packed spheres.

Friday morning began with Marc Malfois (EMBL & ESRF) describing structured one-dimensional SAS data storage using sasCIF and continued with Peter Boesecke (ESRF) detailing requirements for processing synchrotron SAS experiments.

A major theme of the meeting was the dissemination of details of the myriad software packages available for small-angle scatterers. To this aim SANS data analysis was discussed by Elena Litvinenko (JINR, Dubna), who spoke about Visual Numerics' PV-Wave package and Charles Dewhurst (ILL) who demonstrated his Matlab-based 'Grasp' programme.

After lunch Steve King (ISIS) addressed the diverse fields of fibre diffraction, potholing and caving. He discussed his fibre-diffraction results concerning detergent-treated commercial nylon ropes. Steve explained that his interest stemmed from a wish to guard his own gear from any harm they may encounter during cleaning between excursions. Andy Hammersley (ESRF) then described the present status of FIT2D, and Rex Hjelm (LANL) explained the recombination of data within certain quality criteria neede to analyse TOF-SANS experiments. A poster and software demonstration session followed which touched on some enlightening code developments detailed by Els Homan (EMBL), Charles Dewhurst, John Barnes and Alan Munter (NIST).

The final day of the meeting began with Adrian Rennie (King's College,London) explaining the challenges in analysing soft matter small-angle scattering. The rest of the morning was devoted to a group discussion led by Ron Ghosh on the disparities in approach to data format in the community in general. A proposal was made to promote an XML-based solution to unifying *reduced* 1D and 2D small-angle scattering data files with the current push in the larger X-ray/neutron community towards the NeXus (HDF compatible) format. At the close of the meeting there was agreement on collaboration on a number of joint projects, including evaluation of XML and HDF tools on example small-angle scattering HDF datasets and developing a NeXus file definition for small-angle scattering. Progress will be reported at SAS-2002 in Venice.

Matthew Rodman
Ron Ghosh
Steve King

Contributed Articles

Analysis of the disordered myosin lattice in muscle

R.P. Millane and A. Goyal

Whistler Center for Carbohydrate Research and Computational Science and Engineering Program, Purdue University, West Lafayette, Indiana 47907-1160, U.S.A.

Introduction

Vertebrate muscle is made up of many parallel, long, thin strands known as microfibrils [1]. The repeating unit of the microfibrils is called the muscle sarcomere, and is the basic contractile unit of muscle. The sarcomere is made up of alternating ordered arrays of myosin and actin filaments, which are helical assemblies of myosin and actin molecules, together with various regulatory proteins [2]. The sarcomere exhibits a banded structure, the bands corresponding to different ordered arrays of myosin and/or actin filaments. One of these bands, the A-band, is spanned by the myosin filaments which are arranged on a hexagonal array, and also contains myosin cross-linking proteins and part of the actin filaments. The actin filaments extend partially into the ends of the A-band where they fit into the trigonal positions of the hexagonal myosin filament array. Mechanical force is believed to be developed by specific interactions between the myosin and actin molecules. The myosin molecules are a two-chain, coiled-coil, α-helical rod, and many rods form a roughly cylindrical filament that has three-fold helical symmetry.

The packing of myosin filaments within the lattices has been studied by X-ray diffraction, and also imaged directly by electron microscopy of thin transverse sections. The packing of the myosin filaments is most clearly seen in electron micrographs of transverse sections through the so-called “bare region” of the A-band [3]. This region is devoid of actin filaments and cross-linking proteins, and the filament profiles have a characteristic triangular shape allowing their orientations to be inferred. Both X-ray fibre diffraction and electron microscopy show that in the case of bony fish muscles, the myosin filaments pack on a regular hexagonal array with lattice dimensions of 47 nm [3]. However, for most other vertebrate muscle, X-ray diffraction patterns show a fundamental hexagonal spacing of ~81nm ≈47√3nm. Electron micrographs of thin sections through the bare region reveal the source of this longer spacing: the myosin filaments on the hexagonal lattice (of spacing 47 nm) adopt one of two orientations that are 60º (or 180º as a result of the 3-fold symmetry) apart [3]. The two orientations are not regularly distributed throughout the section, nor are they completely random. In fact, the orientations are distributed in a statistical fashion such that filaments which lie at the corners of a rhombus of side ~81µm tend to have the same orientation. This larger (partially regular) periodicity is referred to as the *superlattice*. An example of a micrograph of a section through the bare region of frog sartorius muscle that illustrates the superlattice structure is shown in Figure 10 of Luther & Squire [3], who studied it in considerable detail. Micrographs show that individual superlattices extend over only a few unit cells. The mode of packing is clearly important for our understanding of the actin-myosin interaction in vertebrate muscle.

X-ray fibre diffraction analysis is an important method for studying muscle structure. However the presence of statistical packing means that the X-ray intensities are not related to the molecular and crystal structures in a simple way. For this reason, direct analysis of muscle structure from X-ray fibre diffraction data has utilized specimens that display the simple myosin lattice, such as bony fish muscle [4-6]. We have previously developed methods for calculating cylindrically averaged diffraction from crystalline systems that exhibit short-range order [7,8]. This approach can potentially be used to analyze diffraction data from higher vertebrate muscle, but an accurate statistical model of the disordered myosin lattice structure would be required. With this is mind, we report here a more quantitative study of the statistical structure of the disordered myosin lattice.

The disordered myosin lattice

A detailed study of the disordered myosin lattice has been conducted by Luther & Squire [3], based on a micrograph of a particularly well ordered transverse section through the bare region of a whole microfibril of frog sartorius muscle (their Figure 10). They were able to unambiguously assign the orientations of 639 of the 775 filaments in this section. A reproduction of their interpretation of the micrograph is shown in Figure 1(a), where the red

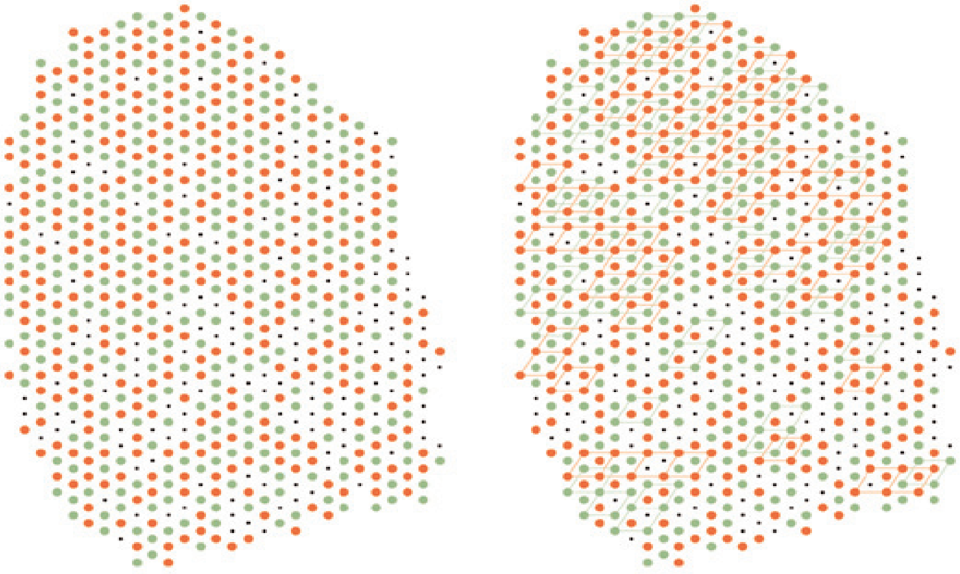

Figure 1: Orientations of the myosin filaments in a transverse section through the bare region of frog sartorius muscle (from Figure 10 of Luther & Squire [3]) (left), and the corresponding superlattice cells (right).

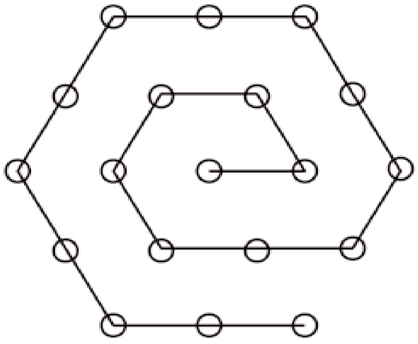

Figure 2: Spiral algorithm for building a hexagonal lattice.

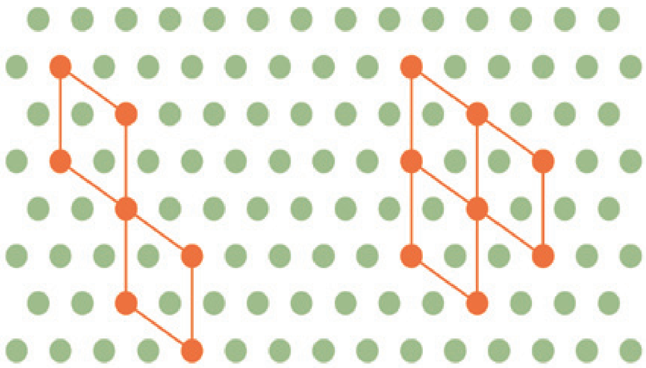

Figure 3: Two superlattice cells (left) and a 3-cell superlattice domain (right).

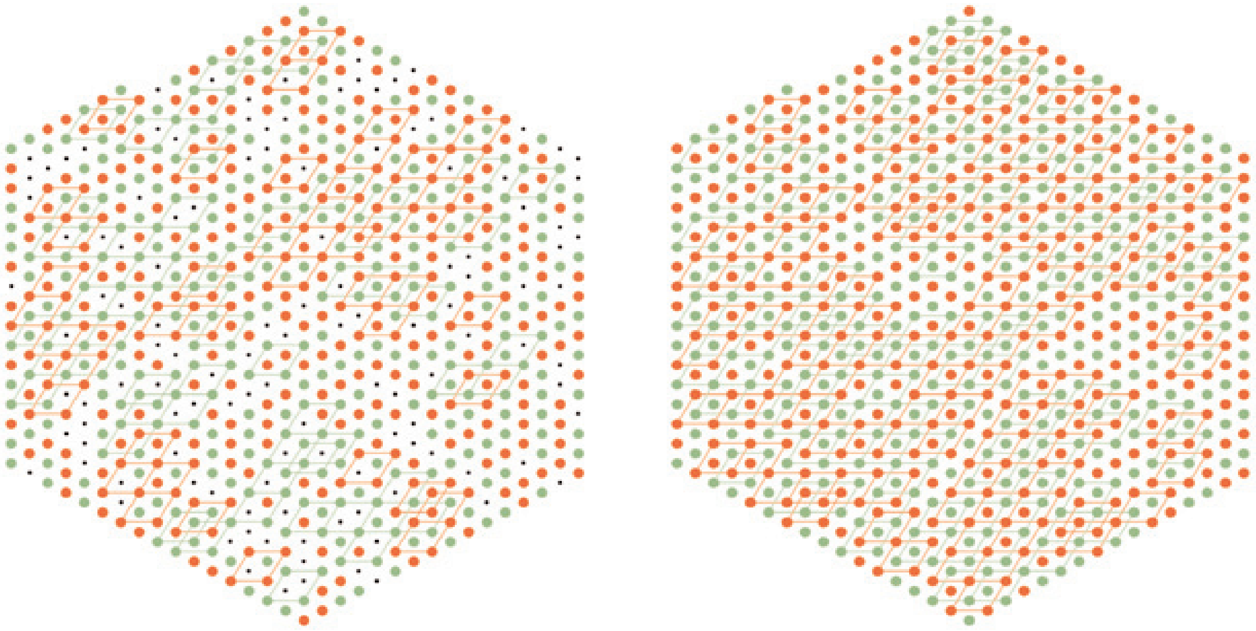

Figure 4: A 775-point disordered lattice generated as described in the text and showing the superlattice cells for: orientations of 136 sites unknown (left), and orientations of all sites known (right).

and green circles indicate the two different filament orientations (referred to as *up* and *down*) and the black dots indicate the filaments whose orientations could not be reliably determined. On detailed inspection of the distribution of filament orientations, they made two important observations. The first was the presence of the superlattice structure referred to above, and that the superlattice regions extend for only a few unit cells. The second observation was that the orientations of the filaments generally satisfy two rules. The first (rule 1) is that the three mutually adjacent filaments at the vertices of a triangle do not all have the same orientation, and the second (rule 2) is that three adjacent filaments along a row do not all have the same orientation. They referred to these as the *no-three-alike* rules. They noted that exceptions to the rules do occur, although quite infrequently, and that exceptions to rule 2 occur more often than do exceptions to rule 1. They also showed that the simple lattice and superlattice structures could be interpreted in terms of different interactions in the M-band and crossbridge region [3,9].

Luther & Squire [3] also studied the relationship between the rules and the superlattice by building synthetic lattices based on the rules and analyzing the lattices obtained. They generated hexagonal lattices of 127 sites following a spiral path (Figure 2). The orientation at each new site was defined by assigning it randomly, but only consistently (if possible) with whichever rules are being applied. Lattices were generated applying rule 1 only, rule 2 only, or both rules. Their results led to a number of

Type of lattice	p_1	p_2	N	N_u	f_{r1v}	f_{r2v}	f_s	$<N_{sd}>$
Figure 1			775	136	0.011	0.059	0.389	2.6
Rule 1 only	1	0	775	136	0.000	0.112	0.293	2.3
Rule 2 only	0	1	775	136	0.011	0.010	0.537	4.7
Rules 1 & 2	1	1	775	136	0.000	0.000	0.583	5.4
Rules 1 & 2	1	0.20	775	136	0.002	0.074	0.369	2.8
Rule 1 only	1	0	775	0	0.000	0.113	0.305	4.0
Rule 2 only	0	1	775	0	0.011	0.010	0.555	14.9
Rules 1 & 2	1	1	775	0	0.000	0.000	0.603	18.8
Rules 1 & 2	1	0.20	775	0	0.002	0.076	0.380	7.9

Table 1: Parameters calculated from the micrograph (Figure 1a) and from the simulated lattices

important conclusions, the main ones being that extensive superlattice is obtained if both rules are applied, and that a lattice similar to that observed is obtained if it is built by applying both rules, but occasionally allowing rule 2 to be broken. Their results are only semi-quantitative however, since they are for a small lattice (where edge effects will be important), they are for a single simulation and so are subject to statistical uncertainty, and analysis of the results does not take into account the effect of the sites of unknown orientation in the data. We describe here generation and analysis of synthetic lattices of the kind described by Luther & Squire [3], but overcoming the deficiencies described above and conducting a quantitative comparison of the resulting superlattice structure with that observed.

Characterizing the disordered lattice

To quantitatively compare simulated lattices with an experimentally observed lattice such as that shown in Figure 1(a), parameters are needed to quantitate the statistical properties of the lattices. The no-three-alike rules are related to local order in the lattice, and the superlattice is a longer (medium) range characteristic. We therefore define four parameters in terms of these characteristics. The first two parameters are the relative frequencies with which the two rules are broken. Consider a finite hexagonal lattice of N sites. We refer to a set of three sites that correspond to one of the rules as a rule *clique*, and the total number of cliques is denoted by N_{r1c} and N_{r2c} for rules 1 and 2, respectively. The number of cliques for which a rule is broken (violated) is denoted by N_{r1v} and N_{r2v}, for rules 1 and 2, respectively, and the first two parameters we use are the frequencies of rule violation, denoted by f_{r1v} and f_{r2v}, given by

$$f_{r1v} = \frac{N_{r1v}}{N_{r1c}}$$

and $$f_{r2v} = \frac{N_{r2v}}{N_{r2c}}$$

The two other parameters we use are related to the amount of superlattice. We define a superlattice cell as any rhombus with edges of length √3 times the spacing of the underlying hexagonal lattice for which the orientations at each corner of the rhombus are identical. Superlattice cells can occur in three different orientations but, since they are not independent, only one orientation is considered. All the superlattice cells in Figure 1(a) are shown in Figure 1(b). The number of superlattice cells in a lattice is denoted by N_s. The maximum possible number of superlattice cells (e.g. if the orientations at all sites were the same) is denoted by N_s^{max}, and for our third parameter we use the normalized number of superlattice cells $f_s = N_s / N_s^{max}$. The superlattice structure is of more significance (particularly in terms of diffraction) if the superlattice cells are contiguous and form superlattice crystalline domains. We refer to a *superlattice domain* as a set of superlattice cells that share at least one common edge for each superlattice cell, and use for our fourth parameter the average superlattice domain size, $<N_{sd}>$ defined as the average number of superlattice cells per domain. The larger $<N_{sd}>$, the more extensive and contiguous is the superlattice structure.

Simulations

Our objective is to generate synthetic lattices following Luther & Squire [3], and to compare the values of the parameters described above to those derived from Figure 1(a). The fact that the orientations of some of the filaments could not be determined must be taken into account in the analysis. Sites with unknown orientation are not used when computing N_{r1v}, N_{r2v}, N_{r1c}, N_{r2c}, N_s and N_s^{max}. Therefore, on average, the number of rule violations and the number of cliques, and the number of superlattice cells and the maximum possible number, will be reduced proportionately as a result of unknown orientations. Therefore, the presence of sites with unknown orientation should have little effect on the parameters f_{r1v}, f_{r2v} and f_s. However, the effect of unknown orientations will be to break up large superlattice domains into smaller domains, so that the effect on $<N_{sd}>$ is expected to be significant.

A computer algorithm was developed to analyze a lattice of the kind shown in Figure 1(a), of any shape and with any number of internal sites for which the orientation is unknown, and to calculate the parameters described above. Application of this algorithm to the lattice shown in Figure 1(a), that has $N = 775$ total sites and $N_u = 136$ sites for which the orientation is unknown, gave values of the parameters listed in Table 1. Note that rule 1 is satisfied almost always (99%), rule 2 is satisfied 94% of the time, and about one-third of the maximum possible superlattice cells are present. The average size of the superlattice domains is rather small (2.6), presumably due in part to the sites for which the orientation is unknown.

A second computer algorithm was developed to build spiral lattices according to the rules (as described above). Using this program, 2000 lattices with $N = 775$ sites were built, applying rule 1 only, rule 2 only, and both rules. The parameters were calculated from the resulting lattices in two different ways. In the first, 136 sites of each generated lattice, chosen at random, were labelled as 'unknown orientation' and were disregarded when calculating the parameters. This case mimics the analysis of Figure 1(a). In the second case, all 775 sites were used when analyzing the generated lattices. The parameters were averaged over the 2000 lattices and are listed in Table 1.

Consider first the case for which the orientations at 136 sites are unknown. Rule 1 lattices produce no rule 1 violations but about 10% rule 2 violations, rule 2 lattices produce few rule 1 or rule 2 violations, and rule 1 and 2 lattices produce no rule violations. These results are in general in accord with the results of Luther & Squire [3] for 127-site simulated lattices. Rule 2 lattices produce about twice the number of superlattice cells, and about twice the superlattice domain size, as do rule 1 lattices. Application of rule 1 and rule 2 gives slightly more superlattice structure than does rule 2 only. Comparison of the amount of superlattice with the observed amount shows that rule 1 produces not enough and rule 2 produces too much (as observed by Luther & Squire [3]). The program for generating the lattices was therefore modified in the following way. When computing the orientation at a new site, rule 1 and rule 2 were considered only with probabilities p_1 and p_2, respectively. Lattices were then generated with $p_1 = 1$ and p_2 adjusted so that the amount of superlattice obtained (f_s and $<N_{sd}>$) matched that observed as well as possible. This led to $p2 = 0.20$ and the resulting parameters are listed in Table 1. Inspection of these values shows a good fit of the parameters to the data. This indicates that our algorithm is producing disordered lattices that have quantitatively the same statistics as the disordered myosin lattice. An example of a generated lattice and its superlattice cells is shown in Figure 4(a), and comparison with Figure 1(b) shows qualitative similarities.

Turning now to the results obtained when the orientations are known at all sites of the lattice, inspection of Table 1 shows that the frequency of rule violations is essentially identical to those obtained for the lattices with unknown orientations, and the relative number of superlattice cells is very similar, as anticipated above. The average superlattice domain size is considerably larger, however, as anticipated. Since the first three parameters in the first part of Table 1 fit the data well, we can take the parameters in the second part of the table to represent those of the full myosin lattice (all sites). In particular, this predicts that the average superlattice domain size is about 8 superlattice cells. An example of a generated full lattice is shown in Figure 4(b), where the more extensive superlattice is evident.

Discussion

Model lattices can be built based on the superlattice rules that quantitatively mimic the statistical structure of the observed disordered myosin lattice. The effect of unknown filament orientations can be taken into account, and the model can be used to predict properties of the full lattice.

The model lattices described here can be used to characterize the detailed statistics of the disordered myosin filament array. We have previously developed efficient analytical / numerical methods for calculating the cylindrically averaged diffraction (fibre diffraction patterns) from polycrystalline fibres in which helical molecules are subjected to correlated lattice disorder within the crystallites [7,8]. The myosin filament array can be described by a similar statistical model, although in general the two different filament orientations may need to be represented by substitution, rather than lattice, disorder. We expect that a similar approach to that which we have used previously will accommodate substitution disorder. Using this theory, together with the statistics derived from a model of the kind described here, it should be possible to compute simulated fibre diffraction patterns from the disordered myosin filament array. The results of such a calculation can then be used to refine molecular and packing models using standard techniques.

Acknowledgements

We are grateful to John Squire and Pradeep Luther for pointing out this interesting disordered lattice to us and for discussion, and to the U.S. National Science Foundation for support (DBI-9722862).

References

[1] Squire, J.M., *The Structural Basis of Muscular Contraction*. (Plenum, New York, 1981).
[2] Squire, J.M., *Curr. Opin. Struct. Biol*. (1997) 7, 247-257.
[3] Luther, P.K. and Squire, J.M., *J. Mol. Biol.* (1980) 141, 409-439.
[4] Harford, J. and Squire, J., *Biophys. J.* (1986) 50, 145-155.
[5] Hudson, L., Harford, J. J., Denny, R. C. and Squire, J. M., *J. Mol. Biol.* (1997) 273, 440-455.
[6] Squire, J., Cantino, M., Chew, M., Denny, R., Harford, J., Hudson, L. and Luther, P., *J. Struct. Biol*. (1998) 122, 128-138.
[7] Stroud, W.J. and Millane, R.P., *Proc. Roy. Soc. Lond. A* (1996), 452, 151-173.
[8] Stroud, W.J. and Millane, R.P., *Acta Crystallogr.* (1996), A52, 812-829.
[9] Luther, P.K., Munro, P.M.G., and Squire, J.M., *J. Mol. Biol.* (1981) 151, 703-730.

Network of Ordered Phases in PE-PEE Diblock Copolymers

Hiroshi Takenouchi[1], Damian A Hajduk[2] and
Frank S. Bates

[1] Kawasaki Development Center, Montell SDK Sunrise Ltd.,2-3-2, Yako, Kawasaki-ku, Kawasaki, Japan.

[2] Symyx Technologies, 3100 Central Expressway, Sunnydale, California 95951

[3] Department of Chemical Engineering and Materials Science, Universoty of Minnesota, Mineapolis MN 55455

The phase behavior and network of order-order phase transitions occurring in binary mixtures of poly(ethylene)-poly(ethylethylene)(PE-PEE) diblock copolymers containing between 60 and 75% by volume PE have been characterized near the order-disorder transition (ODT) by dynamic mechanical spectroscopy (DMS) and small-angle X-ray scattering (SAXS). Three equilibrium phases (lamellae - L, gyroid - G, and cylinders - C) and one metastable phase (perforated layers - PL) are identified in a phase portrait defined by the composition $<f_{PE}>$ *and combination parameter* $\chi<N>$ *where* χ *and* $<N>$ *are the segment-segment interaction parameter and average degree of polymerization. These results unify disparate past findings on the complex phase behavior of diblock copolymer melts near the ODT.*

Introduction

Although the phenomenon of microphase separation in block copolymers has been studied for over three decades, a detailed appreciation of phase behavior in the intermediate and weak segregation limits was not established until the past decade. In fact, the first report of an order-order phase transition (OOT) in a block copolymer melt occurred just 8 years ago [1], followed soon thereafter by many other examples that resulted in the identification of several relatively complete phase diagrams [2-5]. Five morphologies have been established for diblock melts: spheres (S) packed on a body centered cubic lattice; cylinders (C) arranged on a hexagonal lattice; the gyroid (G), a triply periodic and tricontinuous structure with *Ia3d* space group symmetry; lamellae (L), a smectic morphology; perforated layers (PL), a layered structure that contains a hexagonal arrangement of passages through one of the layered microdomain spaces. Figure 1 illustrates these structures. A combination of experiment [6] and theory [7] has established with fair certainty that the PL phase is metastable, while the other structures occur at equilibrium.

Near the order-disorder transition (ODT), phase transitions between ordered phases can be realized at certain polymer compositions by changing temperature (or pressure). These OOT's generally are accompanied by significant changes in the viscoelastic properties of the material, thereby providing a convenient mechanical signal for establishing T_{OOT}; this method of locating phase transitions in block copolymers has been employed to find T_{ODT}'s for many years [8-11]. Subsequently, the domain type and packing symmetry can be ascertained using small angle X-ray and/or neutron scattering (SAXS and SANS), and electron microscopy. Along with establishing static phase behavior we have employed this approach in exploring the underlying OOT mechanisms and kinetic pathways dictated by epitaxial relationships [12].

Earlier work on nearly monodisperse poly(ethylene)-poly(ethylethylene)(PE-PEE) diblock copolymers with $0.25 \leq f_{PE} \leq 0.5$ (f_{PE} is the volume fraction of PE), and blends of $f_{PE} = 0.37$ and 0.46 copolymers, established the viability of using binary mixtures of diblocks to determine phase behaviour near the ODT as a function of the average composition $<f_{PE}>$ [3]. Using just two diblocks the composition can be varied continuously, avoiding the need to synthesize separate macromolecules, a time consuming and tedious process. This prior investigation, along with several related ones, established that transformations between ordered phases are often kinetically limited, leading to substantial hysteresis on heating and cooling, in some circumstances generating long-lived metastable states. Recently, we have concluded that the PL morphology is such a metastable phase [6], appearing as a transient state during the transformation of lamellae to the gyroid structure. Theoretical calculations [7,13-15] support this finding and provide a rationale for the long-lived nature of the PL phase. In general, the morphological pathway followed upon heating or cooling a block copolymer melt is governed by at least two factors: epitaxial relationships and the rate of heating or cooling.

Sample	[a]f_{PE}	[b,c]M_n (kg mol^{-1})	[b]M_w/M_n	[d]phases (°C)
PE-PEE-7	0.75	44	1.05	C-(148)-Dis
PE-PEE-6	0.65	43	1.05	L-(143)-PL-(166)-G-(197)-C-(202)-Dis
PE-PEE-17	0.60	42	1.05	L-(242)-D

a. Volume fraction of PE based on NMR analysis, synthesis stoichiometry, and published densities [21].
b. Determined from GPC analysis.
c. From synthesis stoichiometry.
d. Determined by DMS (while heating at 0.3 °C/min) and SAXS.

Table 1. Block Copolymer Molecular Characteristics

The work reported here compliments our previous study with PE-PEE blends [3], covering the composition range $0.60 \leq \langle f_{PE} \rangle \leq 0.75$, where the L, PL, G, and C phases are all found. Dynamic mechanical spectroscopy (DMS) and SAXS experiments have been used to determine the phase behaviour as a function of $\langle f_{PE} \rangle$ and temperature. By varying the rate of heating and cooling through order-order transitions we have gained fresh insights regarding phase transition dynamics, and completed our picture of the kinetic pathways between the L, PL, G, and C morphologies.

Experimental

The PE-PEE diblock copolymers used in this study were synthesized and characterized using well-established procedures [16, 17]. Molecular characteristics are listed in Table 1. These saturated hydrocarbon polymers are stable against oxidative degradation. The PE block is semicrystalline with a melting temperature of $T_m \approx 108$ °C while the PEE block exhibits a glass transition temperature at about -20 °C. All measurements reported here were conducted in the melt state.

Blends of PE-PEE-7 and PE-PEE-17 were prepared by codissolution in toluene at 90 °C followed by precipitation in methanol and vacuum drying at 140 °C for 12 hours.

DMS measurements were performed on a Rheometrics RSAII solids analyzer with a shear sandwich fixture containing a 0.5 mm gap. A nitrogen gas purge was used to minimize sample oxidation at high temperatures. The work reported here was based on a single type of measurement: heating or cooling at a fixed rate (0.1 - 2.0 °C/min) while measuring the linear dynamic elastic shear modulus G'(T) at a fixed frequency of 0.5 rad/s. Transmission electron microscope (TEM) images were obtained from selected samples. Although not presented here, the TEM results were consistent with the phase assignments identified in the following sections.

Small-angle X-ray scattering (SAXS) patterns were obtained on a beamline at the University of Minnesota; a description of this instrument is given elsewhere [6]. SAXS patterns were used as the principal tool for identifying phase symmetry and

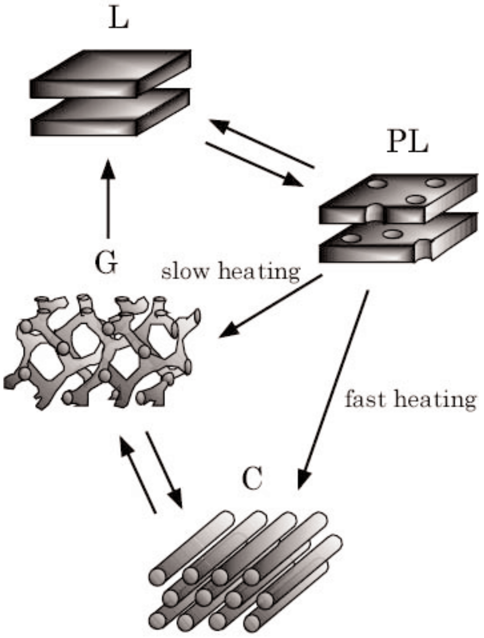

Figure 1: Ordered morphologies documented in diblock copolymers near the order-disorder transition: L-lamellae, PL-perforated layers, G-gyroid,C-cylinders. The L, G, C structures constitute equilibrium phases while PL is a metastable state. Arrows identify documented order-order transitions (OOT's).

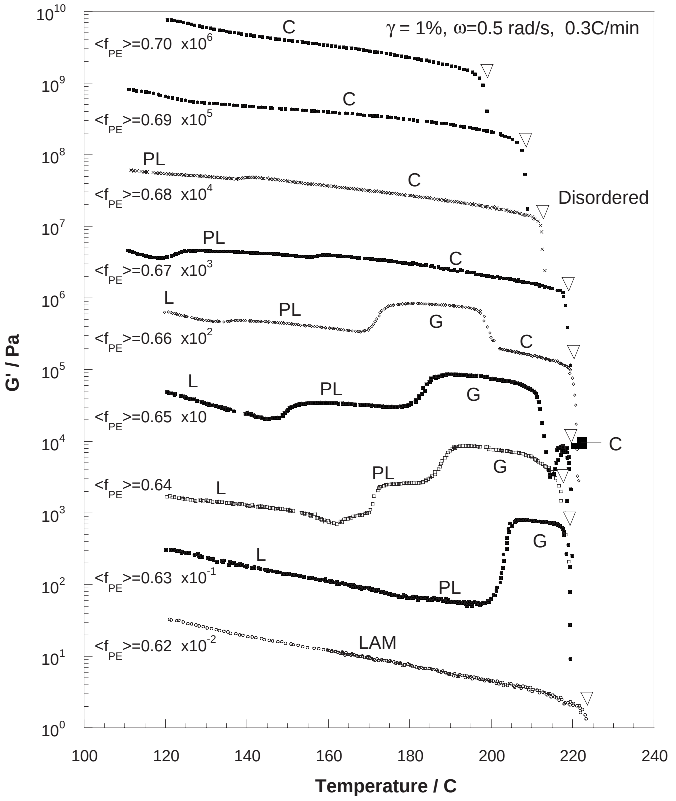

Figure 2: Linear dynamic elastic shear modulus (G') as a function of temperature for mixtures of PE-PEE-7 and PE-PEE-17. $<f_{PE}>$ represents the overall volume fraction of PE. These data were acquired while heating the specimens at 0.3 ^{o}C/min with a 1% strain amplitude and a frequency of 0.5 rad/s. Order-order phase transitions are associated with a rapid increase or decrease in G'. Order-disorder transitions are identified by the open triangles. Data have been shifted vertically as noted by the composition labels.

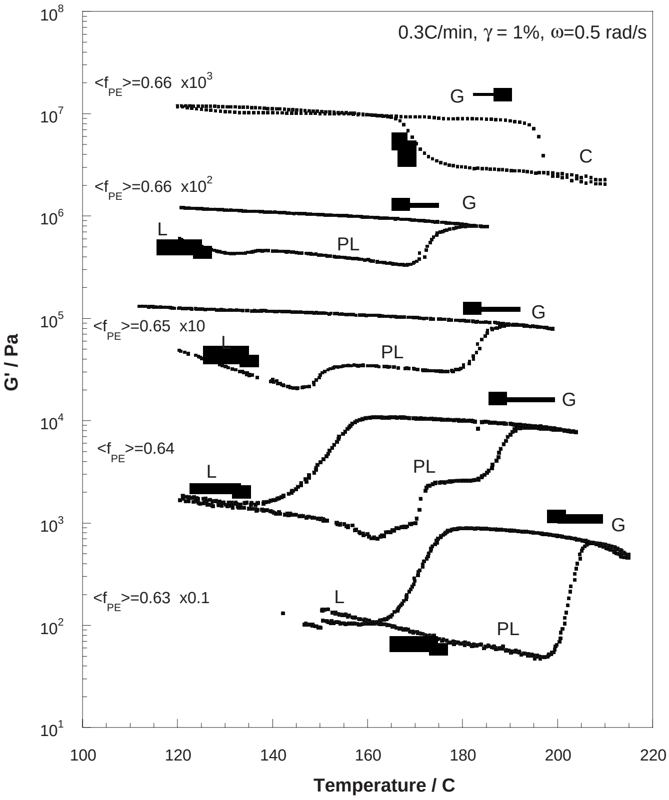

Figure 3: Phase behaviour of ordered PE-PEE binary mixtures as a function of heating and cooling under the same conditions as in Figure 2. Two sets of data were recorded for the $<f_{PE}>=0.66$ specimen: first heating from 120 to 185 ^{o}C followed by cooling to 120 ^{o}C (lower set), then heating to 210 ^{o}C and subsequently cooling to 120 ^{o}C (upper set).

deducing the associated morphology. Although only limited SAXS data are presented in this report, the basis for establishing ordered phases followed the procedures established in numerous previous publications [3-6].

Results and Analysis

Phase Behaviour Phase transition temperatures were identified in nine PE-PEE binary blends ($0.62 \leq fPE \leq 0.70$), formed by mixing PE-PEE-7 and PE-PEE-17 (see Table 1), using isochronal ($\omega = 0.5$ rad/s) G' measurements while heating the specimens at 0.3 °C/min. DMS results are presented in Figures 2 (heating) and 3 (heating and cooling). Order-order phase transitions are associated with a rapid increase or decrease in G', reflecting differences in the elastic characteristics of specific morphologies [3]. One of the four microstructures shown in Figure 1 is identified with each viscoelastic portion of the G'(T) curves. These assignments were made using well-established interpretations of SAXS patterns, supported by several TEM micrographs (not shown here). For example, the L phase produces SAXS patterns with reflections at scattering wavevectors q*, 2q*, 3q*, … where $q = 4\pi\lambda^{-1}\sin(\theta/2)$ with $q^* = 2\pi/d^*$, d* being the lamellae period. A representative SAXS pattern obtained from a lamellae specimen is given in Figure 4a. Upon heating into the PL regime, the second-order reflection disappears as shown in Figure 4b. (Extensive experimentation with this phase in several other block copolymers, including *in-situ* neutron scattering while shearing [18], forms the basis for the phase assignments presented here). The G and C morphologies produce distinctly different SAXS data, with reflections at $\sqrt{3}q^*$, $\sqrt{4}q^*$, … and q*, $\sqrt{3}q^*$, $\sqrt{4}q^*$, $\sqrt{7}q^*$, …., respectively. We have not presented this evidence here since it duplicates comparable results reported in several earlier publications.

Order-disorder transition temperatures (T_{ODT}) are signalled by a complete loss of elastic modulus as

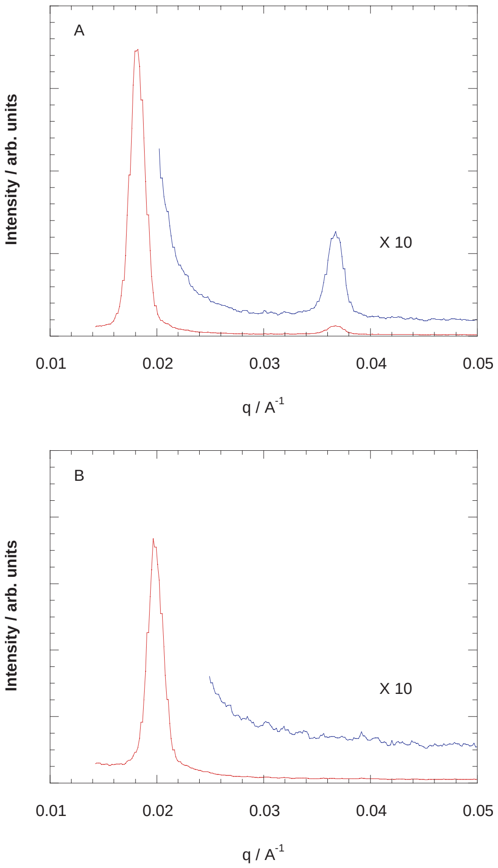

Figure 4: Representative SAXS patterns taken from the $\langle f_{PE} \rangle$=0.63 mixture. (A) T=160^{o}C. Reflections at relative positions of q*, 2q*... are consistent with a lamella phase. (B) Loss of higher order reflections at 200 ^{o}C is associated with the perforated layers phase. Phase assignments are also supported by TEM images (not shown here).

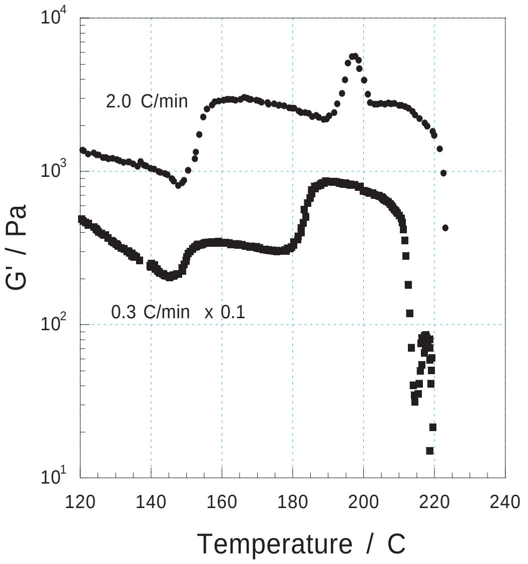

Figure 5: Influence of heating rate on G'(T) for $\langle f_{PE} \rangle$=0.65 PE-PEE mixture. Varying the heating rate from 0.3 ^{o}C/min to 2.0 ^{o}C/min switched the transition path from PL→G to PL→C, respectively. Strain amplitude and frequency are as given in Figure 2.

noted by the open triangles in Figure 2.

A clear pattern of phase behaviour emerges from the G'(T) results in Figure 2. As $\langle f_{PE} \rangle$ increases from 0.62 to 0.70 at constant temperature (ca 180 °C), there is a progression from L to PL to G and finally C. The OOT's form smooth curves as a function of composition and temperature across multiple specimens, carving out well-defined regions for each morphology. For example, the cylindrical state first emerges on heating in the $\langle f_{PE} \rangle$ = 0.65 specimen within 5 °C of T_{ODT}. As $\langle f_{PE} \rangle$ increases the C window broadens, ultimately encompassing the entire experimental temperature range at $\langle f_{PE} \rangle$ = 0.69. However, all these OOT temperatures are subject to the effects of superheating as illustrated by the results found in Figure 3.

Finite nucleation and growth kinetics result in a delay in the transformation from one ordered state to another. This translates into hysteresis when the material is heated and cooled at a finite rate. These DMS data confirm that upon heating L → PL → G while on cooling G → L, bypassing the PL phase. This pattern is identical to one documented in PEO-PEE [19] at just one-twentieth the molecular weight og the PE-PEE diblocks. Two different classes of OOT's where probed in the $\langle f_{PE} \rangle$ = 0.66 sample, which exhibits all four morphologies included in Figure 1. At lower temperatures the L → PL → G sequence occurs, a natural progression from the behavior at lower compositions (see Figure 2). However, cooling the G phase fails to generate lamellae, a result anticipated by the reduction in $T_{L \rightarrow PL}$ as $\langle f_{PE} \rangle$ increases; this effect also was encountered in the PEO-PEE study [19]. This is consistent with our hypothesis that PL is a metastable structure that only forms as a long-lived transient state during transformation of lamellae to gyroid. In contrast the higher temperature OOT, is a reversible, G → C and C→ G, albeit hysteretic transition.

Rate Dependence We have further probed the dynamics of these phase transitions by varying the rate of heating the $\langle f_{PE} \rangle$ = 0.65 sample while monitoring G' (Figure 5). Increasing dT/dt from 0.3 to 2.0 °C/min has little impact on the L → PL transition, presumably due to the similarity in symmetry, i.e. both are layered morphologies. However, whereas the sequence L → PL → G → (C)→ disorder occurs at the lower heating rates, we believe the G phase is bypassed at 2.0 °C/min, i.e. L

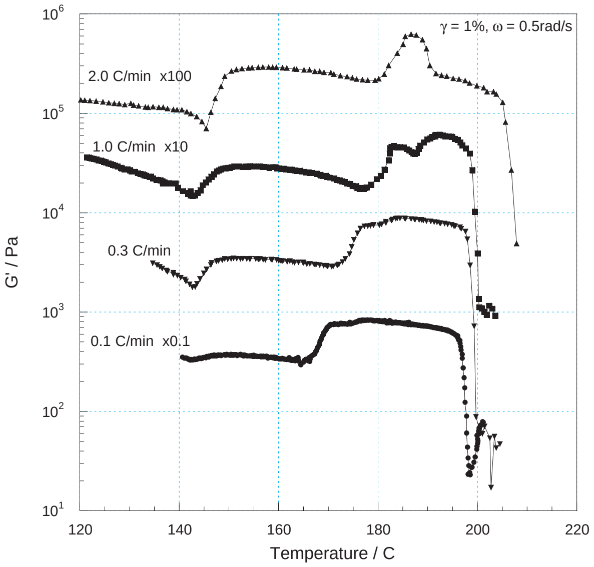

Figure 6: Influence of heating rate on G’(T) for PE-PEE-6, a nearly monodisperse sample. These results are nearly identical to those in Figure 5 confirming that the heating rate dependence of these OOT’s is not attributable to mixing.

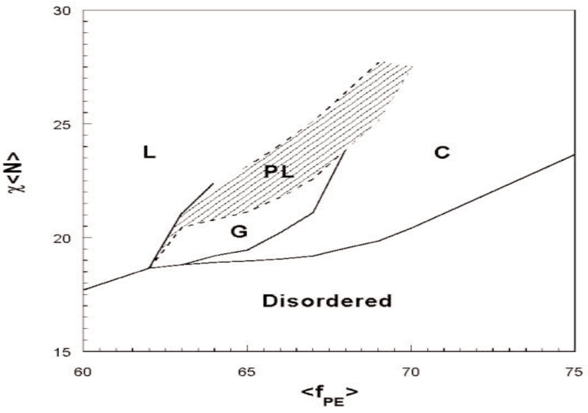

Figure 7: Phase portrait of PE-PEE diblock copolymers as a function of the product χN and the composition $<f_{PE}>$. Phase boundaries have been assigned based on the transition temperatures identified in Figure 2. The PL phase is metastable while L, G, and C are equilibrium states. At equilibrium the indicated order-order phase boundaries will shift up slightly, and the G phase will cover the area denoted PL.

→ PL→ C → disorder. We base this deduction on the magnitude of G' between 190 and 205 °C and the elevated value of T_{ODT} = 206 °C relative to the precipitous drop in G' at about 195 °C when dT/dt = 0.1 °C/min (also compare these results with those in Figure 2). Apparently there is insufficient time to nucleate the PL → G transition at the higher heating rate. Instead the superheated PL phase forms cylinders, presumably due to a lower kinetic barrier. We interpret the peak in G'(T) at about 187 °C as resulting from a transition state structure. Identification of the morphologies underlying these G'(T) patterns rectifies earlier confusion in making phase assignments to PEP-PEE block copolymers near the ODT.

We have excluded the possibility that the results presented in Figure 5 are influenced by the bimodal composition distribution of the PE-PEE-7/ PE-PEE-17mixture by repeating the experiments on sample PE-PEE-6, a relatively monodisperse diblock copolymer with the same composition (Table 1). G'(T) for four representative heating rates (0.1, 0.3, 1.0 and 2.0 °C/min) are presented in Figure 6. Nearly identical phase transitions as those seen in Figure 5 were produced by this compound.

Discussion

The experiments reported here, together with our earlier studies, allow us to present a complete picture of the network of morphologies and kinetic pathways that govern the phase behaviour of diblock copolymers near the order-disorder transition. Figure 1 includes arrows identifying the known OOT's linking the three equilibrium and one metastable phases that occur near f_{PE} = <0.65> in PE-PEE. Upon heating L transforms to PL; this is a thermally reversible transition as shown elsewhere (see Figure 14 in ref. 18). Slowly heating the PL phase results in a transition to G, while rapid heating produces C, both irreversibly. G and C transform reversibly, through an OOT that is known to be mediated by an epitaxial relationship [12]. Cooling G leads to a direct conversion to L, bypassing the metastable PL phase.

We present a phase portrait summarizing our results in Figure 7. Based on $\chi(T) = 15.0T^{-1} - 0.0055$ [16], χ<N> is plotted versus $<f_{PE}>$ where <N> is the number average degree of polymerization assuming 4-carbon repeat units. The phase boundaries have been located according to the transition temperatures extracted from Figure 2; due to hysteresis effects these are all displaced to slightly lower χ<N> than the true equilibrium values. Shading in the PL window signifies metastablity. At equilibrium the G phase extends over the entire PL region and the L - G phase boundary lies somewhat higher in χ<N> than the L - PL boundary (see Figure 7). This phase portrait is strikingly similar to those characterizing

PS-PI, PEP-PEE, PEP-PDMS, and PEO-PEE.

One notable exception to this universal picture is the PE-PEP system in which the G phase has never been identified [2, 20]. Based on the results reported here we can finally understand this puzzling disparity. PE and PEP are nearly compatible, requiring a molecular weight of more than 10^5 g/mol to induce microphase separation at 150 °C [16]. Also, PE and PEP both are characterized by low entanglement molecular weights ($M_{e,PE} \approx 1{,}000$ and $M_{e,PEP} \approx 1{,}600$ g/mol compared with $M_{e,PEE} \approx 10{,}000$ g/mol [21]). Taken together these two facts lead to extremely slow single chain dynamics in microphase separated PE-PEP relative to the other systems listed above. Thus, the commonly applied heating protocol of 1-2 °C/min while probing OOT's will access the "fast heating" branch in Figure 1, and therefore the PL → C transition in PE-PEP. Thus, it would be difficult to access the G phase in PE-PEP (the most entangled and highest molecular weight diblocks studied [2]), in a steady heating experiment, since switching to the "slow" heating branch will require an unfeasible reduction in heating rate of orders of magnitude.

Decreasing the molecular weight of the block copolymer (this requires an increase in incompatibility if χN is to remain constant) and increasing M_e ultimately leads to a crossover from a single chain dynamic limit (which dominates the PE-PEP system) to a regime governed by nucleation and growth. Apparently the PE-PEE system lies near this crossover since both the "slow" (PL → G) and "fast" (PL → C) heating branches are accessible (Figures 5 and 6). All available evidence suggests that lower molecular weight, and less entangled, systems (e.g. PS-PI [4], PS-PVP [5], PEP-PDMS [22], PEO-PEE [19]) follow "fast" branch kinetics (i.e. the PL → G transition), consistent with dynamics dictated by nucleation and growth. In fact, the consequences of these effects may be evident within the PE-PEE (and PEP-PEE) system itself. The complex phase window centered around $\langle f_{PE} \rangle = 0.40$ does not exhibit the heating rate dependence evident in Figures 5 and 6; e.g., the G phase appears at dT/dt = 2.0 °C/min [2]. We believe this is a consequence of the higher percentage of PEE, hence a significantly higher average entanglement molecular weight, in these specimens.

Summary

Dynamic mechanical spectroscopy and small-angle X-ray scattering experiments with binary mixtures of PE-PEE diblock copolymers over the composition range $0.60 \le \langle f_{PE} \rangle \le 0.75$ have resulted in a complete network of phase transitions between the equilibrium (L, G, and C) and metastable (PL) phases. Phase transition pathways were shown to be strongly influenced by both single chain dynamics and nucleation and growth rates. These results clarify the occurrence of the PL phase and absence of G in certain high molecular weights systems.

Acknowledgments

Partial support for this work was provided by Showa Denko K.K. (HT) and by the Materials Research Science and Engineering Center (MRSEC) at the University of Minnesota.

References

[1] Almdal, K., Koppi, K.A., Bates, F.S. and Mortensen, K., *Macromolecules* (1992) 25, 1743.
[2] Bates, F.S., Schultz, M.F., Khandpur, A.K. et al., *Faraday Discuss*. (1994) 98, 7.
[3} Zhao, J., Majumdar, B., Schultz, M.F. et al., *Macromolecules* (1996) 29, 1204.
[4] Khandpur, A.K., Förster, S., Bates, F.S. et al., *Macromolecules* (1995) 28, 8796.
[5] Schulz, M.F., Khandpur, A.K., Bates, F.S. et al., *Macromolecules* (1996) 29, 2857.
[6] Hajduk, D.A., Takenouchi, H., Hillmyer, M.A. et al., *Macromolecules* (1997), 30, 3788.
[7] Matsen, M.W.and Bates, F.S. *Macromolecules* (1996) 29, 1091.
[8] Chung, C.I. and Gale, J.C. J. *Polym. Sci., Polym. Phys. Ed*. (1976) 14, 1149.
[9] Gouinlock, E.V. and Porter, R.S. *Polym. Eng. Sci.* (1977) 17, 535.
[10] Han, C.D., Kim, J. and Kim, J.K. *Macromolecules* (1989) 22, 383.
[11] Rosedale, J.H. and Bates, F.S. *Macromolecules* (1990) 23, 2329.
[12] Schulz, M.F., Bates, F.S., Almdal, K. et al., *Phys. Rev. Lett.* (1994) 73, 86.
[13] Matsen, M.W. and Bates, F.S. *Macromolecules* (1996) 29, 7641.
[14] Qi, S. and Wang, Z.-G., *Phys. Rev. Lett.* (1996) 76, 1679.

[15] Shi, A.-C., Desai, R.C. and Noolandi, J. *Phys. Rev. Lett.* (1997) 78, 2577.
[16] Rosedale, J.H., Bates, F.S., Almdal, K. et al., *Macromolecules* (1995) 28, 1429.
[17] Bates, F.S., Rosedale, J.H., Bair, H.E., et al., *Macromolecules* (1989) 22, 2557.
[18] Hamley, I.W., Gehlsen, M.D., Khandpur, A.K. et al., *J. Phys. II*, France (1994) 4, 2161.
[19] Hillmyer, M.A., Bates, F.S., Almdal, K. et al., *Science* (1996) 271, 976.
[20] Rosedale, J.H., PhD Thesis, University of Minnesota (1993).
[21] Fetters, L.J., Lohse, D.J., Richter, D. et al., *Macromolecules* (1994) 27, 4639.
[22] Vigild, M.E., Almdal, K., Mortensen, K. et al., *Macromolecules* (1998) 31, 5702.

Modelling diffraction patterns from a textured polycrystalline sample

Y. Nishiyama[1] and P. Langan[2]

1. Graduate School of Agricultural and Life Science, University of Tokyo, Yayoi, Tokyo 113-8657, Japan

2. B. Division, Los Alamos National Laboratory, MS-M888, Los Alamos NM87545 USA

Introduction

Fibre diffraction studies have enabled structural information to be extracted from materials that are difficult to crystallize into macroscopic single crystals or when the state of interest is not highly crystalline. It is usually assumed that the sample is an aggregate of basic scattering units, each with an associated unique axis. The scattering units either exhibit rotational symmetry about the unique axis or the distribution of orientations about the unique axis is random. In addition to this, the distribution of the unique axis itself is given by a function that has rotational symmetry about a preferred direction, called the fibre axis. This is a good approximation for fibrous materials with diffraction information uniformly distributed around the fibre axis. However, there are fibrous, polycrystalline materials in which the distribution of the unique axis does not have rotational symmetry about the fibre axis or in which the scattering units are not uniformly orientated around the unique axis. The first effect is often referred to as texture. When the second effect corresponds to a second direction in the basic scattering unit being preferentially oriented around a second axis in the fibre it is referred to as biaxial orientation. In our studies of the crystal structure of native cellulose we have obtained sharp diffraction data extending to 1Å resolution (1) but exhibiting complex texture resulting from a combination of the two effects mentioned above. This problem also afflicts quasi-single-crystalline α-chitin from which good data have been collected recently (2), but the refined structure has yet to emerge due to the lack of proper software to deal with diffraction data from a specimen of complex texture. This article describes a realistic approach to processing diffraction data from fibre specimens with complex texture and is illustrated with the structure of native cellulose as an example.

The sample and diffraction data

The acquisition of diffraction data from highly oriented cellulose film specimens from the tunicate *Halocynthia roretzi* has been described elsewhere (3). The sample consisted of crystalline whiskers with polygonal cross-section which are about 20 nm in width and a few microns in length. A series of X-ray diffraction patterns was collected at 15º intervals around the main axis, and another series of patterns was obtained by tilting the main axis in 2º steps. Each frame was then converted to polar (RZ) coordinates on a 0.001 Å-spaced grid out to 1 Å without merging the four quadrants. Consequently each frame consisted of 2000 by 2000 pixels. The diffuse background was subtracted using the method by Sonneveld (4) extended into two-dimensions.

Computation environment

The computation was carried out on a Linux system equipped with a Pentium III, 256 Mbytes of RAM, and a gcc-2.95.2 compiler.

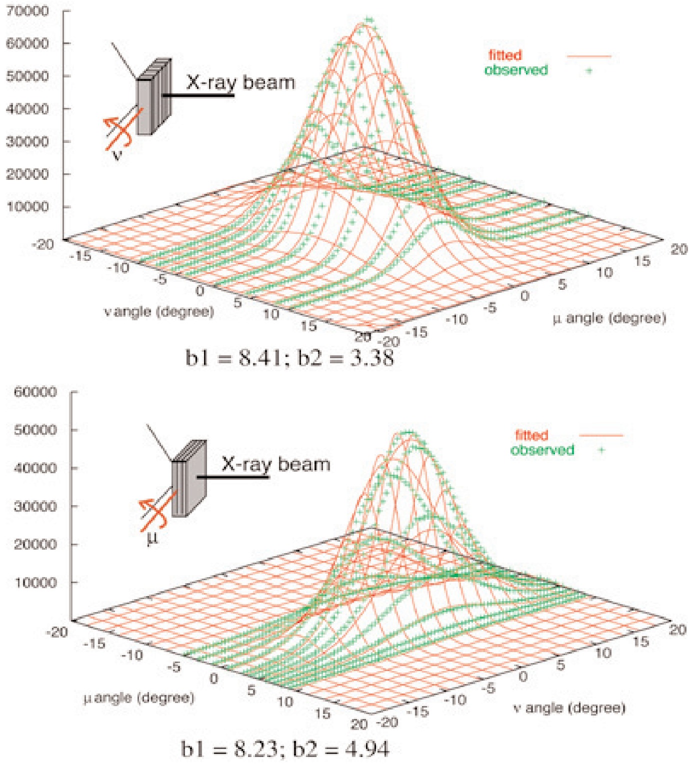

Figure 1. Observed and fitted azimuthal intensity profile of the 004 reflection. The fitted parameters were slightly different between the two sets of experiments and the mean value was taken to define the orientation of the c-axis.

Defining the texture

The texture of the sample can be determined experimentally by measuring the pole figures of two reflections that are in different directions (preferably perpendicular to each other). This can be readily measured when diffraction data are obtained through the whole of reciprocal space.

In the part which follows Cartesian coordinates (XYZ) are used to define principal directions in the sheet specimen (Y perpendicular to the plane, X and Z in plane).

The orientation of the main axis:

Figure 1 shows the observed and fitted intensity distribution of the 004 reflection of the specimen. It can be seen that the unique axes of the crystallites have a broader distribution in a plane parallel to the film surface than perpendicular to it. The distribution function could be fitted with a two-dimensional Gaussian function of the form

$$I = \exp\left(-\left(\frac{\mu}{b_1}\right)^2 - \left(\frac{\nu}{b_2}\right)^2\right)$$

where μ is the angle to the XZ-plane or the film surface, ν is the angle to YZ-plane that is perpendicular to the film surface, and b_1 and b_2 are the standard deviations. In the present case b_1 and b_2 were 4.2º and 8.3º respectively. In a general case, the orientation distribution can be expressed as a function of (μ,ν).

The orientation of the second axis: The existence of preferred orientation of the second axis can be seen in the diffraction pattern obtained with the beam parallel to the Z-axis (Fig. 2). The orientation of the second axis is confined to a circle around the main axis and can be described by only one parameter ω which is defined here as the angle between the second axis $\mathbf{e}_2$ and the YZ plane. Thus an arbitrary orientation can be expressed by three parameters μ,ν,ω, and a three-dimensional population density function ρ(μ,ν,ω) can describe the texture of any polycrystalline sample.

Calculation of azimuthal profile

A difference between b_1 and b_2 itself leads to an asymmetric diffraction pattern at a higher diffraction angle except when taken with the beam

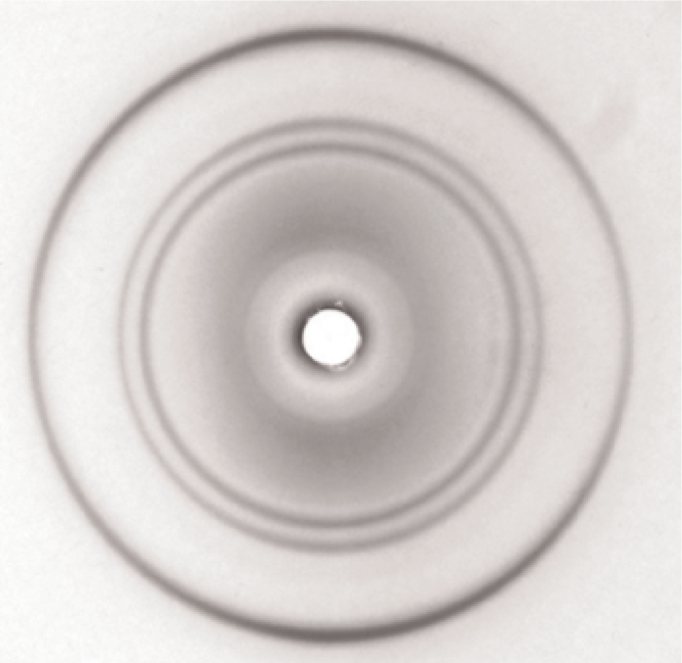

Figure 2. Diffraction diagram taken with the beam parallel to the main axis of the sample: the film surface is horizontal.

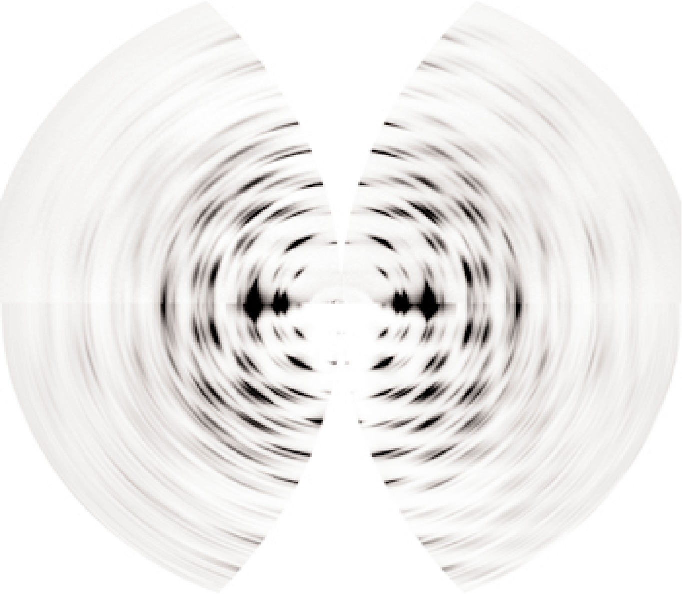

Figure 3. Asymmetric diffraction diagram from oriented cellulose film specimen. The upper half is observed data, and the bottom half is the simulated data.

perpendicular or parallel to the surface. An example is shown in Figure 3. Even if a symmetric diagram could be obtained, the azimuthal intensity profile of each reflection would not be the same as in the fibre case.

In the following analysis, the intensity calculation is for a reflection at position vector ***p*** that makes an angle σ to the main crystallite axis $\mathbf{e}_1$, a dihedral angle ϕ around $\mathbf{e}_1$, and is at a distance *r* from the origin. Consider a position *P* that has a polar coordinate (*r*, τ, υ) as illustrated in Figure 4. The crystal contributing to the diffraction intensity at *P* due to the reflection ***p*** has its main axis $\mathbf{e}_1$ on a cone of semi-angle σ (i.e. between between $\mathbf{e}_1$ and OP). The Cartesian coordinates of the orientation vector $\mathbf{e}_1$ can be described using an angular parameter θ as follows:

$$\mathbf{e}_1 = \mathrm{R}(\upsilon)\mathbf{e}_1'$$

where:

$$\mathbf{e}_1' = \frac{r\tan\sigma\left[\cos\theta\begin{pmatrix}1\\0\\0\end{pmatrix}+\sin\theta\begin{pmatrix}0\\-\cos\tau\\\sin\tau\end{pmatrix}\right]+P}{r/\cos\sigma}$$

$$=\begin{pmatrix}\sin\sigma\sin\theta\\ \cos\sigma\sin\tau-\sin\sigma\cos\theta\cos\tau\\ \cos\sigma\cos\tau+\sin\sigma\cos\theta\sin\tau\end{pmatrix}.$$

For a given orientation of $\mathbf{e}_1$, the orientation of $\mathbf{e}_2$ is uniquely determined as

$$\mathbf{e}_2 = \frac{\mathbf{p}-(r\cos\sigma)\mathbf{e}_1'}{r\cos\sigma}$$

The number of crystals that are contributing to the intensity at that position can be calculated by integrating the population density function ρ over a circle on the cone, or

$$=\int_{-\pi}^{\pi}\rho(\mathbf{e}_1,\mathbf{e}_2)\sqrt{\left(\frac{\partial\mu}{\partial\theta}\right)^2+\left(\frac{\partial\nu}{\partial\theta}\right)^2}\,\mathrm{d}\theta$$

$$=\int_{-\pi}^{\pi}\rho(\mathbf{e}_1,\mathbf{e}_2)\sqrt{\cos^2\theta+\sin^2\theta\cos^2\tau}\,\mathrm{d}\theta$$

The integration cannot be obtained analytically for most types of function ρ and should be obtained numerically. The integration for grid points of appropriate interval and range in reciprocal space can be

$$I(P)=\int_C\rho(P)=\int_{-\pi}^{\pi}\rho(\mathbf{e}_1,\mathbf{e}_2)\left|\frac{\partial\mathbf{e}_1}{\partial\theta}\right|d\theta$$

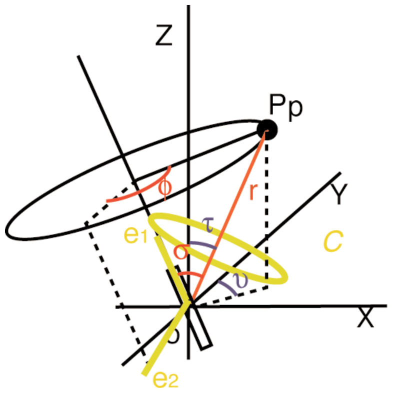

Figure 4. Schematic illustration to define the geometry parameters.

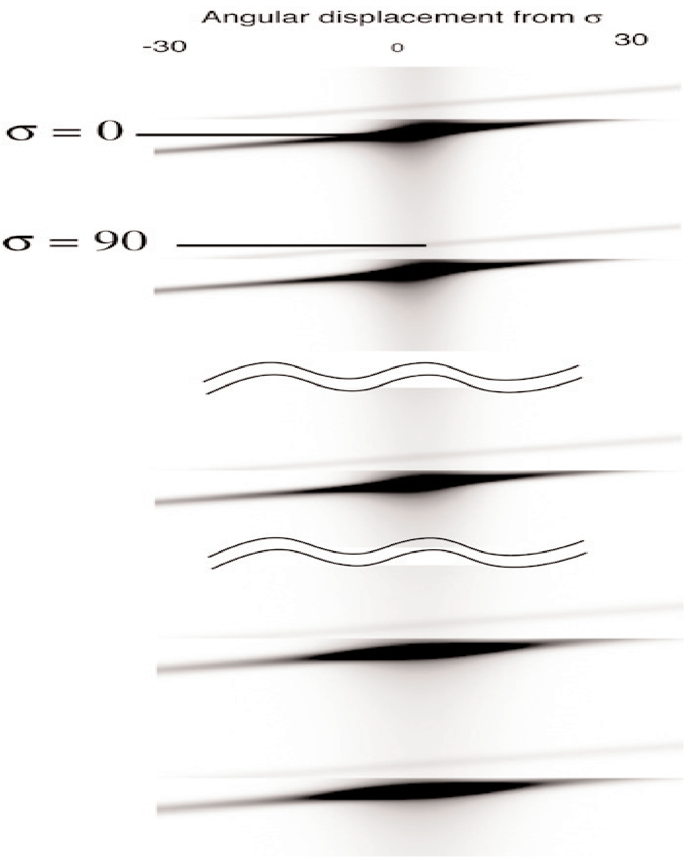

Figure 5. Part of the grid data representing the azimuthal intensity distribution shown in grey scale.

calculated and stored to be interpolated on use. Note that the integration is independent of *r* and only depends on σ, τ, υ and ϕ. Thus the azimuthal intensity profile should be stored in a 4-dimensional array in the most general case. If the texture is such that the orientation of $\mathbf{e}_2$ is independent of the orientation of $\mathbf{e}_1$, or

$$\rho(\mu, \nu, \omega) = \rho_1(\mu, \nu)\rho_2(\omega),$$

and ρ_1 is much sharper than $\rho_2(\omega)$, then I(P) can be approximated as:

$$\mathrm{I(P)} \approx \mathrm{I}_2 \cdot \mathrm{I}_1 = \rho_2(\upsilon - \phi)\int_{-\pi}^{\pi} \rho_1(e_1)\,d\theta$$

and the profile can be stored in two arrays, one of 3-dimensions and one of 1-dimension, to economise on memory and CPU time. This was done in the case of the cellulose sample.

The DQAGE routine from the Fortran mathematical library QUADPACK [5] used to calculate the integration and the interpolation routine for even spaced multi-dimensional grids was obtained from Magic Software Inc. [6]. The evaluation of I_1 in 200 *100 * 30 grid points took about 5 min. Figure 5 shows the array as a grey image.

Determination of the orientation of the second axis

Since the volume of specimen in the beam varied when the specimen was rotated around the Z-axis, the orientation of the second axis was evaluated by comparing the intensity of three reflections on the equator. It would be possible to arrange experiments so as to ensure that there is a constant specimen volume in the beam path, for example by using smaller samples, but this leads to a higher background which is not desirable. Thus the orientation of the second axis was determined from the relative intensities of several clearly resolvable reflections. The intensity ratios of the three most intense reflections, I_{200}, I_{110} and $\mathrm{I}_{1\text{-}10}$ of the cellulose I data are plotted in Figure 6.

Since there should be equal numbers of up and down crystals, and if the **a**-axis is taken as $\mathbf{e}_1$, then:

$$\mathbf{I}_{rel} = \frac{\mathrm{I}_1(\omega)}{\mathrm{I}_2(\omega)} = I_{12}\,\frac{\rho_2(\omega-\phi_1)+\rho_2(\omega+\phi_1)}{\rho_2(\omega-\phi_2)+\rho_2(\omega+\phi_1)}$$

In a matrix expression for a discrete set of ρ_2:

$$\rho_2(\omega-\phi_1) = \Phi_1\rho_2(\omega)$$

$$\Phi_1 = \begin{array}{c} \begin{matrix} & \phi_1 & & n-\phi_1 & \end{matrix} \\ \begin{pmatrix} & \bullet & & \bullet & \\ & & \bullet & & \bullet \\ \bullet & & & \bullet & \\ & \bullet & & & \bullet \\ \bullet & & \bullet & & \end{pmatrix} \end{array}$$

$$(\Phi_1\rho_2+\Phi_{-1}\rho_2)\cdot\mathbf{I}_{rel}=(\Phi_2+\Phi_{-2})I_{12}\rho_2\ ,$$

$$((\Phi_1+\Phi_{-1})\mathbf{I}_{rel}-(\Phi_2+\Phi_{-2})I_{12})\rho_2=0$$

thus I_{12} can be obtained by solving:

$$\left|(\Phi_1+\Phi_{-1})\mathbf{I}_{rel}-(\Phi_2+\Phi_{-2})I_{12}\right|=0$$

ρ_2 can be obtained as an eigenvector. When using several combinations of reflections, a least squares solution can be obtained by solving the following matrix equation with standard matrix inversion:

$$\begin{pmatrix} & \mathbf{A}_1 & \\ & \mathbf{A}_2 & \\ 1 & L & 1 \end{pmatrix}\rho=\begin{pmatrix} O \\ O \\ 1 \end{pmatrix}$$

where

$$\mathbf{A}_i=(\Phi_i+\Phi_{-i})\mathbf{I}_{rel}-(\Phi_j+\Phi_{-j})\,I_i$$

The resulting orientation function ρ and the density profiles of the 200 and 110 reflections are plotted in Figure 7. The reflection profiles become symmetric due to the presence of up and down crystals.

Calculation of the radial profile

Radial broadening comes solely from instrumental broadening, finite crystal size and the presence of crystal imperfections, and can be treated independently of the orientation issue. To analyse this, we used a pseudo-Voigt function of the form:

$$f=\frac{A}{C}\{D*G+(1-D)*L\}$$

$$G=2\sqrt{\frac{\ln 2}{\pi}}D\exp\left\{-4\ln 2\left(\frac{x-B}{C}\right)^2\right\}$$

$$L=\frac{4}{\pi\left\{1+4\left(\frac{x-B}{C}\right)^2\right\}}$$

where A is the peak area, B is the peak position, C is the full width at half maximum (FWHM) and D is a shape parameter between 0 and 1.

Construction of the normal equation

Usually the observed intensities are due to multiple reflections, and modelling is done for the purpose of resolving each component as far as possible. If the orientation distribution and the radial profile are known, the least-squares fitting to the observed data $\mathbf{y}_{obs}$ is a linear problem:

where $\mathbf{a}_i$ is the profile of the *i*th reflection. If the number of data values is *m*, then **A** is a matrix of size *n* by *m*. This can be directly solved if *m* is not too big. With an oriented sample, **A** is a sparse matrix as each reflection contributes to only a small number of data. Although **A** is sparse and could be stored in more compact form, the observed data extend throughout 3-dimensional reciprocal space and would be too numerous. A normal equation is thus constructed as:

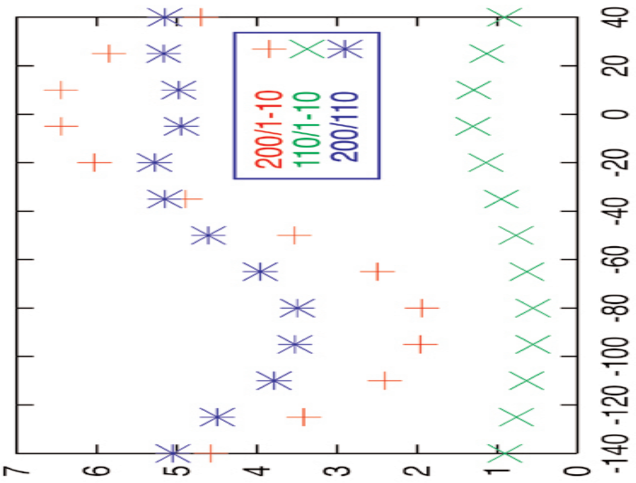

Figure 6. Plot of intensity ratios among the three strongest equatorial reflections from the cellulose sample taken at different rotations around the main axis.

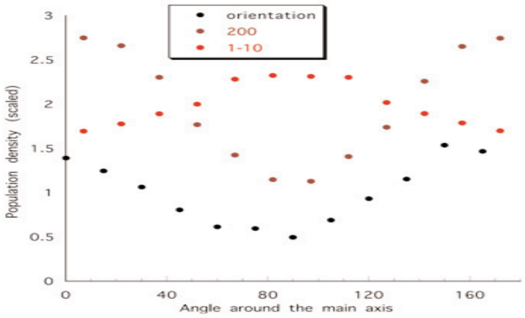

Figure 7. The orientation function and the simulated reflection intensity profile around the main axis. The intensity profiles are symmetric and up and down crystals are assumed to contribute equally.

$$\tilde{\mathbf{A}}\mathbf{Af} \equiv \mathbf{Bf} = \mathbf{Ay}_{obs} \equiv \mathbf{b}$$

$$\text{or, } B_{kl} = \sum_{j=1}^{n}\sum_{i=1}^{n} A_{ki}A_{jl}$$

The direct calculation of B needs n-by-n function evaluations for each of the m-by-m elements. However, since only a limited number of reflections can contribute to a given position, the potentially-contributing reflections were chosen prior to each calculation of element B_{kl}, and the summation was carried out only within a subgroup of (i, j) to make the calculation feasible. In the present case, the reflections within a radial limit of 0.03 Å-1 and within 30° in an azimuthal direction were included.

$$\mathbf{y}_{obs} = \mathbf{a_1} * f_1 + \mathbf{a_2} * f_2 \ldots \mathbf{a_n} * f_n = \mathbf{Af}$$

Singularity issues

The above matrix B is singular if there are reflections that are very close compared to the sharpness of the peak, which is the case for most polycrystalline samples. This means that the normal equation cannot be solved by usual matrix inversion; actually there is no way to know the individual intensity. Consequently the singular value decomposition (SVD) method was chosen as a way to easily filter degenerate components. The DGELSD, a LAPACK [8] driver routine, was used to calculate the minimum norm least-squares solution. The routine gives back the effective rank of the normal matrix B.

The calculation of 12 frames together, including about 800 reflections, took about 80 hours of computation time to construct and to solve the normal equation. The effective rank was 625. The simulated image of half of a frame is shown in the lower part of Figure 3.

The Lorenz-Polarization factor

Since the calculated azimuthal profiles are already based on the number of reflections contributing to the observed intensity, no consideration is needed for the factor due to orientation. The only correction needed to obtain the structure factor is the distance of the reflection from the centre in reciprocal space, as the density diminishes by the square of the distance.

Conclusion

The azimuthal profile of any reflection from a polycrystalline specimen can be calculated by numerical integration of a function defining the texture. A series of diffraction patterns could be simulated in an acceptable time using a standard computational environment.

Acknowledgements

We thank Dr. H. Chanzy for valuable suggestions for the conduct of the work.

References

[1] Presented at the CCP13 Workshop 2000.
[2] H. Chanzy, *Advances in Chitin Science*: Jacques Andre Publishers, France (1998) Vol.II, 11-21.
[3] Y. Nishiyama, S. Kuga, M. Wada, T. Okano, *Macromolecules* (1997) 30, 6395.
[4] E. J. Sonneveld & J. W. Visser, *J. Appl. Cryst* (1975) 8, 1.
[5] http://www.netlib.org/quadpack/
[6] http://www.magic-software.com/
[7] http://www.netlib.org/lapack/

Fibre diffraction and diversity in filamentous plant virus structure

G. Stubbs, G. Ferrell, M. Reams and
N. Fletcher

Department of Molecular Biology, Vanderbuilt University,
Box 351634, Station B, Nashville, TN 37235-1634

Fibre diffraction has a long history of successful structural analysis of tobamoviruses such as tobacco mosaic virus. Studies of other filamentous plant viruses, however, have been fraught with difficulties. These difficulties stem primarily from problems of specimen preparation rather than the inherent complexity of the viral structures. Low yield, low solubility, and flexibility have all contributed to these problems. Nevertheless, over the years diffraction patterns have been obtained from members of several filamentous plant virus groups, and the potexviruses in particular are beginning to provide high quality fibre diffraction data.

Tobacco mosaic virus

Filamentous plant viruses are among the oldest fibre diffraction specimens; the first diffraction patterns from tobacco mosaic virus (TMV) were described in 1936 [1], and TMV has served as a model for the development of fibre diffraction methods ever since then.

Techniques for making oriented sols of TMV were originally developed by Bernal and Fankuchen [2] and refined by Gregory and Holmes [3]. These sols were made by drawing virus from a centrifuged pellet into an X-ray capillary tube, and moving the column of virus, usually mixed with a little buffer solution, back and forth in the capillary to induce orientation by shearing forces. Sols made in this way had concentrations of 200 to 300 mg/ml, and disorientation angles of little more than 1°, and they are still among the best diffracting fibre specimens in biology. In fact, one such sol made by Holmes in 1960 was the source of diffraction patterns taken in 1982 and used in the structure determination of TMV at 2.9 Å resolution [4].

TMV also served as a model for fibre diffraction data processing, particularly using the method of angular deconvolution [5], and for objective methods of phase determination. Isomorphous replacement was used very early to obtain radial density distributions of TMV [6,7], and developed further to solve the multi-dimensional phase problem in high resolution structure determination by fibre diffraction [8]. Other techniques developed or refined using TMV included layer line splitting [9] and molecular replacement [10]. Methods of structure refinement and evaluation were also developed using TMV; examples include restrained least-squares refinement [11], molecular dynamics refinement [12], difference Fourier analysis for fibre diffraction [13] and fibre diffraction *R*-factors [14,15].

These methods were used to determine the structure of TMV at 2.9 Å resolution, and to refine it to an R-factor of 0.096 [4]. Related virus structures followed. The structure of the U2 strain of TMV (U2) was determined at 3.5 Å resolution by molecular replacement from TMV [10], the structure of cucumber green mottle mosaic virus (CGMMV) was determined at 3.4 Å resolution using a combination of isomorphous replacement and molecular replacement [16], and the structure of ribgrass mosaic virus (RMV) was determined at 2.9 Å resolution by molecular replacement [17]. These three virus structures were all refined by molecular dynamics methods [12]. The RMV structure is probably the best-determined tobamovirus structure; its R-factor is 0.095, very close to that of TMV, but the geometry of the RMV model is considerably better.

These structure determinations are all very encouraging for those who use fibre diffraction methods. They are the largest structures to be determined in atomic detail by fibre diffraction, and they have been of considerable use in interpreting the chemistry and biology of the viruses. But the coat proteins of the viruses are highly homologous. TMV and CGMMV are 36% identical, while TMV and RMV are 46% identical. And although there are important differences among the structures, the protein folds are extremely similar (Figure 1).

Other filamentous plant viruses

Despite successes with the tobamoviruses, there has been little progress in fibre diffraction from other filamentous plant viruses.

The International Committee on Taxonomy of

Figure 1: The coat proteins and nucleic acid binding sites of three tobamoviruses. Coat protein folds are represented by ribbon diagrams; RNA by skeletal models. (a) TMV (b) CGMMV (c) RMV.

Viruses currently recognizes 22 genera of plant viruses [18]. A few are morphologically similar to each other at the electron microscopic level, but most exhibit large differences in both morphology and chemical structure. Some authors have suggested that the protein structures of all filamentous plant viruses are similar. A better argument has been made that most fall into one of two groups, the rigid rods or the flexible filaments [19]. Arguments have been made from protein sequence information that the tobamoviruses, the tobraviruses, and the furoviruses share a common protein fold, the four α-helix bundle [20,21]. But although this postulate is probably true, the amino acid sequences and protein chain lengths of viruses in different groups are so different that there must be major differences in the structures, too great to predict without specific structure determinations. And, as with most filaments, those structures can only be determined satisfactorily by fibre diffraction.

Good diffraction patterns have been obtained from a few viruses. In 1965, Finch [22] published patterns from the tobravirus pepper ringspot virus (at that time called tobacco rattle virus, CAM strain) and the hordeivirus barley stripe mosaic virus. The diffracting specimens were made by the method of Gregory and Holmes [3]. Diffraction patterns from dried fibres were obtained for a number of potexviruses, including potato virus X (PVX) [23] and papaya mosaic virus (PMV) [24], by Tollin and his colleagues. Most of the patterns were not good enough for high resolution structure determination, however, and none were used for more than the determination of the helical symmetry and, in one case [22], an estimate of a radial density distribution. None of the investigations was continued, and there has been little or nothing published in this field for the past twenty years. Nevertheless, there continues to be great interest in these viruses, particularly in the potexviruses. Potexviruses can accommodate large insertions in their coat proteins [25], and consequently have great potential for large-scale, inexpensive production of vaccines and other therapeutically and biotechnologically useful peptides. Designing suitable insertions, however, requires knowledge of the viral structure.

This topic should not be left without noting that there have been successful studies of the filamentous bacteriophages. All of the bacteriophages studied have simple, highly α-helical protein structures and relatively small coat proteins, so structures could be determined by model building and refinement [26]. Dried fibre samples were oriented in strong magnetic fields, and the most recent structures [27,28] have been refined using molecular dynamics methods [12].

Problems and solutions

Why are the tobamoviruses such ideal subjects for fibre diffraction analysis, while other filamentous plant viruses are so obdurate?

Despite the many years that were required and the great difficulties that had to be overcome to determine its structure, TMV is an unusually investigator-friendly virus. It is easy to grow (yields of 1 g from 1 Kg of tissue are not unusual), exceptionally stable (we have samples in our laboratory that are decades old), very soluble, and relatively insensitive to radiation. It is a rigid rod, and its aspect ratio of 15 appears to be close to ideal

	symmetry (u/t) (subunits/turns)	**radius(Å)(r)**	**r/u**
TMV	49/3	90	1.8
PVX	35/4	65	1.8
TRV	76/3	110	1.4
Pf1	27/5	30	1.1
microtubules	13/4	150	11.5

Table 1: Intensity overlap (approximately r/u) induced by cylindrical averaging in helical assemblies. Symmetries of TRV and PVX are best estimates.

for orientation. But the flexible filamentous bacteriophage Pf1 has an aspect ratio of 300. Large aspect ratios and flexibility are not insuperable obstacles to orientation. Furthermore, aspect ratios can be modified by shearing or genetic modification if necessary. Flexibility is more difficult to control, although it may be altered by solution conditions, genetic modification, or magnetic orientation.

Namba's group has had considerable success orienting bacterial flagella for fibre diffraction using a combination of centrifugation and magnetic orientation [29,30]. In some cases, they have achieved orientations as good as 0.6°. It seems reasonable, given the morphological similarities between flagella and some of the flexible filamentous plant viruses, to hope that viruses might also respond to these treatments.

Symmetry is not a limitation in fibre diffraction of plant viruses. The degree of intensity overlap induced by cylindrical averaging is well approximated by the ratio of the filament radius to the number of subunits in the helical repeat. This ratio (Table 1) does not vary greatly among viruses, in contrast with some other filamentous assemblies.

The problems in working with filamentous viruses are related either to small yields of viruses or to biochemical problems such as aggregation, which in turn are usually related to surface charge. We have had some limited success modifying surface charge chemically, and we have also made some simple genetic modifications (for example, removing short terminal segments from the coat protein chain). Nevertheless, at this time, the best candidates for fibre diffraction analysis are still those viruses that can be produced in relatively large quantities, and are highly soluble. These criteria suggest that after the tobamoviruses, the best fibre diffraction specimens should be the potexviruses.

Recent work with potexviruses

We have directed our efforts toward developing PVX and PMV as fibre diffraction subjects. Both of these viruses are available in high yields, and both are very soluble.

PMV was purified from infected papaya trees using a protocol adapted from that of Erickson and Bancroft [31]. The modifications included the use of protease inhibitors and reducing agents. PVX was purified from infected tobacco plants (*N. clevelandii*) using a procedure modified from that of Goodman [32]. Again, protease inhibitors and reducing agents were used. Details of these purifications will be published elsewhere.

Sols were drawn into 0.5 mm glass capillaries from soft pellets that had been centrifuged for 24 hours at

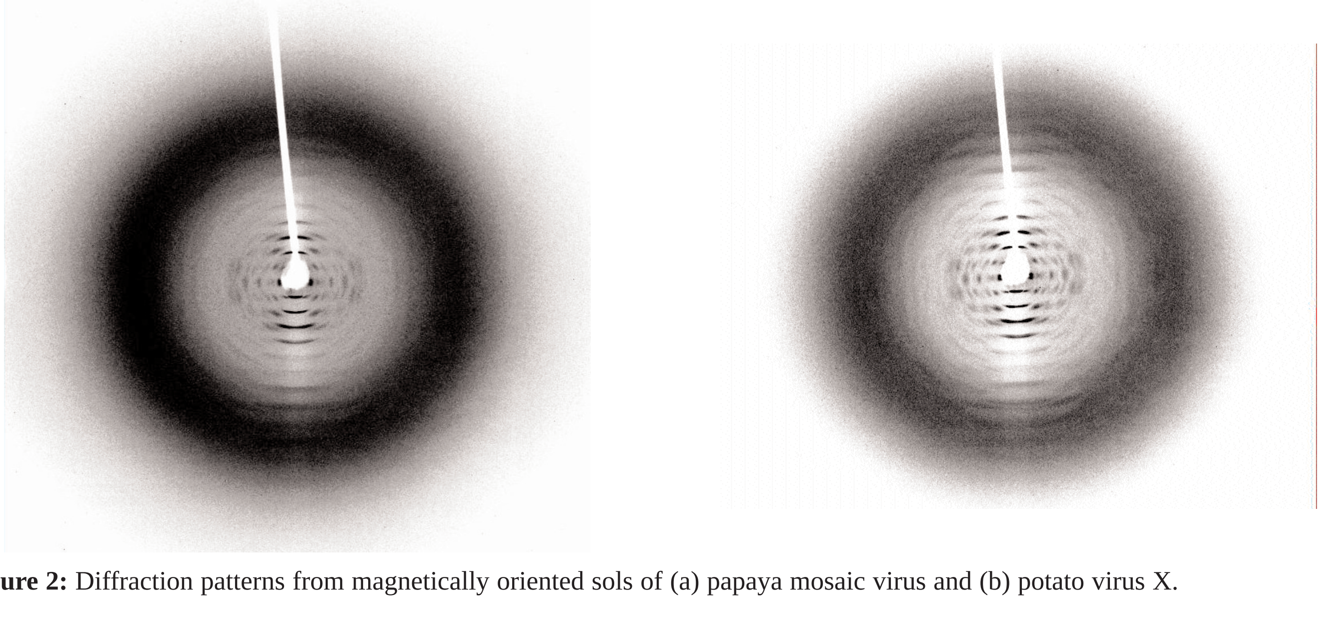

Figure 2: Diffraction patterns from magnetically oriented sols of (a) papaya mosaic virus and (b) potato virus X.

11,000 g. The ends of the capillaries were sealed, and the capillaries were centrifuged for 72 hours at 2000 g in a swinging bucket rotor, following procedures similar to those of Yamashita, Suzuki, and Namba [30]. The dilute regions at the top of the sols were removed using a smaller capillary, and the capillaries containing the sols were sealed. They were then left in a 13.5 Tesla magnetic field for 62 hours. Diffraction patterns were recorded using a Rigaku RU200 X-ray generator and an R-Axis II imaging plate detector.

Diffraction patterns from some of the best-oriented samples of PMV and PVX are shown in Figure 2. The mean disorientation of the PMV sample (Figure 2a) is about 6°; of PVX (Figure 2b), about 5°.

These diffraction patterns are not sufficiently good for high resolution structure determination, but they are significantly better than any previously obtained. Furthermore, there are excellent possibilities for further improvement. It is clear that the potexviruses respond well to magnetic orientation, and particularly to the combination of centrifugation and magnetic orientation developed by Namba's group. The time of exposure to the magnet in these experiments was much less than optimal [30], and it seems likely that the concentration of the viruses was also less than ideal. Experiments with both viruses are continuing.

Acknowledgements

We thank Keiichi Namba for valuable discussions and Winston Chapman and Amy Kendall for technical assistance. This work was supported by NSF grants MCB-9809879 and INT-9602486.

References

[1] Bawden, F.C., Pirie, N.W., Bernal, J.D. and Fankuchen, I., *Nature* (1936) 138, 1051-1053.
[2] Bernal, J.D. and Fankuchen, I., *J. Gen. Physiol.* (1941) 28, 111-165.
[3] Gregory, J. and Holmes, K.C., *J. Mol. Biol.* (1965) 13, 796-801.
[4] Namba, K., Pattanayek, R. and Stubbs, G. *J. Mol. Biol.* (1989) 208, 307-325.
[5] Makowski, L., *J. Appl. Cryst.* (1978) 11, 273-283.
[6] Caspar, D.L.D., *Nature* (1956) 177, 928-928.
[7] Franklin R.E., *Nature* (1956) 177, 928-930.
[8] Stubbs, G. and Diamond, R., *Acta Cryst.* (1975) A31, 709-718.
[9] Stubbs, G. and Makowski, L., *Acta Cryst.* (1982) A38, 417-425.
[10] Pattanayek, R. and Stubbs, G., *J. Mol. Biol.* (1992) 228, 516-528.
[11] Stubbs, G., Namba, K. and Makowski, L., *Biophys. J.* (1986) 49, 58-60.
[12] Wang, H. and Stubbs, G., *Acta Cryst.* (1993) A49, 504-513.
[13] Namba, K. and Stubbs, G., *Acta Cryst.* (1987) A43, 533-539.
[14] Stubbs, G., *Acta Cryst.* (1989) A45, 254-258.
[15] Millane, R.P., *Acta Cryst.* (1989) A45, 573-576.
[16] Wang, H. and Stubbs, G., *J. Mol. Biol.* (1994) 239, 371-384.
[17] Wang, H., Culver, J.N. and Stubbs, G., *J. Mol. Biol.* (1997) 269, 769-779.
[18] M.H.V. van Regenmortel, C.M. Fauquet, D.H.L. Bishop, E.B. Carstens, M.K. Estes, S.M. Lemon, J. Maniloff, M.A. Mayo, D.J. McGeoch, C.R. Pringle, R.B. Wickner (eds.) *Virus Taxonomy: Seventh Report of the International Committee on Taxonomy of Viruses.* (Academic Press, San Diego, 2000).
[19] Dolja, V.V., Boyko, V.P., Agranovsky, A.A. and Koonin, E.V., *Virology* (1991) 184, 79-86.
[20] Goulden, M.G., Davies, J.W., Wood, K.R. and Lomonossoff, G.P., *J. Mol. Biol.* (1992) 227, 1-8.
[21] Chen, J., Torrance, L., Cowan, G.H., MacFarlane, S.A., Stubbs, G. and Wilson, T.M.A., *Phytopathology* (1997) 87, 295-301.
[22] Finch, J.T., *J. Mol. Biol.* (1965) 12, 612-619.
[23] Tollin, P., Wilson, H.R., and Bancroft, J.B., *J. Gen. Virol.* (1980) 49, 407-410.
[24] Tollin, P., Bancroft, J.B., Richardson, J.F., Payne, N.C. and Beveridge, T.J., *Virology* (1979) 98, 108-115.
[25] Santa Cruz, S., Chapman, S., Roberts, A.G., Roberts, I.M., Prior, D.A.M. and Oparka K.J., *Proc. Natl. Acad. Sci. USA* (1996) 93, 6286-6290.
[26] Nambudripad, R., Stark, W. and Makowski, L., *J. Mol. Biol.* (1991) 220, 359-379.
[27] Gonzalez, A., Nave, C. and Marvin, D., *Acta Cryst.* (1995) D51, 792-804.
[28] Welsh, L.C., Symmons, M.F., Sturtevant,

J.M., Marvin, D.A. and Perham, R.N., *J. Mol. Biol.* (1998) 283, 155-177.
[29] Yamashita, I., Hasegawa, K., Suzuki, H., Vonderviszt, F., Mimori-Kiyosue, Y. and Namba, K., *Nature Struct. Biol.* (1998) 5, 125-132.
[30] Yamashita, I., Suzuki, H. and Namba, K., *J. Mol. Biol.* (1998) 278, 609-615.
[31] Erickson, J.W. and Bancroft, J.B., *Virology* (1978) 90, 36-46.
[32] Goodman, R., *Virology* (1975) 68, 287-298.

Crystallisation in block copolymer melts: soft-hard templating

J.Patrick. A. Fairclough[1], Shao-Min. Mai[2], Mark W. Matsen[3], Wim Bras[4], Loic Messe[1], Simon Turner[1], Anthony Gleeson[5], Colin Booth[2], Ian W. Hamley[6] and Anthony J. Ryan[1]

[1].Dept of Chemistry, University of Sheffield, Sheffield S3 7HF, UK.

[2].Dept of Chemistry, University of Manchester, Manchester M13 9PL, UK

[3].Polymer Science Centre, University of Reading, Reading RG6 6AF, UK.

[4].Netherlands Organisation for Scientific Research, DUBBLE CRG, ESRF, F38043, Grenoble Cedex, France.

[5].CLRC Daresbury Laboratory, Warrington, WA4 4AD, UK.

[6].School of Chemistry, University of Leeds, Leeds LS2 9JT, UK.

The crystallisation of shear oriented oxyethylene/oxybutylene (E/B) diblock copolymers has been studied by simultaneous SAXS and WAXS. Crystallisation of ordered melts can be accompanied by a change in length scale and retention of the melt orientation. Lamellar melts crystallise with an increase in length scale with multiply-folded E blocks and the B blocks slightly stretched from their melt conformation. Crystallisation from oriented gyroid melts leads to an increase in length scale with preferred melt directions being selected. The retention of layer planes on crystallisation from an ordered melt is caused by the local stretching of chains and the locally one dimensional structure, despite the relative strengths of the structural process. We demonstrate that an interfacial preordering effect can cause crystallographic register to jump length scales in a soft matter system showing epitaxial crystallisation.

Introduction

Self-assembly of amphiphilic molecules provides one of the fundamental structure directing processes for building hierarchical structures in nature[1]. The universality of pattern formation by lipid membranes, lyotropic and thermotropic liquid crystals, and block copolymers[1-3], all soft-structures that are closely related to biological materials, is striking. Classical structures of lamellae, hexagonally ordered cylinders and cubic arrays of spheres are well established[1,4] and it is easy to visualise how they act as templates. Complex cubic structures, such as the bicontinuous double diamond (Pn3m) and gyroid (Ia3d) have been found in lyotropic liquid crystals[2] and in block copolymer melts[5-7] and solutions[8] as well as in naturally occurring lipids[1,9,10]. These also act as templates but in a more subtle manner. Here we report a transformation from a soft structure (block copolymer melt) to a hard structure (semi-crystalline block copolymer) with conservation of preferred lattice directions and a doubling of the lattice spacing.

How can one make a large hierarchical structure? Hard (crystalline) materials cannot form large scale structures directly but need soft materials, which have the ability to self-assemble, to act as templates and direct structure formation. Another important question is, what circumstances allow the retention of crystallographic register, especially when the free energy changes associated with the two processes, templating and hard material growth are quite different? Structures in lipids, liquid crystals and block copolymers are typical of "soft" condensed matter where the material has a large scale structure with crystallographic register, but where the local atomic structure is liquid-like and disordered. These large scale structures are formed due to a balance of forces minimising the Gibbs energy and are truly at dynamic equilibrium[10]. In the case of block copolymers the important features are the configurational entropy of the molecules and the formation of interfacial area. The theory, which describes these phenomena, is well developed[11] and gives accurate predictions of phase behaviour. The gyroid (Ia3d) phase has been observed between the lamellar and hexagonal packed cylinder phases in the diblock copolymer phase diagram close to the order-disorder transition[6,12]; it comprises cylindrical channels of the minority material joined by 3-fold connectors, two such lattices with opposite chirality interpenetrate through a matrix.

One important class of structure direction is soft-soft templating between mesoscopic structures. Transformations between adjacent gyroid and lamellar or hexagonal phases have attracted attention because they are related to the structural transitions which occur when cells fuse or rupture. A number of studies of anionic and non-ionic surfactants have provided evidence of epitaxial relationships in transformations of gyroid to lamellar[13,14] with growth proceeding along [111] directions without change in lattice parameters. This is thought to be related to the orientation of the 3-fold connectors within the unit cell. A similar epitaxial relationship has been observed for a diblock copolymer melt[15] where the lamellar phase grows from the gyroid without long-range transport of material and with preservation of orientation in some layer planes. In these epitaxial transformations the lattice spacing is either conserved or changes smoothly as the high-symmetry cubic structure transforms into the lower symmetry layered or rod-like structure. This is usual in structural transformation in both soft- and hard-condensed matter. Soft-hard templating, by block copolymers and surfactants, of porous and composite structure on the nanometer scale has provoked much interest for formation of mesostructured inorganic[16,17] and organic materials[18]. In these cases there is no crystallographic register between the soft template and the growing hard phase and structural transformations are observed as chemical reactions change the thermodynamic interactions between components[18]. However, if epitaxy is observed, then there is nearly always a continuous change in lattice parameters.

Experimental

The amphiphilic system reported here has been extensively studied including self-assembly in dilute and concentrated aqueous solutions[19], microphase separation in the melt[20] and crystallisation behaviour[21]. Block copolymers with narrow molecular weight distributions were prepared by sequential anionic polymerisation of ethylene oxide (E) followed by 1,2-butylene oxide (B). Vacuum line and ampoule techniques were used throughout and the copolymers were characterised by gel permeation chromatography and ^{13}C NMR spectroscopy. The molecular characteristics are expressed in E_mB_n notation where the subscripts denote the average numbers of repeat units.

Simultaneous SAXS/WAXS measurements were made on beamline 16.1 at the Daresbury Synchrotron Radiation Source or on the DUBBLE beamline at the European Synchrotron Radiation Source (ESRF). At Daresbury the incident beam was 1.4 Å and a Fuji image plate at 10 cm was used to record the WAXS pattern with a 10 mm hole to allow the SAXS pattern to develop out at 3 m for recording on an area detector. At the ESRF the incident beam was 1.0 Å and an area detector was used to record the SAXS at 4 m. The sample thickness was 1 mm and the beam passed through a hole of 3 mm which was covered with Kapton^{TM} tape. The sample was oriented by shearing the ordered melt, for 50 cycles at approximately 1 Hz and 200% strain, in a heated cell consisting of a piece of brass with machined side grooves to allow movement of a parallel brass slider during shear. The polymer temperature was monitored by a thermocouple. Quiescent cooling after shear orientation allowed the epitaxial relationships to be observed.

Observed intensity	**<211> Azimuthal position/º**	**Predicted intensity**
1	0,180	1
1.3	28.1,151.9,208.1,311.9	1.14
3.2	70.5,109.5,250.5,289.5	1.50

Observed intensity	**<220> Azimuthal position/º**	**Predicted intensity**
3.2	0,180	1.15
1	54.7,125.3,234.7,305.3	1

Table 1: The predicted intensities from a gyroid melt randomly oriented about the [111] direction [15] compared to those observed in the azimuthal intensity measurements.

Results and Discussion

The crystallisation of melts of E_mB_n copolymers has been studied in some detail[21] and the orientation of the crystal stems perpendicular to lamellar interfaces is well established. This is soft-hard templating but with obvious epitaxial relationships. The simplest case of a copolymer with a lamellar melt phase and a lamellar semi-crystalline phase is illustrated in Figure 1a by a schematic of the molecular conformations of $E_{76}B_{38}$ in the equilibrium melt and crystallised states. In the melt the characteristic length scale, D, is that of the stretched coil with a length dependent on the radius of gyration, R_g, whereas in the crystalline state the characteristic length scale is the related to the extended chain length, L. The low temperature structure is a once-folded E block (two crystal stems) and an unfolded, stretched B block: an unfolded E chain would not be possible due to conservation of volume. The SAXS pattern in Figure 1b is obtained from a sample of $E_{76}B_{38}$ that was shear oriented prior to crystallisation. It shows first order reflections from the lamellar crystals with a d-spacing of 224 Å. There are clearly resolved 2nd, 3rd and 4th order reflections and the minimal arcing illustrates that the material is a monodomain with lamellae oriented in the shear direction. The simultaneously recorded WAXS pattern in Figure 1c confirms that the E chains are oriented perpendicular to the lamellar interfaces, the strong equatorial reflections derived from the c-axis {001} of the helical E block[22]. SAXS[21] shows a change in length scale from 109 Å in the ordered melt to 224 Å in the crystal phase, i.e. there is a step change in lattice spacing on transformation from the soft ordered melt structure to the hard semicrystalline solid structure with an approximate doubling of lattice spacing due to stretching of chains perpendicular to the lamellar interface with corresponding lateral contraction.

The terms "soft" and "hard", as applied here to the ordered melt and semicrystalline solid, are justified by the enthalpy of formation of the structures and the mechanical properties of the materials. High resolution calorimetry[23] studies on $E_{60}B_{29}$ show that the latent heat of the fusion process is 90.2 ± 2 Jg^{-1} whereas that of the order-disorder transition in the melt is 0.171 ± 0.003 J g^{-1}. The enthalpy of formation of crystals is 500 times larger than that of the ordered melt. Similarly the shear modulus of the semicrystalline polymer is 10^7 Pa whereas that of the ordered melt is 10^5 Pa.

Ordered block copolymer melts have chains that are stretched compared to the random (Gaussian) conformations[3,11]. The characteristic length of a strongly segregated melt scales with $N^{2/3}$ compared with $N^{1/2}$ for a Gaussian chain. Furthermore, the stretching is not uniform, chain segments are more strongly oriented across the interface between the two chain types. It is feasible that it is the local orientation of chain segments perpendicular to the interfaces that nucleates crystallisation. The local orientation reduces the crystallisation energy barrier (crystallisation in polymers requires development of orientational order along the chain) and promotes crystal growth. For this reason the vast majority of semicrystalline block copolymers show stems perpendicular to lamellar surfaces. The conditions for formation of other orientations and morphologies must be strongly forcing, i.e. confinement of the crystallising chains by hard walls[24,25] and with chain imperfections that prevent formation of large crystals.

The retention of orientation of layer planes on crystallisation from a lamellar ordered melt is not unexpected given the local stretching of chains and the one dimensional structure, despite the strong driving force for the transition. What is unexpected, however, is that a more complex soft structure will also direct crystallisation processes. The SAXS patterns in Figure 2 follow the transformation of a gyroid melt into a lamellar crystal. The SAXS pattern in Figure 2a was obtained following large amplitude oscillatory shear and is typical[5,6,12,15] of the gyroid morphology. The 10 spot pattern is from a directionally oriented Ia3d crystals with the zone axis along the [111] lattice direction which is oriented parallel to the shear direction[15,26]. This oriented melt structure was allowed to cool from 80°C to 20°C over a period of an hour. Orientation was maintained after shearing and many higher order reflections were sampled. Once crystallisation starts strong scattering was observed inside the 211 reflections of the melt. The example shown in Figure 2b shows simultaneous growth in two of the <211> directions. Repeated experiments (at Daresbury and the ESRF) showed crystal growth to be observed preferentially in three of the five {211} planes. These lamellar crystals are consuming the ordered melt the presence of which is confirmed since the higher orders of Ia3d are still clearly visible. Eventually (Figure 2c) the gyroid melt is nearly all consumed and higher order reflections can be seen for the lamellar crystals. There has been a transformation in two of the [211] directions of the Ia3d cubic structure with d-spacing 123 ±2 Å to an oriented lamellar structure with d-spacing 237 ± 5Å. If there is epitaxy from the Ia3d to the lamellar structure then there are 24 equivalent planes available. In this experiment we have Bragg sampled two of these planes during the crystallisation of a {111} zone oriented crystal of Ia3d melt.

In the gyroid morphology, chain stretching is uniform (within 7%)[26] across the interface between microphases and consequently crystallisation can nucleate anywhere around this surface. The absolute magnitude of the change in characteristic length on crystallisation is determined by the crystallisation temperature and block lengths, in the example given here the length scale doubles. The effective doubling of the plane separation is illustrated in Figure 3 (a, b) where unit cells are shown transforming along {111} into 2 lamellar unit cells. Figure 3c shows average segmental density profiles across the [112] and [220] directions of the gyroid phase, calculated using self-consistent field methods[4,11,26], and the density map of the structure as it would appear in the TEM looking down the {111} axis. These calculations provide strong evidence that lamellae orient along [211] directions because that is the direction in which the gyroid phase most resembles a lamellar phase.

The stretching is localised to the interface and this is where we would expect crystallisation to initiate. Statistically crystals that initiate are likely to grow fastest in the direction most able to provide room for growth, i.e. the most lamellar-like directions. Consequently, the crystallisation follows the lamellar like direction initially and then breaks out to a longer length scale. The initial crystallisation is the symmetry breaking step and retains the preferred direction of the soft cubic structure even though the length scale increases. Recent experimental and theoretical[27] work on polymer crystallisation has shown that the local structure of the polymer melt, prior to crystallisation, has a strong influence on the nature of the crystallisation process. The local orientation at the block copolymer interfaces reduces the crystallisation energy barrier causing the epitaxial relationships observed.

In Figure 4 we compare the scattering pattern from the melt and the crystals to confirm the epitaxial relationships. In Figure 4a the melt and crystal structures from a small scattering volume (0.125 mm^3) clearly illustrate that crystallisation selects the <211> directions and the lamellar peaks lie on these planes separated by 70.5 °. We suspect that there are two domains in the Bragg condition giving rise to these two sets of lamellar reflections and this gives indirect evidence of the grain size. In Figure 4b, however, there is a much larger scattering volume (2.5 mm^3) and more lamellar domains are sampled. Now three of the five [211] directions are obviously preferred and these are highlighted by the solid lines Figure 4b and by the azimuthal intensity scans in Figure 4c. In repeated crystallisation we do not observe strong crystalline reflections in the directions highlighted by the dotted lines.

The Ia3d structure obtained by large amplitude

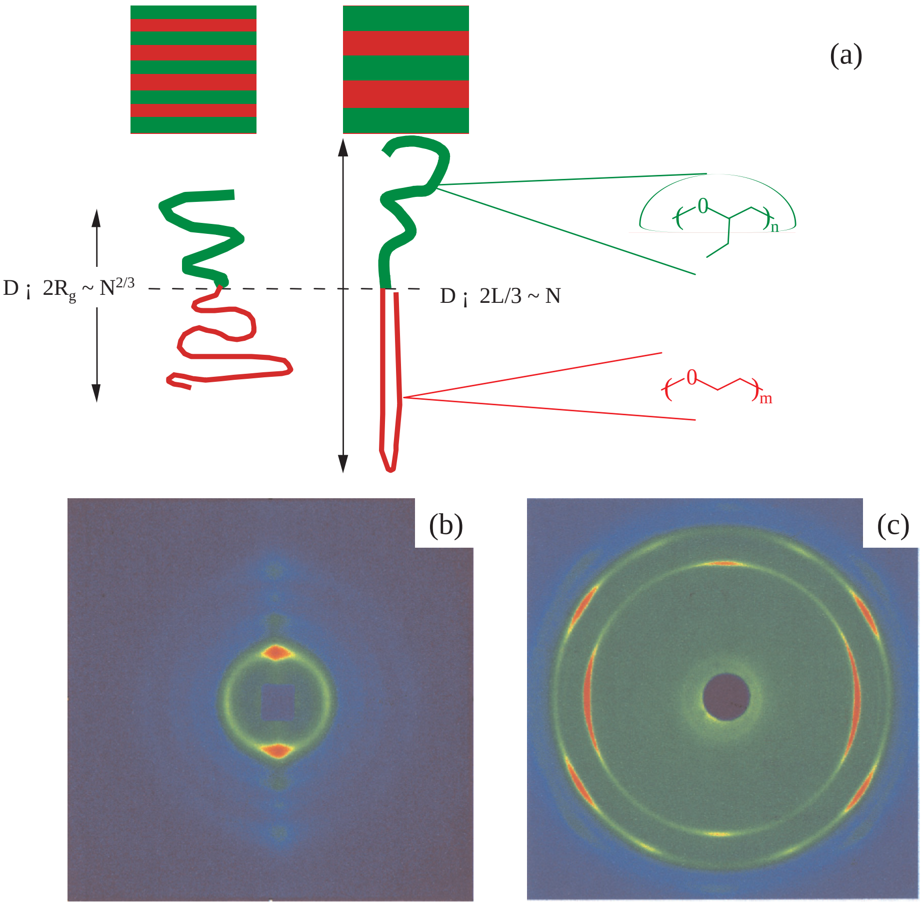

Figure 1: (a) A schematic representation of block copolymer chain conformation in the molten and crystalline states. In the disordered melt the chains are Gaussian and have a size which scales as $N^{1/2}$, whereas in the ordered melt the chains are stretched from their Gaussian conformations and have a domain spacing which scales as $N^{2/3}$. When one of the blocks crystallises into a straight stem the amorphous chains are stretched from their Gaussian conformations and have a domain spacing that scales as N. (b) Small angle X-ray scattering data from a sample of $E_{76}B_{38}$ that had been crystallised after shearing in the melt. It shows a pair of first order reflections from the lamellar crystals with a d-spacing of 224 Å. There are clearly resolved 2nd, 3rd and 4th order reflections and the minimal arcing illustrates that the material is a monodomain with lamellae oriented in the shear direction. (c) Wide angle X-ray diffraction data from a sample of $E_{76}B_{38}$ that had been crystallised after shearing in the melt. Fibre diffraction of poly(oxyethylene)[22] shows that the E chains are oriented perpendicular to the lamellar interfaces as the strong equatorial reflection is the c-axis (001 reflection) of the unit cell. Simultaneous SAXS/WAXS measurements were made on beamline 16.1 at the Daresbury Synchrotron Radiation Source using a Fuji image plate at 10 cm to record the WAXS pattern with a 10 mm hole to allow the SAXS pattern to develop out at 3 m. The sample thickness was 1 mm and the beam passed through a hole of 3 mm which was covered with Kapton^{TM} tape. The sample was oriented by shearing the ordered melt, for 50 cycles at approximately 1 Hz and 200% strain, in a heated cell consisting of a piece of brass with machined side grooves to allow movement of a parallel brass slider during shear, the polymer temperature was monitored by a thermocouple. Quiescent cooling after shear orientation allowed the epitaxial relationships to be observed.

oscillatory shear is a highly twinned body centred cubic structure with a [111] direction along the shear direction[15] The intensities predicted for the 211 and 220 reflections are given in Table 1. There are eight orientations of grains with a common [111] zone axis that are sampled to make up the observed pattern. The 211 reflections at 70.5° and the 220 reflections at 0° come from the two projections of the unit cell with the {111} planes parallel to the shear direction and the {220} planes along the shear gradient, i.e. perpendicular to the shear plates and the X-ray beam. The shear conditions used have obviously caused preferential orientation about this direction and this is seen by the fact that these reflections are at least twice as strong as predicted (see Table 1). Furthermore the samples were cooled slowly after shear orientation so the [220] direction is also preferentially aligned along the thermal gradient during crystallisation. We conclude that the sample crystallises most rapidly along a [211] direction in grains which are oriented with their <220> directions parallel to the shear and thermal gradient. Furthermore grains with this orientation in the melt are observed to be in the Bragg conditions at least twice as frequently as in a randomly rotated set of grains. Crystallisation could select these grains to

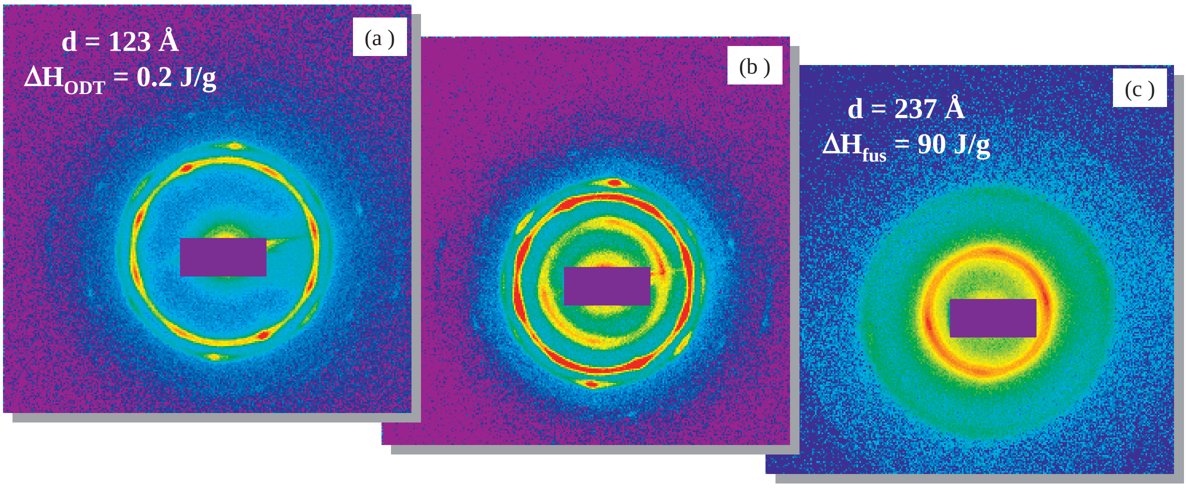

Figure 2: A series of SAXS patterns showing the transformation of a bicontinuous (Ia3d) cubic melt of $E_{75}B_{54}$ into an oriented lamellar crystal. (a) The (inner)10 spot pattern is from a 2D powder made up of grains rotated randomly around the [111] lattice direction which has become preferentially oriented parallel to the shear. (b) Once crystallisation starts strong scattering is observed inside the <211> reflections of the melt. Lamellar crystals, nucleated from the cubic melt, are observed to grow in a number of preferred directions, corresponding to the <211> and <220> reflections of the Ia3d. These lamellar crystals are consuming the ordered melt and the higher orders of the Ia3d are still clearly visible. (c) Eventually the Ia3d melt is nearly all consumed and higher order reflections can be seen for the lamellar crystals. There has been a transformation along the two crystallographic planes of the Ia3d cubic structure with d-spacing 123 ±2 Å to an oriented lamellar structure with d-spacing 237 ± 5Å.

crystallise in the thermal gradient direction, consuming the other adjacent orientations. The SAXS patterns in Figure 4a indicate that the grains are of the order of 10 µm in size and only two orientations (and possibly tens of grains) are sampled in Figure 4a. In contrast there are many grains sampled in Figure 4b where there are oriented peaks on a strong lamellar ring.

Summary and Conclusions

We have demonstrated here that an interfacial preordering effect can cause crystallographic register to jump length scales in soft-hard templating. The retention of layer planes on crystallisation from an ordered melt is caused by the local stretching of chains and the locally one dimensional structure, despite the relative strengths of the structural process. What is unexpected, however, is that a complex soft structure will also direct the crystallisation processes, selecting specific orientations. We have considered many options for this, including low-angle grain boundaries, but conclude that there is a subtlety in the local chain orientation that provides the selection process. Small soft structures (lipid membranes) directing larger hierarchical structures (bone and exoskeleton) are common in natural systems. We present here a soft matter system showing epitaxial crystallisation and length-scale jumping.

References

[1] P. Ball, *The self-made tapestry*, Oxford University Press 1998
[2] J.M. Seddon, *Biochim. Biophys. Acta.*, 1031, 1 (1990).
[3] I.W. Hamley, *The Physics of Block Copolymers*, Oxford University Press 1998
[4] F.S. Bates, G.H. Fredrickson, *Ann. Rev. Mat. Sci.*, 26, 501 (1996).
[5] E.L. Thomas, R.L. Lascanec, *Philos.Trans.R. Soc. London A*, 348, 149 (1994).
[6] S. Förster, A.K. Khandpur, J. Zhao, F.S. Bates, I.W. Hamley, A.J.Ryan, W. Bras. *Macromolecules*, 27, 6922 (1994).
[7] E.L. Thomas, D.M. Anderson, C.S. Henkee, D. Hoffman, *Nature*, 334, 598 (1988).
[8] D.A. Hajduk, M.B.Kossuth, M.A. Hillmyer, F.S. Bates, *J Phys Chem B*, 102, 4269

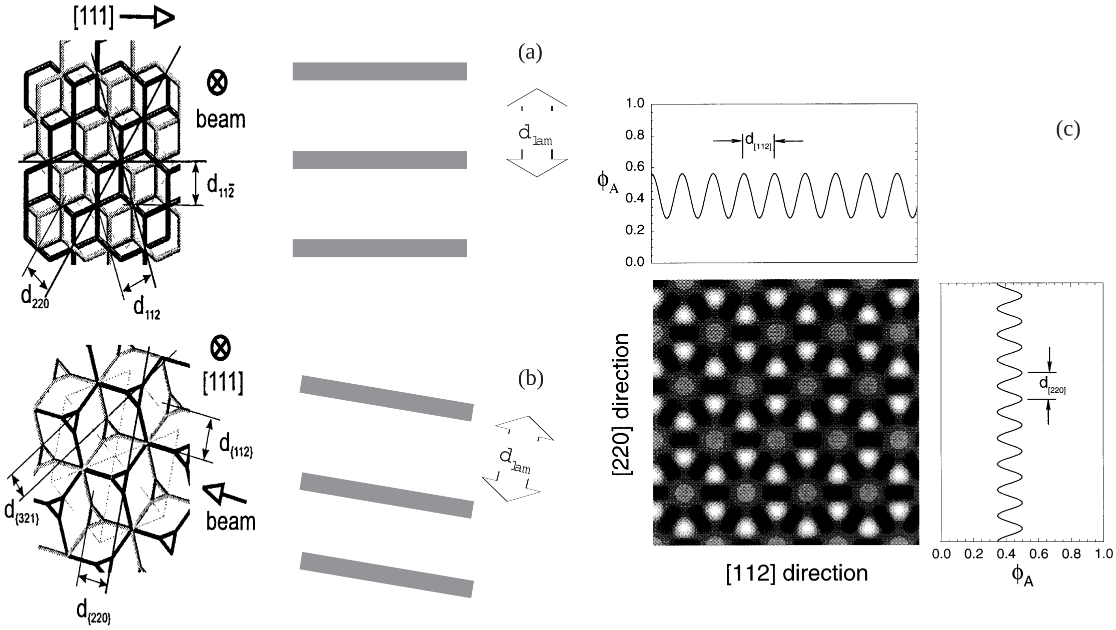

Figure 3: Schematics of the Ia3d morphology showing the orientation of the 3-functional connectors and the principal crystallographic directions. (a) A 2-dimensional projection [15] that shows the <112> and the <11-2> reflections that are strongest in Figures 2a and 4a which transform into aligned lamellae by crystallisation along every second <11-2> plane. (b) A view along the [111] direction [15] displaying {211}, {220} and {321} planes which transform into aligned lamellae by crystallisation along every second {211} plane. (c) A 2-D image of composition, $\Phi_A(r)$, averaged in the [111] direction with the corresponding 1-D plots resulting from the average of $\Phi_A(r)$ in the [112] and [220] directions. This establishes that the gyroid phase is most lamellar-like in the [112] direction because the uppermost 1-D plot has the stronger oscillation.

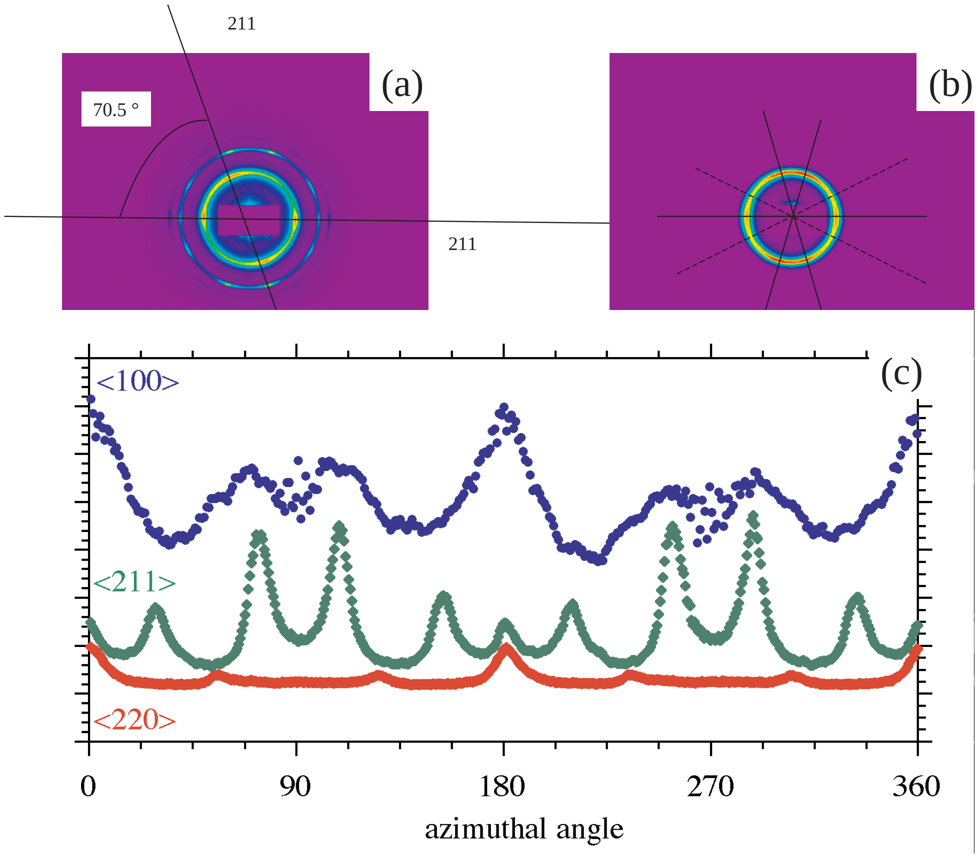

Figure 4; The relationship between the gyroid melt structure and the semicrystalline structure. (a) Superimposition of the SAXS patterns from the Ia3d melt and fully crystalline sample showing that the two lamellar orientations observed are consistent with the 112 and 11-2 reflections. The lamellar reflections are separated by 70.5 ° as expected for Ia3d [15]. The scattering measurements are made on a small scattering volume of 0.125 mm^3 and sample only a small number of grains. (b) Scattering from the same fully crystalline sample with a much larger scattering volume of 2.5 mm^3. The solid lines show the <211> reflections that are followed by crystallisation, the dotted lines those not so obviously sampled. It should be noted that the peaks in the crystalline sample are superimposed on a bright ring implying some loss of overall orientation. (c) Azimuthal scans (with respect to the meridional direction) showing the relative intensities of the <211> and <220> in the melt compared to the crystalline lamellae <100> peaks in the solid.

(1998).

[9] M. Clerc, P. Laggner, A.-M. Levelut, G. Rapp, *J. Phys. France II*, 5, 901 (1995).

[10] V. Luzzatti, *Nature*, 218, 1031 (1968).

[11] M.W. Matsen, F.S. Bates, *Macromolecules*, 29, 1091 (1996).

[12] D.A. Hajduk, P.E. Harper, S.M. Gruner, C.C. Honeker, G. Kim, E.L. Thomas, L.J. Fetters, *Macromolecule*, 27, 4063 (1994).

[13] Y. Rancon, J. Charvolin, *J. Phys. Chem.*, 92, 2646 (1988).

[14] P. Kekicheff, B. Cabane, *Acta. Crystallogr. B*, 44, 395 (1988).

[15] M.E. Vigild, K. Almdal, K. Mortensen, I.W. Hamley, J.P.A. Fairclough, A.J. Ryan, *Macromolecules*, 31, 5702 (1998).

[16] A. Firouzi, D. Kumar, L.M. Bull, T. Besier, P. Sieger, Q. Huo, S.A. Walker, J.A. Zasadzinski, C. Glinka, *Science*, 267, 1138 (1998).

[17] D. Zhoa et al, *Science*, 279, 548 (1998).

[18] P.M. Lipic, F.S. Bates, M.A. Hillmyer, *J.Am. Chem. Soc.*, 120, 8963 (1998).

[19] A. Kelarakis, W. Mingvanish, C. Daniel, H. Li, V. Havredaki, C. Booth, I.W. Hamley, A.J. Ryan, *Phys. Chem. Chem. Phys*. 2, 2755 (2000).

20 S.M. Mai, J.P.A. Fairclough, K. Viras, P.A. Gorry, I.W. Hamley, A.J. Ryan, C. Booth, *Macromolecules*, 30, 8392 (1997).

21 S-M. Mai, J.P.A Fairclough, N.J. Terrill, S. Turner, I.W. Hamley, M.W.; Matsen, A.J. Ryan, C. Booth. *Macromolecules* 31, 8110-8116, (1998).

22 Y Takahashi, H. Tadokoro, *Macromolecules*, 6, 672 (1973).

23 V.P. Voronov, V.M. Buleiko, V.E. Podneks, I.W. Hamley, J.P.A.Fairclough, A.J.Ryan, S- M. Mai, B-X. Liao,, *Macromolecules*, 30, 6674 (1997).

24 I.W. Hamley, J.P. Fairclough, N.J. Terrill, A.J. Ryan, P. Lipic, F.S. Bates, E. Towns-Andrews, *Macromolecules*, 29, 8835 (1996).

25 D.J. Quiram, R.A. Register, G.R. Marchand, D.H. Adamson, *Macromolecules*, 31, 4891 (1998).

26 M.W. Matsen, F.S. Bates, *Macromolecules*, 29, 7641(1996).

27 P.D. Olmsted, W.C.K. Poon, T.C.B McLeish, N.J. Terrill and A.J. Ryan, *Phys. Rev. Lett*., 81, .373 (1998).

Small angle X-ray scattering reveals changes of bone mineral habit and size in archaeological bone samples

T. Wess[1], I. Alberts[1], G. Cameron[1], C. Laurie[1], J. Orgel[1], J. Hiller[2], C. Nielsen Marsh[2], V. De La Cruz Balthazar[3], M. Drakopoulos[4], A. M. Pollard[3], and M. Collins[2]

[1] Centre for Extracellular Matrix Biology, Dept. of Biological Sciences, University of Stirling, Stirling FK9 4LA, UK.

[2] NRG Unit Fossil Fuels & Env. Geochem. Drummond Building, University of Newcastle-upon-Tyne, UK.

[3] Department of Archaeology, University of Bradford, Bradford, BD7 1DP, UK.

[4] ESRF, Grenoble, 6 rue Jules Horowitz, 38043Grenoble, France.

X-ray scattering provides a powerful non-destructive technique capable of providing important information about the size, habit and arrangement of mineral crystals in bone. In the case of archaeological bone the changes in the habit of the apatite crystals and recrystallised material may reflect the changes in bone environment that have occurred since death. In the study presented here we have examined a variety of archaeological bones by small-angle X-ray scattering to show the alterations in bone habit that can be adopted after 'diagenetic remodelling'. Furthermore we show that the use of small-angle scattering microfocus technology allows us to probe into the fine structure alterations that can occur in bone as a result of microbial attack and mineral recrystallisation. The integrity of the bone crystallites has a strong correlation with the ability to extract other biomolecules from bone such as osteocalcin and DNA. Alterations in the crystallite habit may explain the success of macromolecule recovery from archaeological samples.

In vivo, bone consists of a matrix of collagen fibrils which provides a framework for calcium hydroxyapatite organisation. The hydroxyapatite is found as discrete needle or plate-like crystal structures with a mean thickness of 25-35 nm (Fratzl et al, 1991). The long term archaeological degeneration of bone involves a number of processes indicating that specific forms of geological or microbial degeneration have occurred (Bell et al, 1996; Nielsen-Marsh et al, 2000). These processes involve the remodelling of the mineral and collagen matrix of bone. However, the exact nature of the rearrangements is poorly defined. Some processes, such as cooking or cremation, are expected to have a more global effect on crystal habit, whereas bacterial action is expected to produce focal changes in bone character on the micron lengthscale (Hackett, 1981). In order to develop an understanding of properties such as differential diagenetic durability between and within the heterogeneous architecture of bones, it is essential to provide information about changes in crystal habit, orientation and statistical distribution of mean thickness. This will lead to an understanding of the archaeological remodelling that occurs at the molecular level and manifests at the level of macroscopic bone integrity.

Small-angle X-ray diffraction is capable of determining the statistical habit of mineral in tissues such as bone (Fratzl et al, 1996(a)). The technique measures the scattering from the collection of crystals within a bone that are bathed by an X-ray beam. The shape of the scattered X-rays contains two key pieces of information, the invariant and the Porod region. The combination of the two allows parameters such as the average crystal thickness and crystal shape to be determined (Fratzl et al, 1996(a)). This has already proved to be successful in examining the effects of osteoporosis (Fratzl et al, 1994). The technique is less subjective than electron microscopy and also does not rely on factors such as the degree of crystallinity that hampers comparisons made by high angle X-ray diffraction (Ziv and Weiner, 1993).

The development of microfocus techniques (Snigirev and Snigireva, 1995) and highly sensitive X-ray detectors, also allows crystallite texture to be analysed over a micron size range in thin sections of bone where focal changes in mineral habit may have occurred with time. In this study we present data showing the typical shape of X-ray scattering obtained from bones of modern animals and we compare these shapes with the alterations that can take place in both well-preserved and highly remodelled archaeological bones. The use of X-ray microfocus technology allows the textural changes to be exhibited on a µm length-scale and indicates that the local texture of archaeological bone can be highly variable. Macroscopic measurements, such as total organic content and porosity, commonly made on macroscopic samples of archaeological bone, may be obscuring a number of local features which possibly hold the key to differentiation between different

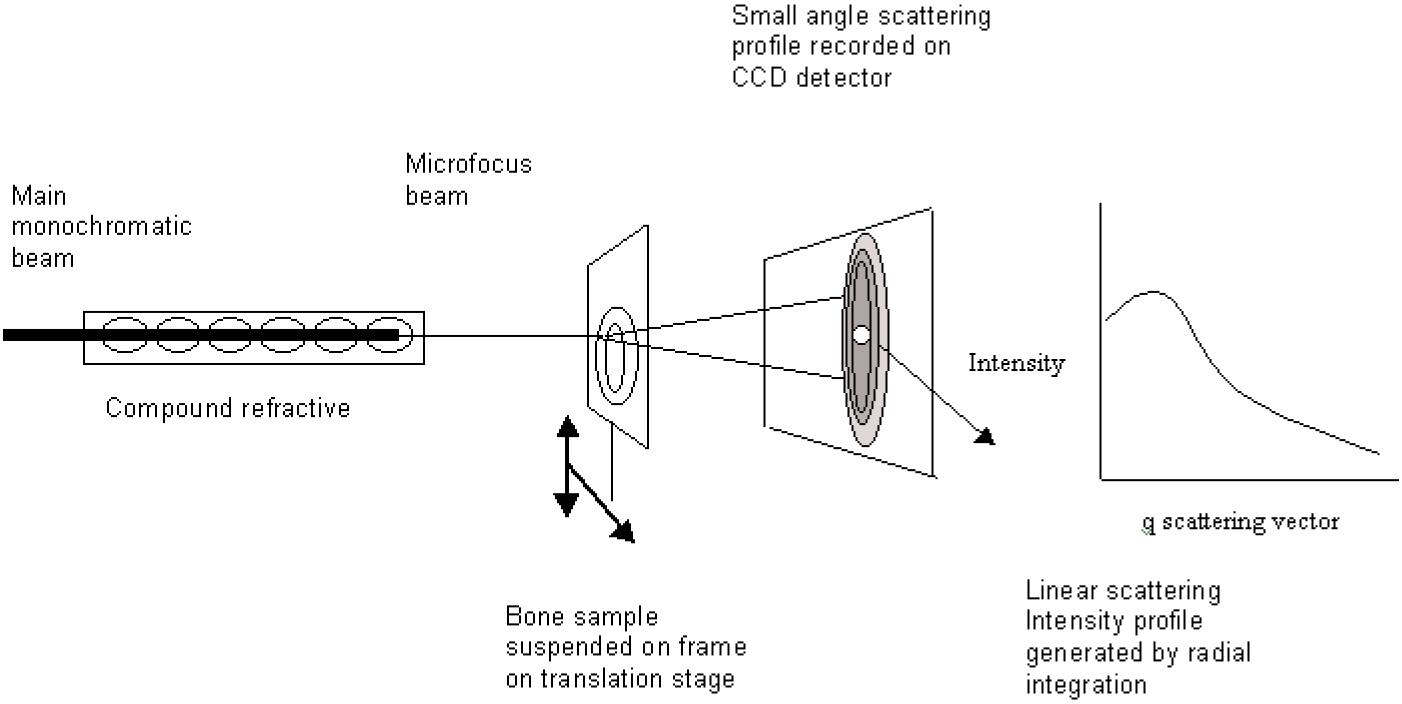

Figure 1: A schematic diagram of the small-angle X-ray scattering geometry for microfocus experiments. The highly parallel monochromatic X-ray beam is defined by an optical element (the compound refractive lens) and used to scan the bone samples. The nature of small-angle diffraction means that the scattered X-rays are close to the main X-ray beam and long camera lengths are used to help resolve the angular scattering components. Data are collected on a CCD detector and then processed as described in the text.

remodelling processes

Materials and Methods

Details of samples and data collection. In this study, 30 archaeological and 10 modern bone samples were analysed. The bones were supplied from the archaeological archives of the Universities of Bradford, Newcastle and Sheffield. The samples exhibited a wide range of deterioration; some bones appeared to be well preserved as judged by microscopic examination of their histology, whereas others were friable and contained no recognisable bone ultrastructural features. Modern bovine femur cortical bone was used as a control sample The archaeological sample used in microfocus studies was a human femur believed to be aged 1550BP.

All samples were cut on a Leica rotary saw to thicknesses of 50-70µm, and mounted on mica squares with cyanoacrylate at points where diffraction data were not to be collected. X-ray scattering experiments were conducted at beamline 2.1 of the CCLRC Daresbury synchrotron with complementary microfocus experiments conducted at ID22 of the ESRF Grenoble. At beamline 2.1 at the CCLRC Daresbury synchrotron (Cheshire, UK; Towns-Andrews et al, 1989), a 6m camera length was used to resolve the small-angle scattering profile from the main beam. The spot size at the sample was 500 µm x 2000 µm. The X-ray scattering profile was recorded on a two-dimensional gas filled detector system (for details see Lewis, 1994).

At the ESRF a compound reflective lens (Snigirev et al, 1996) was used to generate a microbeam of size 2µm vertically by 7µm horizontally and with a flux of 5.10^9 photons/s, at a wavelength of 0.086 nm. The micro-SAXS patterns were observed with a Fuji photonics low temperature CCD Detector with a recording q range of 0.016 - 4.0 nm^{-1}, where q is the scattering vector $q = 2\pi\sin\theta/\lambda$, θ is the scattering angle and λ the wavelength of incident radiation (λ= 0086nm).

Prior to microfocus scattering, the defocused monochromatic X-ray beam was used to produce an X-ray transmission image of each bone sample. Using the microfocus beam, bones were scanned along a 200 µm-long predefined line at 21 regular intervals that covered regions of what were judged to be intact or modified bone structure. Each individual exposure was in the range of 1-5 seconds. A schematic diagram of the microfocus beamline is shown in Figure 1.

Data treatment The analysis of X-ray small-angle scattering profiles was conducted using the approach of Fratzl et al (1996(a); 1991). Briefly, small-angle

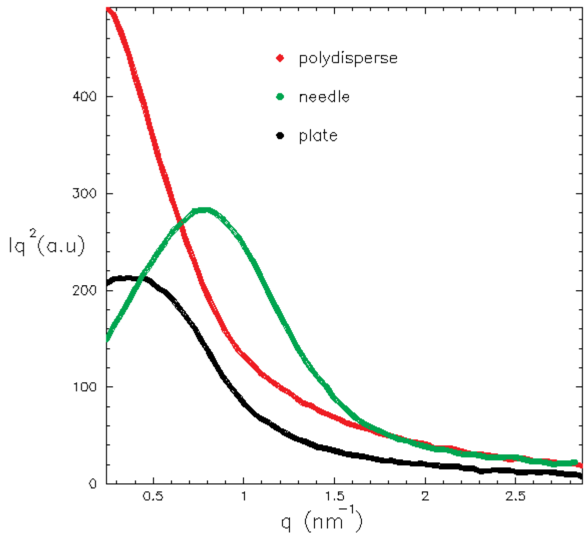

Figure 2: X-ray scattering profiles of bone samples: examples of scattering profiles that show the representative curves corresponding to different crystallite habits. The data are plotted as the intensity multiplied by q^2 where $q = 2\pi \sin\theta/\lambda$ (λ is the wavelength). This is known as a Kratky plot. The profiles shown represent the three main crystalline morphologies that are observed in the bone samples used in this study. The profile marked in red typifies scattering from polydisperse crystal habits. The profile shown in green is typical of needle-like crystals. A third example (scattering profile shown in black) typifies scattering from plate-like crystals.

diffraction profiles were corrected for the dark field current of the detector and were spherically averaged. Two-dimensional images were converted to linear intensity profiles by rebinning data radially in the q range from 0.01 - 3 nm^{-1}. Each profile had an appropriate background profile subtracted, and the resulting linear profiles I(q) converted into Kratky plots ($I(q)q^2$ against q) and Porod plots ($I(q)q^4$ against q^4) that allowed the average crystallite thickness to be defined (see Figure 2).

The scattering profiles indicated that in some cases the habit of the bone varied over the length of the scanned region. This variation was investigated further and quantified. It is preferable to rescale the scattering profiles according to crystal thickness (T) which leads to the definition of a new horizontal axis parameter, x = qT. The data were renormalized using the total scattering integrals to give the crystal form factor G(x), such that

$$\int G(x)dx = 1$$

Plots of G(x) against x were superimposed and were used to assess the change in the crystal habit, since they represent the scattering function in relation to the form factor of the crystallite. Quantification of the crystal habit was made by comparing the resultant scattering curve to a Lorenzian curve and calculating the residual η, such that $\eta = [G(x) - G_0(x)]^2\,dx$, where G_0 is the normalised Lorentzian function $4 / [\pi(4+x^2)]$. For more detail see Fratzl et al (1996(a)).

Crystal habits such as needles or plates have different characteristic low-angle scattering interactions with X-rays. The size of the crystals also has an effect on the scattering profile. In X-ray scattering, the angular deviation of scatter has an inverse relationship with size. From this, the position and shape of an X-ray scattering curve can be used to determine the average shape and size of crystallites in a sample.

Multiplying the observed X-ray scattering intensity by the square of the corresponding q value (a parameter derived from the scattering angle) gives a Kratky plot as shown in Figure 2. Needle and plate-like crystals give differently shaped Kratky plots. In the case of plates, the form factor that corresponds to this shape has an intensity profile that decays by a factor of q^{-2} at values close to q=0. This leads to a flattened region in the Kratky plot at low q values. In the case of a needle crystal habit, the X-ray scattering form factor of this shape has an intensity that decays in proportion to q^{-1} at low q values, leading to a positive slope at low q in the Kratky plot. Since the plot involves the product of I and q^2, the differences in the scattering profiles are enhanced and it is relatively easy to distinguish between the two principal crystal types in this study. A further profile that is observed corresponds to a crystal morphology that is neither representative of needle nor plate-like crystals. This scattering curve closely corresponds to a Lorenzian distribution and is thought to correspond to a polydisperse mixture of crystal shapes incorporating large crystal sizes that cannot be studied by small-angle scattering. A thickness measurement, however, can still be made for the part of the crystallite population that is within the domain of small-angle X-ray scattering measurements.

The main parameters that were derived from the study here are the crystal thickness parameter (T) and the shape parameter η. The variation of these

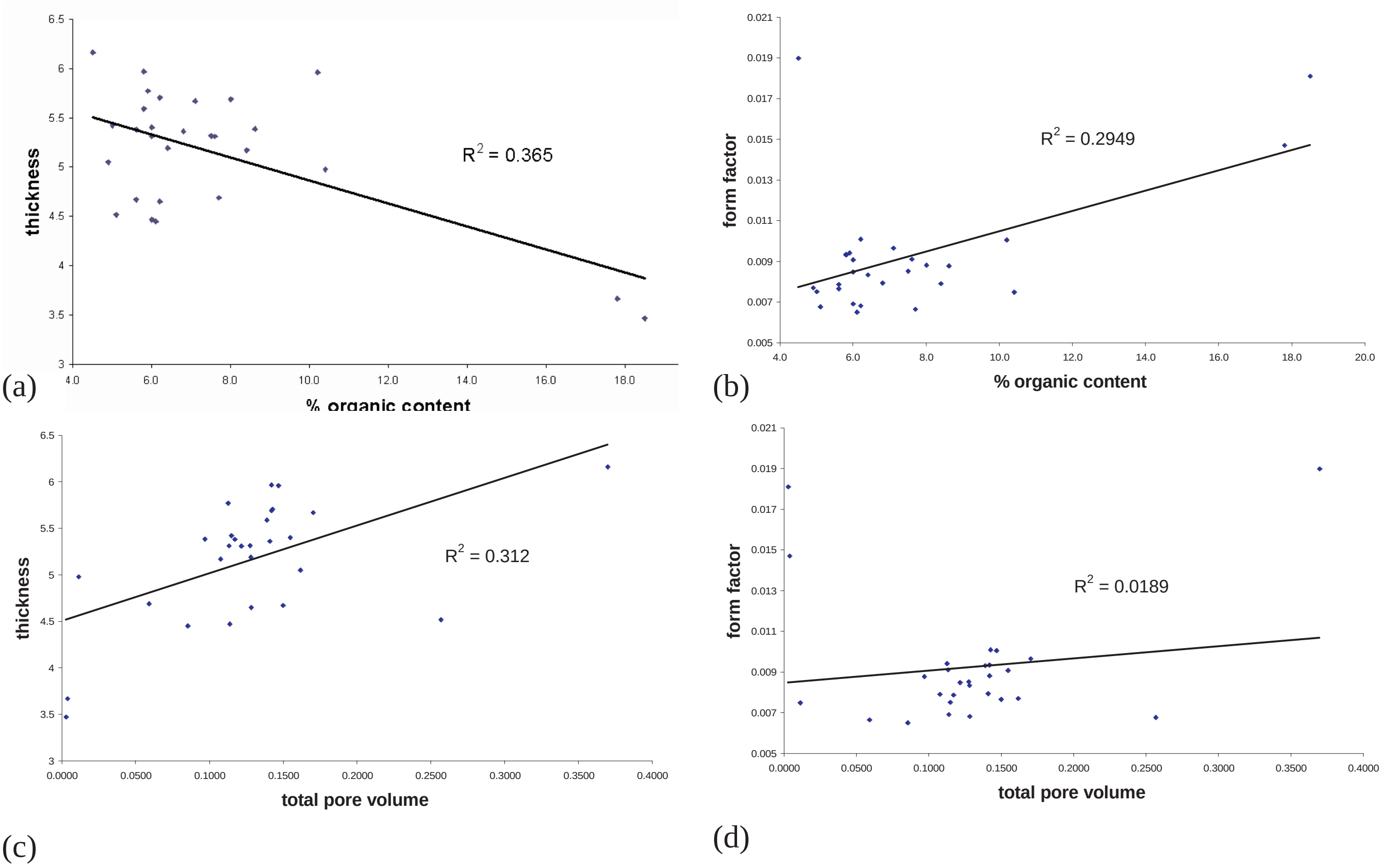

Figure 3: Scatter plot of the thickness parameter T and shape parameter η with allied measurements made on the archaeological sample. Two parameters of interest are the organic content and porosity of archaeological bone. The plots show a line of best fit and a regression analysis value R^2 that is the square of the correlation coefficient. The four scatter plots correspond to:

(a) the measured organic content against thickness parameter T;
(b) the measured organic content against form factor η
(c) the total pore volume against thickness parameter T and
(d) the total pore volume against form factor η

The plots contain a number of outlying points. These correspond to the most deteriorated bone which have a negligible organic content and large pore volume. At the other extreme, well preserved bones tend to have a high organic content and low porosity value.

parameters can be assessed between samples using data obtained on a conventional SAXS camera, and can be assessed within an individual sample by analysis of scans made at many points in a sample using microfocus SAXS.

Results

Crystal habit and thickness values from bulk measurements. The bulk measurements of crystallite thickness were derived from the data collected at the Daresbury synchrotron. Here the beam size is 4 orders of magnitude larger than the microfocus line and therefore provides an average of crystallite parameters over a large number of crystallites. It is important that such 'bulk' measurements are made since they are more representative of the size of samples used by archaeologists to obtain measurements of a number of other parameters such as porosity, total organic content, FTIR signal and histological preservation index. In this study, the major parameters that can be obtained as mean values with standard deviations are the crystal thickness parameter T and the shape function or η parameter.

In comparison to measurements from 10 control modern bones, the average thickness (T) of mineral in archaeological bone (516 nm) is larger than the mean value of control bone (349 nm). The spread of the values given by the coefficient of variation (125 % for archaeological and 120 % for control modern bone) also reveals that a wide range of crystal sizes can be attained by mineral remodelling over time.

The shape parameter is also a quantifiable variable

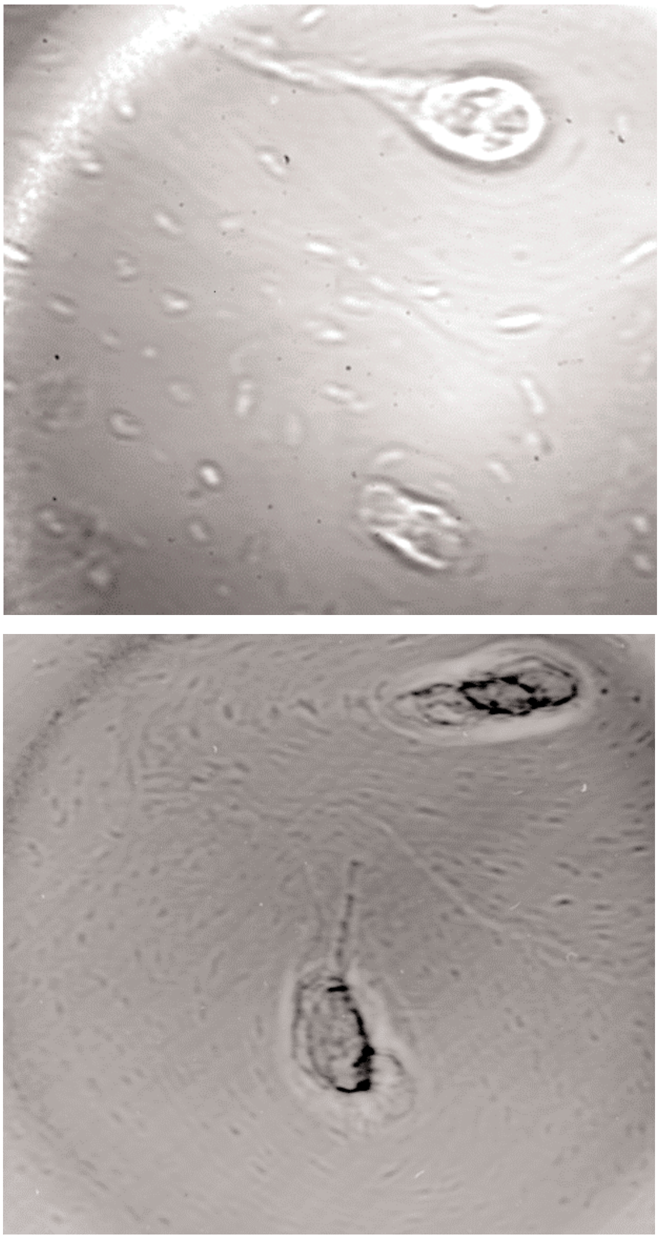

Figure 4: X-ray transmission micrographs of archaeological samples used for microfocus studies: These were obtained by using the unfocused X-ray beam from the ID22 synchrotron beamline at the ESRF, Grenoble. These examples show where scans were performed, as well as the direction of the scan. Each scan is 200 μm in length and 21 measurements were made at equal intervals on each line. The length of a scan also serves as a scale bar. The top image shows a region of cortical bone from a bovine femur and the bottom image is from cortical bone of an archaeological human femur. Both bones show features such as Haversian canals (large ovoids) and osteon lacunae (small ovoids). The deterioration in the archaeological bone is exemplified by the darker regions around the Haversian canal.

that shows the deviation of the scattering profile from the ideal Lorenzian profile. The archaeological bone samples showed a mean shape parameter of 0.009, which suggests that the average shape of the 30 samples is typical of a polydisperse crystal habit. This is not significantly different (according to Student's t-test at the 0.05 significance level) from the shape profile of modern bones (mean $\eta = 0.011$), which typically give a plate-like crystal habit, although the coefficient of variation is also far greater in the case of archaeological bone (33.3 % versus 90 % for modern bone).

Although it is difficult to make any presumption about the case history of an archaeological bone *post mortem*, it is possible to take representative samples of archaeological bone and to make comparisons of crystal thickness and form factor with other measured parameters. We have chosen to use the total organic content and total pore volume, parameters that may be expected to have a correlation with the bone crystallite thickness. The level of organic material in the bone reflects the collagen content; it could be expected that loss of collagen from archaeological bone removes restrictions on the crystallite shape and size. Furthermore, increased bone porosity may be expected to allow the formation of larger crystallites.

The scatter patterns of these parameters with crystallite size and form factor are shown in Figure 3(A-D). The plots show that there is a moderate correlation between these parameters and crystallite thickness and they allow us to suggest that the effects of porosity and organic content that are on a nm to μm scale reflect the remodelling of crystallites that are at the nanostructural level. The crystal shape parameter shows only a weak correlation with total organic content and no correlation at all with total pore volume, a measure of the porosity of the bone as indicated by nitrogen adsorption. This is probably a consequence of the large variability in η values for the archaeological bones.

Results from microfocus X-ray scattering studies on Archaeological bones. From the results described above, it can be seen that the variability in crystallite shape and thickness between archaeological bone samples is significant. The processes that remodel archaeological bone are thought in part to affect small regions of bone structure and therefore archaeological bone will contain a number of different crystallite textures over relatively small length scales. X-ray microdiffraction of small regions of bone were used to reveal these textural changes. An analysis of a representative microfocus scan is used here to show the capability of the technique.

Images of a thin section of the archaeological and modern bones used in this study are shown in Figure 4. These were obtained on a high resolution X-ray camera from the transmitted X-ray beam without the microfocus optical elements in place. In both cases the histological features such as the Haversian canal, lacunae and osteons can be seen in cross-section.

The variability of the crystallite habit in the bone samples at various points in each scan line (Figure 4) can be assessed best by comparing the normalised form factor function G(x) for each point in the scan and also by quantifying these parameters by computing η, the shape parameter. This parameter increases with the deviation of scatter from the idealised Lorentzian profile. In this study, polydisperse crystal sizes have low values for η (typically below 0.008), plates have higher values (typically $0.008 < \eta < 0.012$) and needles have values for η typically above 0.012 (corresponding to values derived from Fratzl et al, 1996a), although there is no sharp division between the different shapes.

The G(x) functions, thickness parameter and shape parameter for an archaeological bone sample (Figures 5(a) and 5(b)) are compared to those of a control sample (Figures 5(c) and 5(d)), which corresponds to a typical modern bone. It should be noted that the G(x) functions for all points in the control scan (Figure 5(c)) overlay with very little deviation, and show a very consistent needle-like morphology, which is typical for most modern cortical bones. For the scan in the archaeological bone sample, Figures 5(a) and 5(b) clearly correspond to a local region of bone remodelling, which shows the development of regions of microfocal destruction. This leads to the more variable G(x) functions displayed in Figure 5(a), which indicate a modulation in crystal habit. Examination of the shape parameter as a function of position in the scan (Figure 5(b)), shows that values of η decrease at a specific location between points 10 and 19 of the scan where the nature of the crystallite shape becomes more plate-like. The mineralised bone that surrounds the region of microfocal destruction was judged to be relatively unaltered from a histological perspective and the crystal habit remained as needle type structures.

As shown in Figures 5(b) and (d), the thickness parameter T was rarely larger than 4 nm for either the archaeological or the control bone scans. Changes in crystal thickness were exhibited on two length scales. First, local oscillations of ~ 0.1 nm in the thickness between consecutive points often occur, corresponding closely to the position of osteons in the sample along the scan. Secondly, undulations of up to 0.5 nm in crystal thickness that occur over a 30-50 μm range. These often correspond to regions of microfocal destruction involving local variation in the shape parameter. This is observed for the archaeological bone scan (Figure 5(d)). As depicted in Figures 5(b) and (d), the variation in the thickness parameter is, in general, significantly less than that of the shape parameter η. For both the archaeological and control bones, the shape parameter and T values along the scans are highly anti-correlated (with correlation coefficients of -0.92 and -0.89, respectively). This indicates a relationship between crystal shape changes and thickness that could provide a basis for remodelling of archaeological bone.

Discussion

Previous studies of crystal habit in bone have shown particular bone classes, such as cortical, lamellar and trabecular bone, to contain what is essentially a consistent crystal morphology; typically needles or plates with relatively little variation over a mm length scale (Fratzl et al,1996b). X-ray microfocal scattering has the capability of distinguishing the level at which textural variation occurs. This study has demonstrated that local regions of microfocal attack can be identified and the variation in crystal habit statistically analysed using microfocus X-ray technology.

The X-ray microfocus scattering experiments outlined here show the potential for using this technique to map the texture of bone in health, disease, forensic and archaeological contexts.

The ability to extract important structural information at the μm level has shown that local variation within bone texture can be observed and also that data can be represented in a quantified manner. Statistically this clearly has advantages over more subjective microscopical techniques such as scanning and transmission electron microscopy. The observation that the crystal thickness appears to be limited in the samples studied supports the earlier hypothesis of Collins *et al* (1995) that within archaeological bone, regions unaffected by microbial reworking contain essentially intact collagen. The results suggest that the persistence of collagen in bone may regulate the ability of the sample to remodel its mineral *post mortem*, and that the protein

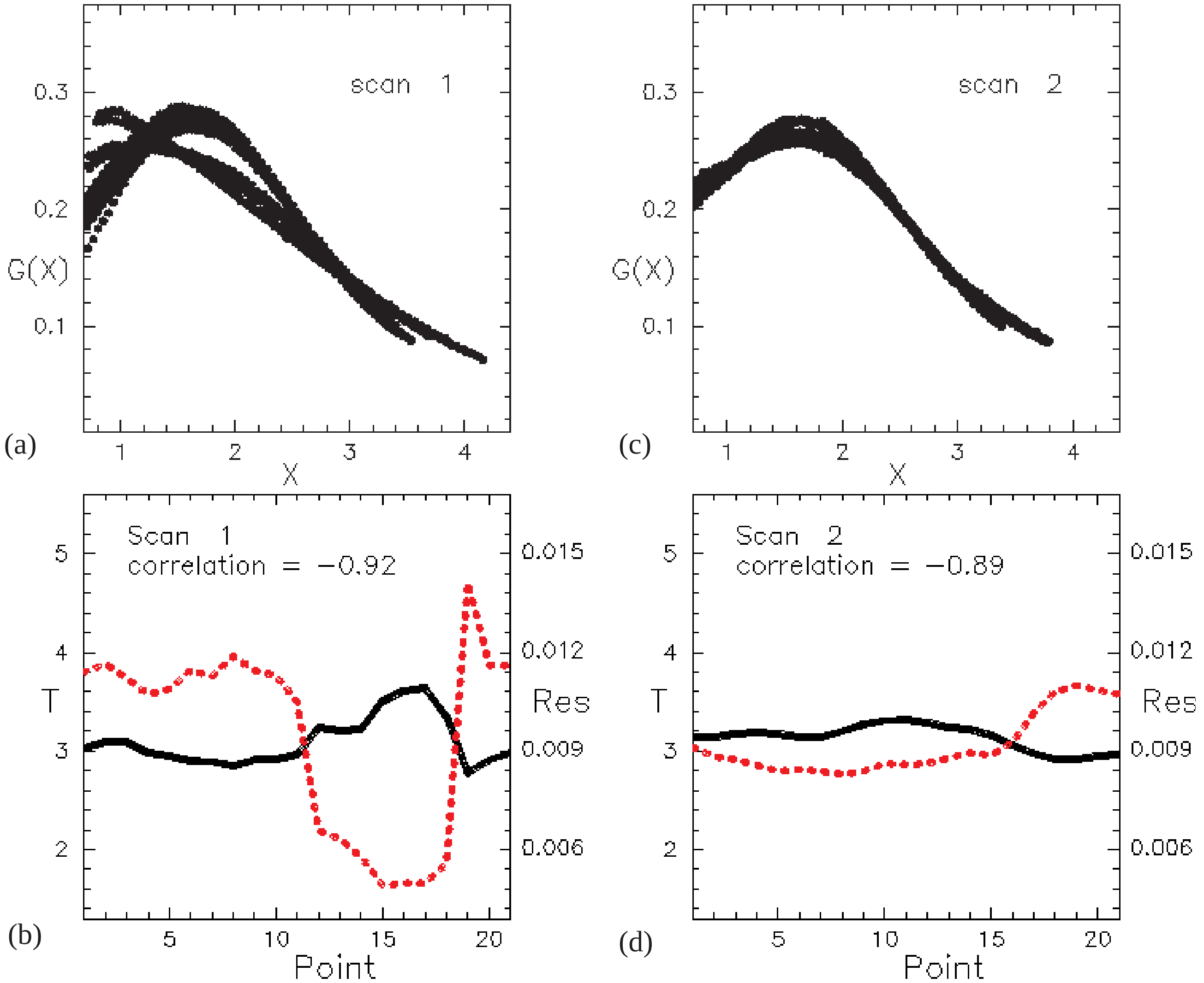

Figure 5: Plots of the crystal form factor G(x) for the scan lines shown in Figure 4 and of the variation of the thickness of the crystallites (T) in comparison with the parameter η The parameter η shows the deviation of the crystal habit from a Lorentzian distribution as determined by methods described in the text. The variation of the crystal thickness (continuous line) and habit (η dotted line) is shown for a typical control sample of modern human bone and compared to a scan that has been made in regions of an archaeological bone sample.

part of the extracellular matrix is an essential modulator of crystal habit.

The applicability of X-ray scattering studies in general to the field of archaeological bone analysis will allow the deterioration state of bones to be determined in a non-destructive manner. The identical sample can, therefore, also be used for biochemical analysis. Alterations in the crystal habit can be examined in comparison to other effects that are noted in archaeological bone, such as increase in porosity with deterioration (Hedges and Millard, 1995). Bone is a valuable archaeological indicator and significant progress has been made recently in the extraction of DNA from archaeological bone samples. The variability of the amounts and quality of DNA that can be extracted may relate to the alterations of the bone microstructure. Microfocus X-ray scattering is therefore an excellent tool that may be capable of determining the physical basis for the persistence of bone and its macromolecular contents.

Acknowledgements

We would like to thank all staff at the CCLRC Daresbury synchrotron and ESRF, Grenoble for help in data collection, especially A. Hammersley, A. Snigirev and I. Snigireva. This work was funded by the NERC grant GR 8/5019.

References

[1] Bell, L.S., Skinner, M.F. & Jones, S.J. (1996) The speed of post mortem change to the human skeleton and its taphonomic significance. *Forensic Science International*, 82, 129-140.
[2] Collins, M.J., Riley, M.S., Child, A.M. & Turner-Walker, G. (1995) A basic mathematical model for the chemical degradation of ancient collagen. *J. Arch.*

Sci. 22, 175-183.

[3] Fratzl, P, Fratzl-Zelman, N., Klaushofer, K., Vogl, G. & Koller, K. (1991) Nucleation and growth of mineral crystals in bone studied by small-angle X-ray scattering. *Calcif. Tissue Int*. 48, 407-413.

[4] Fratzl, P., Roschger, P., Eschberger, J., Abendroth, B. & Klaushofer, K. (1994) Abnormal bone mineralization after fluoride treatment in osteoporosis: A small-angle x-ray scattering study. *J. Bone Miner. Res*. 9, 1541-1549.

[5] Fratzl, P., Schreibe,r S. & Klaushofer, K. (1996a) Bone mineralisation as studied by small-angle scattering. *Connective tissue research* 34, 247-254.

[6] Fratzl, P., Schreiber, S. & Boyde, A. (1996b) Characterization of bone mineral crystals in horse radius by small-angle X-ray scattering. *Calcif. Tissue Int*. 58, 341-346.

[7] Hackett, C.J. (1981) Microscopical focal destruction (tunnels) in exhumed human bones. *Medicine, Science and the Law*, 21:243-264.

[8] Hedges, R.E.M. & Millard, A.R. (1995) Bones and groundwater: towards the modelling of diagenetic processes. J. *Archaeological Science* 22 155-165.

[9] Lewis, R. (1994) Multiwire Gas Proportional Counters: Decrepit Antiques or Classic Performers? *J. Synchrotron Rad*. 1, 43-53

[10] Nielsen-Marsh, C.M., Gernaey, A.M., Turner-Walker, G., Hedges, R.E.M., Pike, A.W.G. & Collins, M. (2000) The chemical degradation of bone in Human Osteology: In 'Archaeology and Forensic Science' (eds Cox, M. and Mays, S.), *Greenwich Medical Media*, London, pp 439-454.

[11] Snigirev, A. & Snigireva, I. (1995) On the possibility of X-ray phase contrast microimaging by coherent high-energy synchrotron radiation. *Rev. Sci. Instrum.* 66, 5486-5490.

[12] Snigirev, A., Kohn, V., Snigireva, I. & Aristova, E. (1996) A compound reflective lens for focussing high energy X-rays. *Nature* 384, 49-51.

[13] Towns-Andrews, E., Berry, A., Bordas, J., Mant, G., Murray, K., Roberts, K., Sumner, I., Worgan, J.S. & Lewis, R. (1989) Time-resolved X-ray diffraction station: X-ray optics, detectors, and data acquisition. *Rev. Sci. Instrum*. 60, 2346-2349.

[14] Ziv, V. & Weiner, S. (1993) Bone crystal sizes: a comparison of transmission electron microscopic and X-ray line-width broadening techniques. *Conn. Tissue Res*. 30, 1-14.

Lessons for Today and Tomorrow from Yesterday - the Structure of Alginic Acid

Struther Arnott#,*, Wen Bian*, R. Chandrasekaran*, Bridget Ryan Manis*

The Institute for Cancer Research, Chester Beatty Laboratories, 237 Fulham Road, London SW3 6JB, England.

* Whistler Center for Carbohydrate Research, Purdue University, West Lafayette, Indiana 47907, USA.

We describe a re-determination by X-ray diffraction analysis of the structures of polymannuronic and polyguluronic acids in oriented, polycrystalline fibers and thereby provide a more accurate visualization of the role of divalent cations in alginate gels.

The Context of this Study.

Fibrous substances are important in many biological contexts and their successful exploitation by *Homo sapiens* for food and textured materials had a millenia-long history before it was even thinkable to rationalize their valuable properties in molecular terms. Profitable technologies can evolve without accurate information about molecular or higher structure and even despite inaccurate information: there is no accurate fibre structure in the literature for, say, crystalline rubber! This is not to say that technologies cannot profit from detailed molecular structures in those cases where there is indeed a close and manipulatable relationship between their functional properties and their atomic-level structures. Our predicament is that revealing structures at this level gets to be tantalizingly difficult in many fibrous biological systems where diffraction data are sparse below 2.5 Å. Credible atomic detail therefore comes at a cost more than most fibre diffractionists have been prepared to invest. Poor-mouthing their own good data becomes a routine justification for failure to make this investment and to go on to fully complete and authenticate provisional structures. The published record thereby accumulates too many incomplete and flawed structures and consolidates a needlessly baleful impression of the power of fibre diffraction analysis and the worth of its products. We will use the case of a gel-forming polysaccharide system important in the food and pharmaceutical industries to illustrate the potentially high information content of conventional, film-recorded, fibre diffraction patterns subjected to linked-atom least-squares analysis [1,2] guided by ancillary Fourier syntheses of electron density. In such analyses the polymer framework can, with care, be defined with confidence and precision. Ancillary cations and water molecules justified by the diffraction data then can be added and function rationalised in atomic terms.

The Nature of Alginic Acid.

Alginic acid essentially has a very simple primary structure but its useful properties depend not only on its secondary structure(s) but also on the manner with which small components such as water and ions interact with these polymeric structures. Its biological synthesis occurs via poly-1,4-β-D-mannuropyranosylic acid (M). This polymonosaccharide, mannuronan, then undergoes post-polymeric modification by a C5-epimerase which introduces blocks of poly-1,4-α-L-guluropyranosylic acid (G or guluronan) and regions of mixed M and G composition between the M and G blocks. Alginates with higher content of G show a greater affinity for Ca^{++} ions and form stronger, harder gels. Spinning oriented fibres from such gels has not been very successful but they have been shown to contain the same molecular conformations as the acid forms which can be obtained in uniaxially oriented, polycrystalline form [3,4]. *Faute de mieux* we have had to rely on the data obtained from these pioneering experiments whose good-quality fibre patterns have not been bettered. It is a more common experience in fibre diffraction analyses than in macromolecular crystallography that one has to rely on a unique example of successful art in producing felicitously well-ordered specimens and in this case using the original data has the additional merit of highlighting what could and should have been done at the time of their collection when the same analytical tools that we have used were all available [1].

The X-ray Data and Structural Variables.

We have reviewed the structures of both mannuronan and guluronan. Each in the hands of the original skilled investigators provided what we would regard as rather good fibre diffraction patterns. The numbers of reflections are not large - 44 in the case

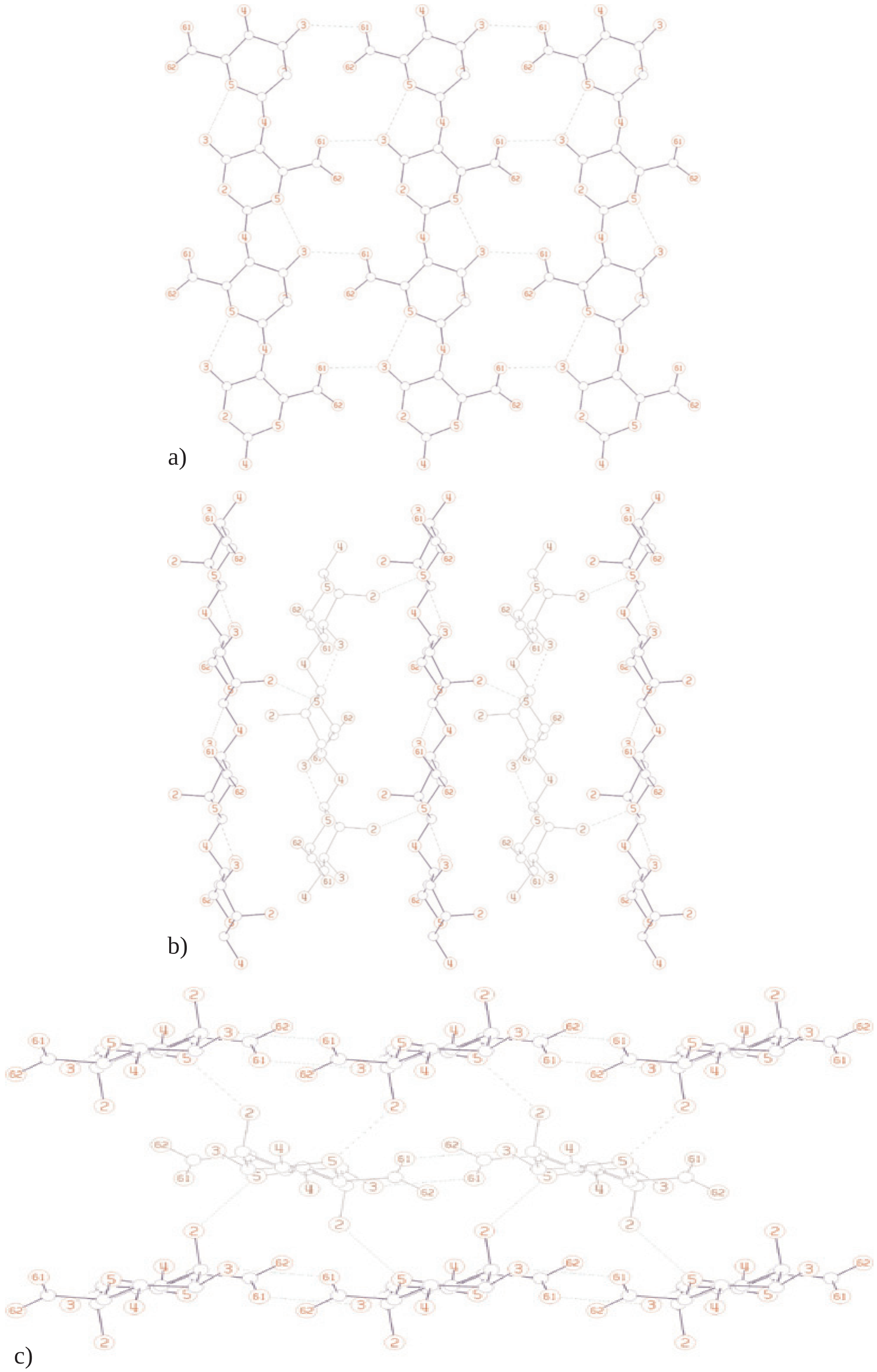

Figure 1: Various views of the crystal structure of mannuronan: (a) the **bc** face of four unit cells, **c** is vertical and the length of the disaccharide is **c** = 10.4 Å, the polysaccharide chains are flat ribbons with O3···O5 H-bonds stabilising the glycosidic linkages, **b** is horizontal and the molecular ribbons are spaced at intervals **b** = 7.6 Å and linked by O3···O61 hydrogen bonds; (b) the **b** axis projection, **c** is again vertical and the horizontal **a** spacing (between parallel molecules) is **a** = 8.6 Å which are linked indirectly by the hydrogen bonds between anti-parallel chains; (c) the **c** axis projection with **a** vertical again showing the inter-sheet O2···O5 H-bonding of the antiparallel sheets of parallel molecules with intra-sheet O3···O61 H-bonding.

of mannuronan and 48 in the case of guluronan - but the molecular structures are correspondingly simple: both are 2-fold helices of monosaccharide residues. With their c spacings determining the pitch, the backbone conformations are fixed except for any restrained variation that was allowed to the initially standard bond angles and ring conformations. The only challenging molecular variable to be determined is the carboxyl conformation and even this can be reduced to a few narrow ranges if there are internal H-bondings such as are illustrated in Figs. 1a and 2a. In both structures two antiparallel 2-fold helices pass through each unit cell in such a fashion as to result in $P2_12_12_1$ orthorhombic symmetry. There are therefore only two variable polymer packing parameters, a molecular translation along **c** and an orientation about **c**. This means that in a linked-atom system with fixed standard bond lengths and angles there are only three degrees of structural freedom to be determined with 45 or so intensity data available in each case. Even when final refinements might involve ring bond and conformation angles subject to elastic restraints on their movements and to ring-closure constraints, the data parameter ratio would remain high, (45+12)/(3+12-6) ~ 6. Even the addition of two water molecules, each with three coordinates, but each also with four hydrogen-bonding restraints, would not seriously reduce the satisfactory ratio, (45+12+8)/(3+12-6+6) ~ 4. Nor should it be forgotten that in these compact unit cells the close contacts between neighbouring non-bonded atoms provide around 70 more quasi-data in the least-squares minimization. Altogether it should be impossible with reasonable care not to arrive at an accurate and precise atomic resolution structure.

The Structures of Mannuronan and Guluronan.

We should define at this point what these two structures are now seen to be. Many important details have emerged from our new analysis - whose details in terms of atomic coordinates, lists of structure factors, etc. are available separately [5] - but the gross framework emerged from the earlier investigation by others and our purpose is not to minimize their contribution but to discuss the difficulties encountered in reaching a credible final conclusion.

The biosynthetic relationship of mannuronan and guluronan and their formally similar crystal structures belie the very different secondary and tertiary structures they assume. The mannuronan chains are extended maximally in the **c** direction just like cellulose with a 10.4 Å repeat (Fig. 1a). Intramolecular O3···O5 H-bonds buttress the resulting molecular ribbons which form sheets when they are laid parallel to one another along the **b** direction with a 7.6 Å spacing and stitched together by intermolecular O61···O3 H-bonds. When these sheets are stacked anti-parallel to one another along **a** (Fig. 1b), the repeat distance is 8.6 Å and the interleaved sheets in the stacks are glued together by O2·O5 H-bonds.

The carboxyl O61 hydrogen atoms have a crucial role in this compact acid structure (Fig. 1c) that has no space for guest molecules even as small as water and therefore does not survive salt formation.

The C5 epimerization which changes mannuronan to guluronan results also in the dramatic change in the pyranose ring conformations which are evident in all views of the G structure (Figs. 2a,b,c). The molecular shape is no longer a ribbon and the **c**-axis repeat is reduced from 10.4 to 8.7 Å and a different H-bond, O2···O61, buttresses the glycosidic linkage (Fig. 2a). There is no longer direct H-bonding between polysaccharide chains. Instead a chain of water molecules provides O2···W···O61 bridges between guluronan molecules along the **a** direction, using every other water molecule in the chain. The alternating set of water molecules in the chain provides O3···W···O5 bridges between the polysaccharide chains that are lined up parallel to one another along the **b** direction (Fig. 2b). The images given by this somewhat artificial deconstruction of the overall three-dimensional structure needs to be integrated by the **c**-axis projection of the lattice (Fig. 2c) which shows a more comprehensive picture of parallel chains at the corners of two contiguous unit cells and the central anti-parallel chains completing the orthorhombic array. The water molecules fill up the channels that are diamond-shaped in cross section and run along the **c** direction. Although these water molecules are connected vertically to one another, laterally each also provides a bridge between two parallel chains across the diagonals of the diamond, but none by itself is connected to more than two chains. The picture changes dramatically when water is replaced by Ca^{++} in one water site (Fig. 3). Then the guest molecule becomes the connector of all four guluronan chains bordering the channel: the O5···X···O3 connection acquires an intersecting

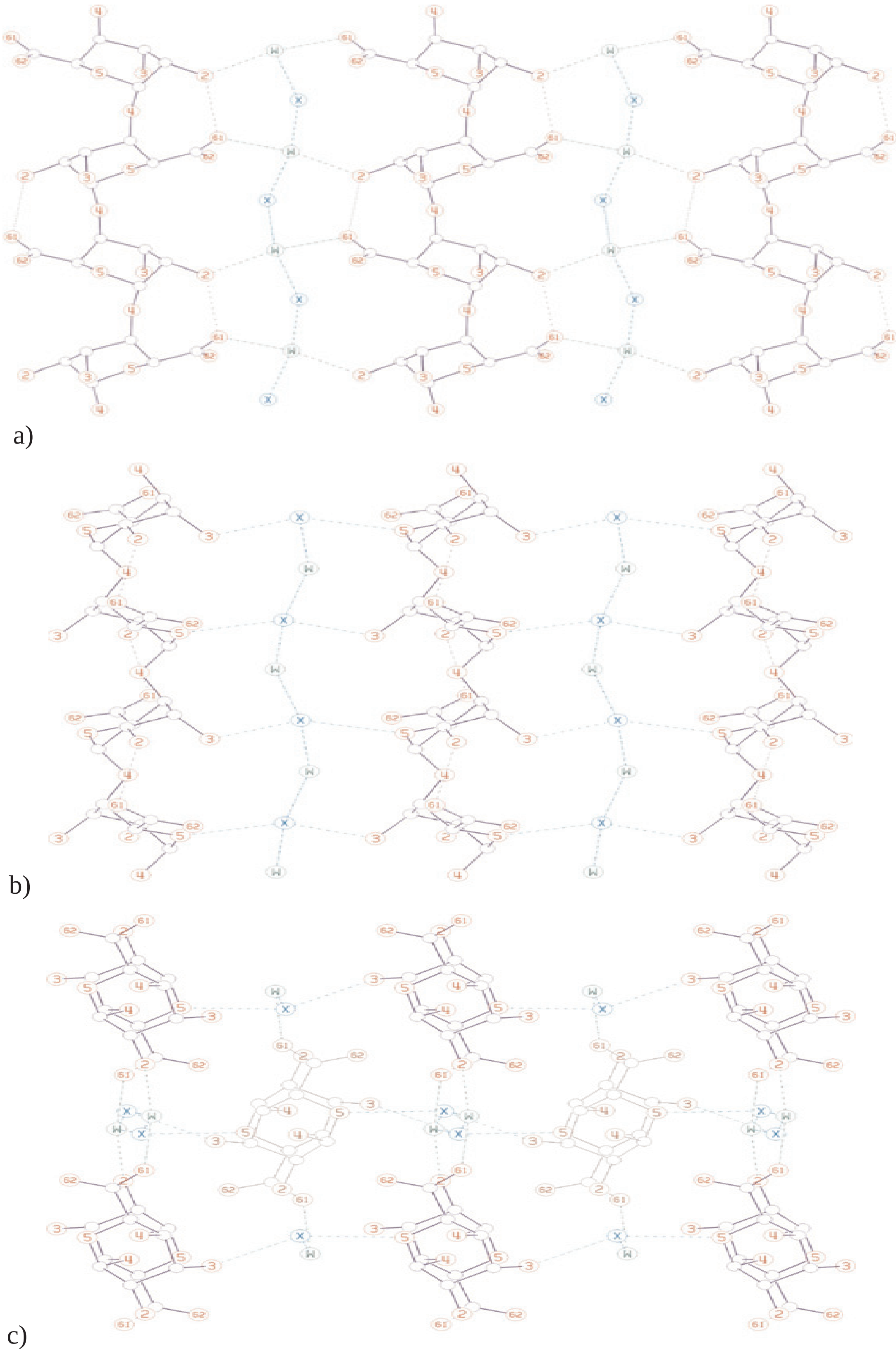

Figure 2: Various views of the crystal structure of hydrated guluronan: (a) the **ac** face of four unit cells, **c** is vertical and the length of the disaccharide repeat is much reduced relative to mannuronan (**c** = 8.7 Å), the intra-chain H-bonds are now O2···O61, the **a** spacing is long (**a** = 10.7 Å) and accommodates a chain of water molecules between the parallel guluronan chains, linking them by O2···W···O61 H-bonds through the set of 21 symmetry related water molecules W; (b) the **bc** face with **c** vertical showing that these parallel guluronan chains are linked by O3···X···O5 H-bonds using the second set of symmetry-related water molecules X, the chain-to-chain spacing **b** = 8.6 Å; (c) the **c** axis projection of two complete unit cells with **a** vertical, the central diamond shows all the O···water···O bridges that glue the matrix together - the (green) O61···W···O2 bridges vertically and the (blue) O3···X···O5 bridges horizontally.

connection O2···X ···O61 more or less perpendicular to it and, like it, perpendicular also to the vertical string of water molecules. It is not surprising that the resulting gel is strong and hard. Nor is it surprising that Sr^{++} ions promote even tougher gels since the $O\cdots X^{++}$ distances in the polysaccharide matrix would be an even better match with a divalent cation of radius a few tenths of an Å greater than Ca^{++}. All in all the picture of the cation-dependent alginate structure that emerges from this analysis is profoundly different from the egg-box cartoon that was developed by Rees *et al*. [6] in the wake of the earlier imperfect structure.

The Sequence of the X-ray Refinements.

It had not been our intention to embark on a major recapitulation of the structure determination of these two polysaccharide systems. We had in mind only to have on file up-to-date versions of the structures with confirmed stereochemistry and added detail such as the hydrogen atoms omitted in the earlier study. We also wanted to recover an unbiased set of X-ray data with reflections too close to separate grouped together as one composite datum rather than carved up in the same ratio as some calculated model set as had been done in the provisional work. We wanted also to make sure that all reflections perceived to be absent within the field of observed reflections were indeed calculated to be below the observational threshold for any modified structures we might construct. We planned a routine final refinement to reconcile our modestly modified version of the original structures with these equally modestly modified data but began with an attempt to reproduce the original final structures and their structure factors. Unfortunately we discovered that we could in neither case reproduce these (and their R-factors) without improperly doubling the values of our calculated $h0l$ and $0kI$ reflections. We had thereby uncovered, not for the first time, a not uncommon error in structure analyses involving uniaxially oriented polycrystalline fibres [7]. It can arise from the facile cliche that all diffraction data from fibres are 'cylindrically averaged' versions of the Fourier transform of a molecule or a molecular assembly. This is just not the case for oriented and polycrystalline specimens where one is dealing with the analogue of a rotation diagram of a single crystal where different zones of reflections may have different multiplicities. In the orthorhombic case there is systematic overlap of $0,k,l$ and $0,-k,l$, -- only two reflections assumed to have equal amplitudes in this instance -- but for h,k,l there are four reflexions that overlap systematically and also can be assumed to have equal amplitudes: $-h,k,l$ and $h,-k,l$ and $-h,-k,l$ and h,k,l. The important thing to do is to compare observed and calculated quantities that correspond with one another!

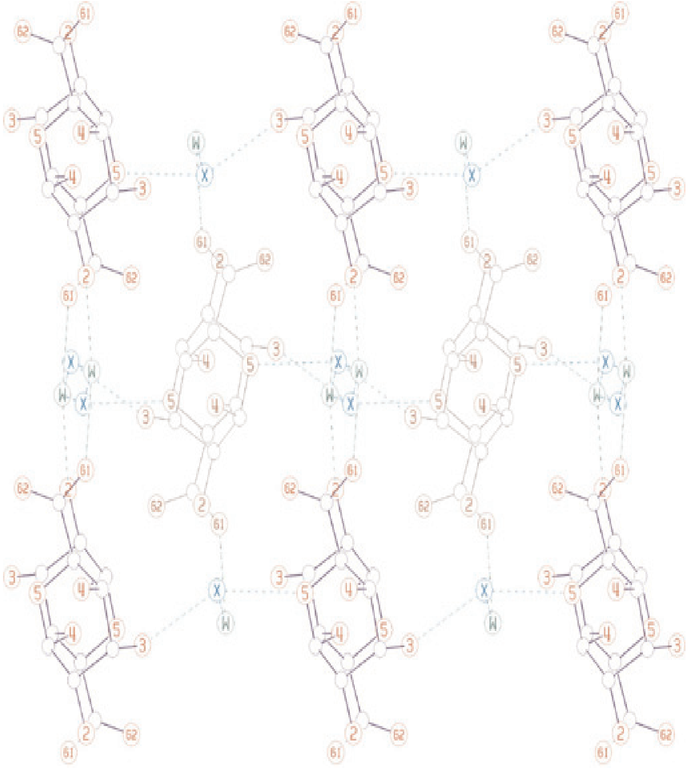

Figure 3: When X is not water but Ca^{++} the resulting octahedral coordination allows this component to make bridges vertically between O2 and O61 as well as horizontally between O3 and O5. Each water coordinated to Ca^{++} continues to participate in the O2···W···O61 bridges shown in Figs. 2a,c but not shown in this illustration.

Correcting the M and G data sets for these fundamental errors immediately raised their already non-descript 'final' R values, respectively 0.23 and 0.25, to provocatively higher values, 0.31 and 0.40. We therefore had to go on with new refinements using the corrected data set but starting with the final parameters provided by the previous analyses. In the discussion which follows, we will continue to quote the conventional R factor as a more familiar surrogate for the quantities we in fact used to monitor the course of our refinements. The quantity minimized by the LALS process is:

$$\Omega = \Sigma\, \omega\, \Delta F^2 + \Sigma\, \varepsilon\, \Delta\Theta^2 + \Sigma\, \kappa\, \Delta D^2 + \Sigma\, \lambda\, G$$

and the statistical tests [8] of the significance of improvements achieved during our structure analyses were made using its values and/or more conservatively its first component , $\Sigma\omega\Delta F^2$, which is the usual sum of the weighted, squared differences between model and experimental structure amplitudes. The second sum of weighted, squared difference terms involves structure parameters such as bond-angles or ring conformation-angles that have standard values that are explicitly varied during an analysis while tied elastically to the standard values. The third term involves another set of restrained variables (such as hydrogen bond lengths) that may vary elastically from pre-set standard values and are functions of the parameters explicitly varied during the least-squares refinements. The fourth term involves Lagrange Multipliers (λ) and the constraint functions (G) that have all to be made zero by the end of the refinement. Commonly these (exact and not elastic) relationships are used to ensure ring closure, residue connectivity and the like.

For the M structure, refinement of a scale and an overall isotropic temperature factor as well as the packing variables and the carboxyl conformation brought R down from 0.31 to 0.21 but changing the domain of the carboxyl conformation so that its refined value ended up at 10º rather than 114º reduced R still further to 0.16. At this stage difference electron density maps were used to confirm that there were no guest molecules and the analysis was concluded by a refinement that permitted restrained variation of the previously fixed ring conformations and bond angles. This resulted in reducing R falling to 0.12.

With the G structure, the same sequence of refinements starting with R at 0.40 brought improvement only to 0.37 before reduction could be continued to 0.27 by moving the carboxyl conformation to an alternative domain in this structure also. At this stage, by contrast to the M structure, there was clear evidence from the electron density syntheses of further scattering material centred half way along **a** and about 3 Å from two carboxyl groups. A single water molecule placed near this position resulted in $R = 0.25$, but a pair of water molecules brought R down to 0.20. A concluding refinement with relaxed ring conformations ended with $R = 0.17$.

Technical Lessons.

Data. The obligation of diffractionists to publish their data at the same time as the structure(s) derived from them is now well established among crystallographers. The same obligation must be expected of fiber diffractionists. We were fortunate in this analysis that our predecessors had been so scrupulous as to do just this at a time when it was much less common. We were fortunate also that the error in their data was so simple and straightforward to correct. For other diffraction studies where there has been elaborate manipulation of the fundamental experimental observations it may be desirable that these unprocessed data be freely available also. This has to be a serious option in fibre diffraction analyses where many procedures are pioneered in local laboratories but do not become part of some canon recognised by a large community as is the case with, say, protein crystallography.

R Factors. The original, flawed data sets with partially refined structures subjected to limited but unspecified elasticity gave R factors of 0.23 and 0.24 respectively for mannuronan and for guluronan (with its one added water molecule per sugar residue). The corrected data sets and the same gross polysaccharide structures refined with fixed bond lengths and angles and fixed sugar rings and no guest molecules gave R factors of 0.21 and 0.37 after refining a scale and a temperature factor, two packing parameters and the carboxyl conformations (in wrong domains). We can estimate that adding one or two water molecules to the guluronan structure would have reduced R to 0.34 or 0.28 but we know that in the end both mannuronan and guluronan ended up with these R factors nearly halved as a result, first, of changing the domains of the carboxyl conformations (a significant 30% reduction of the previous value) and, finally, restrained relaxation of the ring shapes - to anneal or equilibrate, so to speak, the completed structure - provided the final 15% improvement. This also was a significant improvement as determined - as always in our analyses - by a Hamilton test [8]. The final R values (0.12 and 0.17) confirm our original good impression of the efforts of the pioneering investigators. Because these values have been subjected to Hamilton Test monitoring, we believe they are not cosmetic and, indeed, the harmonious structures that have emerged as a result of our scrupulous step-wise processes are consistent with this conclusion. The historic data from good laboratories that provided these good indices are therefore deserving of considerable respect. Processing such data could be improved in simple non-controversial ways. There is evidence that the main systematic errors are due to background and baselines and that very significant improvements in the fit between observed data and their modelled equivalents can be achieved by intruding one or two global parameters to deal with overall background. Nevertheless those of us who deal mainly with biological or other solvated systems in the end will come up against a phenomenon observed, and commented upon [9], by macromolecular crystallographers: *R* factors, even in very favourable cases, are systematically higher for data of resolution > 5 Å than they are for higher resolution data even when substantial allowance has been made for solvent. In many fibre systems, where the data-to-parameter ratios are quite similar although the data are many fewer, a higher proportion of data come from the difficult range so that miniscule values of *R* will be denied to us no matter how sophisticated our data detectors become. In the context of this discussion it has not escaped our notice that the compact, unsolvated mannuronan structure has a rather lower *R* value than the hydrated guluronan structure even although its data-to-parameter ratio is somewhat greater than that of guluronan!

Least-Squares.

We have continued to exploit a modern version of the Linked-Atom Least-Squares technology and eschewed hybridizing it with algorithms that minimize free energy. Both approaches have their drawbacks. Our main concern is to perform a diffraction analysis augmented, minimally, with other information in order to overcome the somewhat limited resolving power of the diffraction data, and not to compensate either for their often small number (since we always restrict the number of allowed variables and their nature appropriately), nor yet for their quality (since it is evident from analyses such as the present ones that the data often are good enough to allow structures to be solved, with confidence and precision, to an accuracy that is within a few tenths of an Ångstrom in atomic positions). To some extent the additional restraint terms in W relate to the potential energy of the structure being determined but they have the advantage of having the right form to be integrated with a least-squares process not least because it can be arranged that in the end the relative weights of all the terms can be harmonized to ensure that all sub-sets have mean squared discrepancies of unity (i.e. $<\omega\Delta F^2> \sim <\varepsilon\Delta\Theta^2> \sim <\kappa\Delta D^2> \sim 1$). This is the condition for a successful least-squares minimisation from which meaningful measures of overall significance can be extracted as well as standard deviations for the values of variables [10].

Optimization.

Optimization has to be a way of life for fiber diffraction analysts. Solution of the phase problem by them most often is dependent on the formulation of initial models. If alternative models can be proposed, a choice between them should not be made on the basis of samples of each type but on the basis of the optimum representatives. A related but distinct problem is the occurrence of false minima where a best fit is obtained with all restraints and constraints satisfied but a better solution exists that can be accessed only by conducting the refinement from a different starting point. The analyses of mannuronan and guluronan each provided examples of this in the matter of their carboxyl conformations. These have two sterically viable domains about 90º apart (and a further two, 180º from each of these, which can be distinguished from the original two only when carboxyl can be distinguished from carboxylate). In both investigations, the earlier workers had the bad luck to opt for conformations in the wrong domain. This we believe was not a result of their incorrect sets of data since we achieved for mannuronan a very satisfactory $R = 0.21$ with the corrected data and a refined version of their inaccurate structure. Rather their mistake was to make a premature choice of the conformational domain of the major variable (the carboxyl), before there had been a concerted refinement of all the variables as would occur in a least-squares process. Then they compounded the initial mistake by not giving a further opportunity to the alternative conformation in a second refinement. Such parsimony is inappropriate in fibre diffraction studies: when alternatives exist, significant discrimination can be made only between optimum representatives of each possibility.

Acknowledgements.

This work was supported by the UK Leverhulme Trust and the Industrial Consortium of the Whistler Center for Carbohydrate Research.

References.

[1] Arnott, S. and Wonacott, A.J., *Polymer* (1966) 7, 157-166.
[2] Smith, P.J.C. and Arnott, S., Acta *Crystallogr*. (1978) A34, 3-11.
[3] Atkins, E.D.T., Nieduszinski, I.A., Mackie, W., Parker, K.D. and Smolko, E.E., *Biopolymers* (1973) 12, 1865-1878.
[4] Atkins, E.D.T., Nieduszinski, I.A., Mackie, W., Parker, K.D. and Smolko, E.E., *Biopolymers* (1973) 12, 1879-1887.
[5] Bian, W., Ph.D. Thesis, Purdue University (2001).
[6] Grant, G.T., Morris, E.R., Rees, D.A., Smith, P.J.C. and Thom, D., *FEBS Letters* (1973) 32, 195-198.
[7] Upstill, C., Atkins, E.D.T. and Attwool, P.T., *Int. J. Biol. Macromol.* (1986) 8, 275-288.
[8] Hamilton, W., *Acta Crystallogr.* (1965) 18, 502-510.
[9] Sheldrick, G.M. and Schneider, T.R., *Methods Enzymol.* (1997) 277, 319-343.
[10] Cruickshank, D.W.J., *International Tables for X-ray Crystallography* (1972) Vol. II, 84-98.

Applications of highly constrained molecular modelling scattering curve fits to biologically important proteins

Stephen J. Perkins

Dept of Biochemistry and Molecular Biology, Royal Free and University Medical School, Rowland Hill Street, London NW3 2PF, UK.

Full molecular structures can be extracted from solution scattering analyses of multidomain or oligomeric proteins if the scattering curve fits are constrained by known small structures for the subunits. All the different possible molecular structures are computed, using as constraints any known covalent connections or symmetry features between the subunits. Each model is assessed for steric overlap, radii of gyration, sedimentation coefficient and R-factor. Filtering leaves a small family of good fit models that corresponds to the molecular structure of interest. These structural analyses often provide new biological insights into function.

Introduction

Solution scattering is a diffraction technique used to study overall structures in solution. A sample is irradiated by a collimated, monochromated beam of X-rays or neutrons. The resulting two-dimensional circularly-symmetric diffraction pattern is recorded on a flat area detector system. Radial averaging leads to a one-dimensional scattering curve. Traditionally these curves leads to structural information at a resolution of about 2-4 nm from calculations of the radius of gyration R_G, the cross-sectional R_G (R_{XS}) and the distance distribution function, and the use of spherical harmonics or genetic algorithms provides an overall view of the macromolecule. This approach provides information on overall macromolecular dimensions and molecular weights from the intensity I(0) at zero scattering angle. In distinction to this traditional approach, the utility of solution scattering has been much improved by means of a novel strategy in which molecular structures are derived directly from the scattering curves. This method starts from known molecular structures for subunits within the macromolecule which are used as tight constraints of the scattering data (reviewed in [1-3]).

In this article, the comparison of a series of investigations [4-18] shows that these studies fall into four distinct types (Table 1). Our most recent studies are discussed to illustrate this approach [14,17].

Scattering modelling potentially provides useful results for a multidomain protein for which an overall structure is unknown, yet molecular structures are available for all the individual domains in it. Such large multidomain proteins are often not crystallisable for reason of interdomain flexibility or surface glycosylation, either of which hinders crystal growth. If crystals are obtained, it is possible that a flexible multidomain arrangement has become frozen into an artefactual snapshot of only one possible conformation. The use of scattering modelling will show what types of domain arrangements are compatible with the solution data. Scattering modelling is also useful in analysing the association of multiple subunits into oligomeric structures. If a biologically important oligomer cannot be crystallised, scattering modelling is a way to obtain a structure. In these applications, the use of known atomic structures as tight constraints to model scattering curves is highly complemented by the continuing growth of the Protein Data Bank, which currently possesses over 14,000 structures (March 2001), as this provides the raw material for these scattering analyses. Indeed the use of these constraints can raise the precision of the scattering models to as high as 0.5 nm.

Scattering modelling is applicable to both X-ray and neutron data. These exhibit very different but complementary properties. X-ray scattering using synchrotron radiation provides high quality curves that are minimally affected by instrumental geometry, as the incident fluxes are sufficiently high to permit the use of ideal pin-hole optics. X-rays visualise the macromolecule in a high positive solute-solvent contrast. More importantly, X-rays also visualise the macromolecule with a hydration shell surrounding it, and this significantly affects the modelling of the scattering curve. In distinction to this, neutron scattering is able to visualise macromolecules in positive and negative contrasts by the use of light and heavy water buffers. The range of scattering densities generated by varying this heavy water content is sufficiently wide to encompass the scattering densities of lipids, protein, carbohydrate and DNA/RNA. Hence, by neutron contrast variation, one component can be matched out by an appropriate choice of heavy water buffer (see below). Neutron scattering is also characterised by the absence of radiation damage effects sometimes encountered with X-ray synchrotron radiation, and also by the ease of determining molecular weights. It is also useful that to a good approximation the hydration shell is not visible in neutron scattering, and this simplifies the application of modelling strategies.

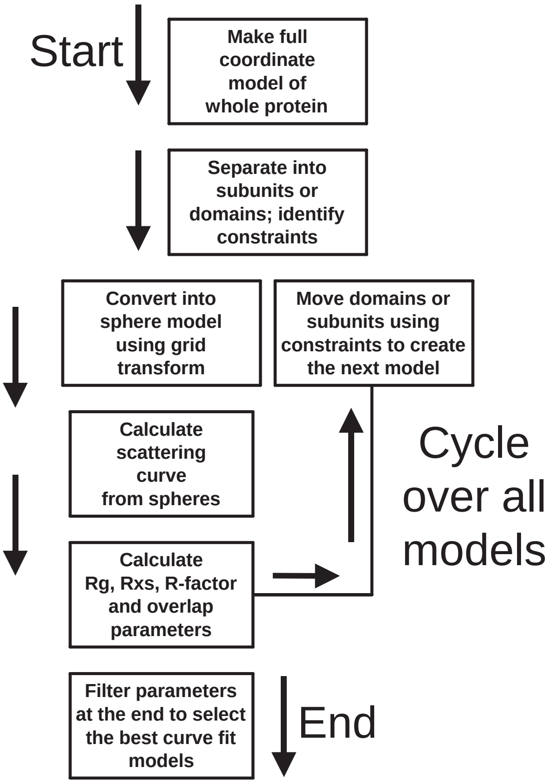

Figure 1: Flow chart of the automated modelling procedure that is used with appropriate modifications for the searches in Table 1.

Method for curve fits

The first stage in constrained scattering modelling is of course the experimental data acquisition itself. Our data have been obtained at the SRS Daresbury (X-rays), ISIS Rutherford-Appleton (neutrons) and the Institut Laue Langevin (neutrons) laboratories. Technical details are given in [3]. Analyses to obtain the RG and I(0) values from Guinier plots and distant distribution functions are completed in full before any modelling is initiated. The second stage is to identify the atomic structures that best represent the subunits of the full structure to be modelled, whether these be directly obtained from crystal or NMR structures, or indirectly by the application of homology (or "comparative") modelling. The third stage is to model the X-ray and neutron scattering curves I(Q) using small spheres of uniform density to represent the protein structure. Their total volume must be the same as that of the dry protein. Curves are calculated from Debye's Law adapted to small spheres [1,2]. These spheres have to be sufficiently small (about 0.6 nm) so that their form factor in the Debye equation is almost invariant in the Q scattering range used (Q = 4B sin 2 /8; 22 = scattering angle; 8 = wavelength).

The first of the four types of constrained scattering modelling listed in Table 1 are the calibration studies required to establish the technique [4-6]. For these, the crystal structures for ∀-chymotrypsin, ∃-trypsin, $\forall_1$-antitrypsin and pentameric serum amyloid P component (SAP) correspond to structures that are rigid and well-defined in solution and cover a wide molecular weight range of 23,200-127,000. These calibrations showed that the same single density approach under conditions of high solute-solvent contrasts worked well for both proteins and glycoproteins. Similar good fits were obtained with X-ray data in high positive contrasts and 100% heavy water neutron data in high negative contrasts, even with carbohydrate contents as high as 50% as found in carcinoembryonic antigen (CEA) [16]. The calibrations also showed that the hydration shell could be neglected in the neutron fits, but is required in the X-ray fits. This shell corresponds to a water monolayer surrounding the protein surface and is well-modelled by 0.3 g of water/g glycoprotein and an electrostricted volume of 0.0245 nm^3 per bound water molecule. Hydration shells are best modelled by adding spheres in a uniform layer to the surface of the model that is adjusted to reach the required hydrated volume [6]. The calibrations also show that no instrumental corrections for X-ray wavelength spread or beam divergence are required, although these are necessary for neutron cameras for reason of their larger physical dimensions. Neutron curve fits sometimes deteriorate at large Q. This is usually attributable to a small residual flat background that arises from incoherent scatter from protons in the sample.

The remaining three types of constrained modelling are automated conformational searches (Table 1). All three utilise the procedure summarised in Figure 1. Script files written for standard molecular graphics software packages generate a full range of models starting from atomic structures for the individual domains or subunits. Each one is readily converted into a sphere model by a grid transformation, from which the scattering curve is calculated for comparison with experimental data.

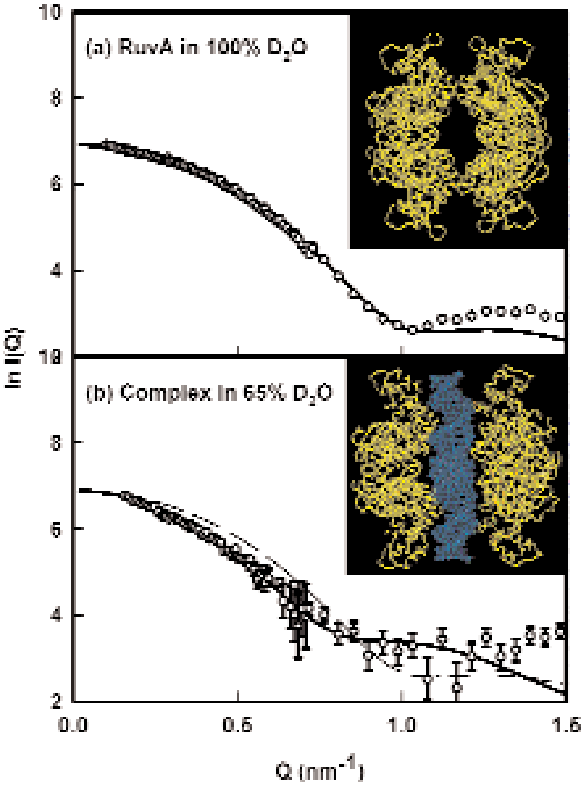

Figure 2: Neutron scattering curve fits for (a) the RuvA octamer (yellow: seen edge-on) and (b) its complex with the four-way Holliday junction DNA (blue). The curve fits in 100% D_2O for RuvA and in 65% D_2O for the complex (DNA invisible) are shown by the continuous lines. The dashed line in (b) corresponds to the unbound RuvA octamer and illustrates the large structural change on complex formation. Adapted from [14].

Up to four filters are used to identify the best models and to remove unsatisfactory models: (i) The systematic creation of models can result in physically unreasonable steric overlap between domains or subunits. This is readily detected by the grid transformation which will give too few spheres if significant overlap occurs, so there was a requirement for at least 95% of the expected total of spheres in a good model. (ii) The R_G and R_{XS} values were determined from the calculated curves in the same Q ranges used in the experimental Guinier fits of the experimental data. These are required to be within 5% of the experimental values in a good model. (iii) Sedimentation coefficients were calculated from the hydrated sphere models used for X-ray fits for comparison with the experimental values as an independent monitor of the search. (iv) The remaining good models were then assessed using a goodness-of-fit R-factor computed by analogy with the same term used by crystallographers. This rank ordering of all the good

Protein[1]	**Molecular weight**	**Scattering data**[2] **method**	**Search**	**Number of models tested**	**Constraints**	**Reference**
(a) Calibration Studies						
$\forall_1$-antitrypsin	51,500	X, N, S	Manual	1	Crystal structure	[4]
Trypsin/chymotrypsin (bovine)	23,200-25,600	X, N, S	Manual	4	4 crystal structures	[5]
SAP pentamer	127,000	X, N	Manual	3	Pentamer structure	[6]
(b) Translational and/or rotational searches of separate subunits						
IgM and its fragments	976,000	X, S	Manual	~200	2 Fab and 1 Fc structures	[7]
IgG1 and IgG2 (bovine)	144,000	N	Semi-automated	~200	Crystal structure	[8]
IgE-Fc	75,300	X, N	Automated	37,440	2 Ig folds and 1 Fc structures	[9]
Carcinoembryonic antigen	152,500	X, N, S	Automated	20,280	1 V-type and 6 C2-type Ig folds	[10]
Factor VIIa	51,400	X, N, S	Automated	15,625	4 FVIIa domains	[11]
Tissue factor-FVIIa complex	76,200	X, N, S	Automated	37,044	2 FVIIa and TF structures	[11]
Factor 1	85,300	X, N	Automated	9,600	5 factor I domains in 2 lobes	[12]
(c) Symmetry-constrained translational searches						
AmiC trimers (*P. aeruginosa*)	127,900	X, N	Automated	21	Monomer structure; trimeric symmetry	[13]
SAP decamer	254,000	X, N	Automated	640	Pentamer structure; axial symmetry	[6]
RuvA (*M. leprae*)	165,700	N	Automated	120	E.Coli RuvA structure; axial symmetry	[14]
RuvA-Holliday junction complex	205,100	N	Automated	200	E.Coli RuvA structure; axial symmetry	[14]
MFE-23 (scFv antibody: *E. Coli.)*	27,200	N, S	Manual	3	MFE-23 structure in crystal lattice	[15]
(d) Covalently-connected domain searches by molecular dynamics						
Carcinoembryonic antigen	152,500	X, N, S	Manual	1	1 V-type,3 I-type,3C2-type; 6 CD2 linkers	[16]
IgA1	164,000	X, N	Automated	12,000	2 Fab and 1 Fc structures; 2 covalent linkers	[17]
Factor H	150,000	X, N, S	Automated	16,752	20 SCR structures; 19 covalent linkers	[18]

Table 1: Summary of constrained scattering curve modelling analyses

[1] Proteins are of human origin unless specified otherwise.

[2]. X, X-ray scattering; N, neutron scattering; S, sedimentation coefficients.

models defines the best-fit structures, which are then examined in more detail.

Translational and/or rotational searches of separate domains

Translational and rotational searches of domain fragments provides a straightforward approach for obtaining curve fits. Our first attempt to model a multidomain protein in terms of component crystal structures was made with the antibody IgM. This is a pentameric molecule in which 10 four-domain Fab and 5 four-domain Fc fragments and 11 other domains form a large planar structure in solution. This total of 71 domains was analysed in a stepwise fashion, in which scattering curves for the four-domain Fab fragment, the ten-domain Fab_2 fragment, and the 21-domain Fc_5 fragment were each individually modelled. The scattering curve for the intact IgM structure was then modelled in terms of these three models. The curve fits were achieved using manual rotational and translational searches of small sphere models. The outcome of the modelling was illuminating, as the homology model of the Fc_5 fragment revealed the likely position of a binding site for C1q of complement, which was masked in free IgM, but is exposed when the five Fab_2 fragments are bound to an activating surface [7].

These simple searches were automated for the modelling of the two Fab and one Fc fragments connected by hinge peptides in intact bovine IgG1 and IgG2 antibodies. A translational search optimised the relative positions of these three individual fragments within each molecule. The best-fit models showed that both IgG molecules possessed extended arrangements of these three fragments that allowed full access to the hinge peptides and receptor sites at the centre of each structure [8]. Automation was also applied to the study of the six-domain Fc fragment of human IgE, in which there is an additional pair of domains $(C\gamma2)_2$ in place of the hinge peptide in IgG. This modelling in terms of small sphere models proved to be more complex than anticipated, and was completed by allowing for 37,000 rotations and translations of the $(C\gamma2)_2$ domains and possible rotations in the other domains. The best fit model was defined as the mean structure of the 100 models with the best R-factor values. This showed that a bent IgE-Fc model with a $(C\gamma2)_2$ rotation of 70^o gave a very good X-ray curve fit, and accounted for reports that the intact IgE antibody is itself bent [9]. Another translational-rotational search of the five

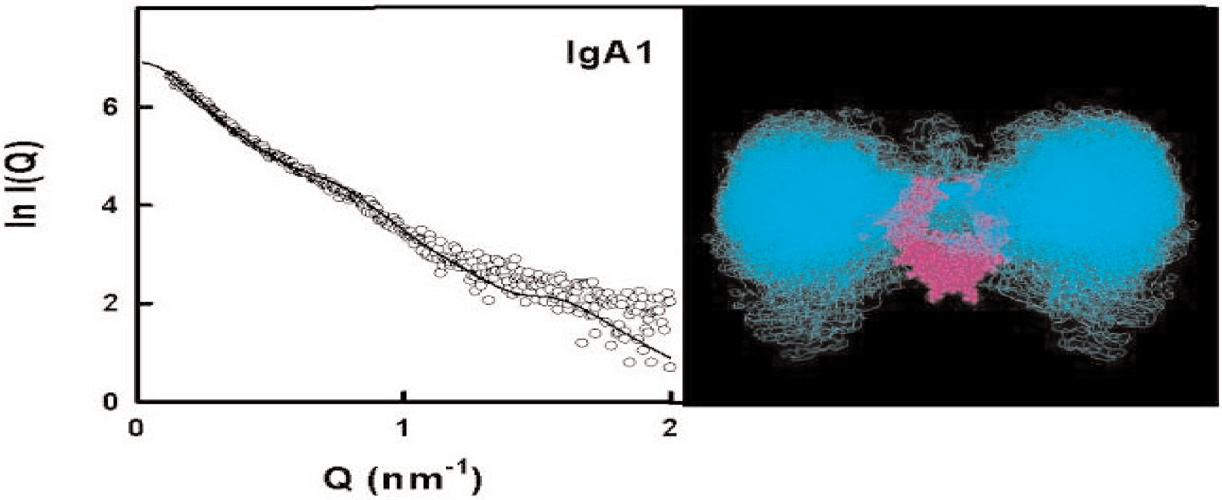

Figure 3: X-ray scattering curve fit for IgA1. The superimposition of 104 best-fit IgA1 models is shown, with the Fc fragment depicted in purple at the centre, and the 104 pairs of Fab fragments are shown in cyan. Adapted from [17].

domains in factor I of complement showed that a two-lobed structure provided a plausible explanation for why its five domains did not form an extended structure in solution [12].

Curve fits can also be obtained by rotation searches. CEA contains seven Ig fold domains, and is 50% carbohydrate. Here, scattering modelling was based on an automated set of systematic domain rotations based on a fixed interdomain separation. The 100 best-fit CEA models showed an extended zig-zag structure with carbohydrate chains extended away from its surface [10].When the crystal structure of an anti-CEA antibody MFE-23 became available, the remodelling of the entire zig-zag CEA structure in terms of the linker conformation observed in the CD2 crystal structure showed that it was possible both to improve the curve fit and to propose a model for its complex with MFE-23 [16]. Another automated domain rotation search showed that factor VIIa of blood coagulation had an extended four-domain conformation [11].

Symmetry-constrained subunit translational searches

Proteins often form oligomeric structures that can be analysed by scattering, for which the most notable feature is that symmetry considerations play a role in the curve modelling. AmiC is a two-domain periplasmic binding protein that was shown by scattering to exist in a monomer-trimer equilibrium. This was unexpected as its crystal structure revealed an antiparallel dimer. As a trimeric structure has a three-fold axis of symmetry, the scattering modelling of the trimer was achieved by arranging the long axes of three monomers parallel to each other about this axis, and optimising the position of the monomers using 21 translations [13]. Asymmetric associations of AmiC monomers and dimers are ruled out as valid scattering models, since these would form indefinitely self-associated structures, which are not observed. A variant of this type of modelling is to use observed crystal lattice packing arrangements as scattering models for oligomer structures in solution, which is possible if symmetric subunit associations are observed [15].

Symmetry considerations lead to the most precise scattering modelling fits. Serum amyloid P component (SAP) is a disc-like pentameric molecule that forms very stable face-to-face decamers in the absence of calcium [6]. RuvA is another disc-like tetrameric molecule that forms face-to-face octamers and binds to a four-stranded DNA helix structure called a Holliday junction [14]. Both SAP and RuvA were modelled by taking advantage of the five-fold or four-fold symmetry axis perpendicular to the plane of SAP or RuvA respectively. In these searches, one molecule was held fixed while the other was translated along the symmetry axis in 0.1 nm steps. Both searches gave two best-fit minima that correspond to the two possible structures formed by face-to-face contacts (cf: Figure 2). For SAP, one decamer structure was rejected as it is devoid of the Trp residues known to be present at the interface between the two pentamers. However there was uncertainty in the outcome of the SAP modelling as the relative rotation between the two pentamers could not be well determined. For RuvA, one of the two octamer structures was rejected as it is devoid of charged groups that would readily account for its formation. This time, there is no uncertainty in the relative rotation between the two tetramers as only one aligned orientation permits the formation of a clear DNA-binding groove between them. This modelling was extended to include the use of neutron contrast variation, which enabled the DNA in RuvA complexed with a Holliday junction to be masked out in the scattering experiment. Neutron data recorded using 65% D_2O permitted the modelling of the protein only in the complex to be carried out (Figure 2). This revealed a gap between the two tetramers, which corresponded in size to the width of a DNA double helix. The modelling concluded by showing that this octameric complex existed in solution, and clarified the significance of crystallographic studies on the tetrameric and octameric forms of this complex.

Covalently-connected domain searches by molecular dynamics

To model a multidomain protein, it is sometimes better to replace the straightforward rotational and translational searches using a fragmented subunit structure with a full covalently-connected structure. This avoids the arbitrary nature of these searches as each model is now stereochemically correct before it enters the curve fit process. If the conformationally variable linker peptides between domains are modelled using structural libraries calculated by molecular dynamics simulations, full models of the protein are generated by an automated process that assembles randomly selected linker peptides with the individual domains to create the full structure. Curve fits then become a trial-and-error procedure that is left to run until a sufficient number of good-fit solutions are obtained. This was applied to determine the solution structure of the antibody IgA1 as an assembly of three well-defined rigid homology models for the two Fab and one Fc fragments joined by two extended 23-residue glycosylated hinge peptides whose conformations were unknown [17]. The best-fit structures showed that the hinge peptides were highly extended and positioned the two Fab fragments far away from the Fc fragment in IgA1 (Figure 3). Such a structure accounted for the location of the IgA receptor site at the centre of the Fc fragment, rather than at the top of the Fc fragment as found in IgG antibodies, as the position of the IgA1 Fab fragments do not obstruct access to this site. The importance of this alternative modelling approach for IgA1 is that the use of translations and rotations became too complex to interpret in this particular case, and gave inconsistent results [17]. The use of molecular dynamics to create peptide libraries offers a powerful strategy that is applicable to other multidomain proteins. For example, its use with the 20 SCR domains and 19 linker peptides in factor H of complement demonstrated that this protein possessed a folded-back domain structure in solution [18].

Conclusions

What is common to all three methods of constrained scattering fits is that, if relevant small crystal structures are available, a large number of possible macromolecular models are generated. Systematic comparisons with the experimental scattering curve then leaves a small number of best-fit structures. The biological significance of these studies is similar to that of standard protein homology modelling, in that the three-dimensional proximity arrangement of key amino acid residues are indicated. For example, the antibody analyses indicated the accessibility of several key residues relative to the other domains for interactions with their receptors. While a good curve fit is only a test of consistency, and will not constitute a unique structure determination, the modelling becomes more useful when the constraints become stronger. Frequently, the modelling complements newly-determined crystal structures by clarifying important details in these. Alternatively, it is possible to analyse structures that crystallographers are unable to solve.

Acknowledgements

The Wellcome Trust, the Biotechnology and Biological Sciences Research Council, and the Clement Wheeler-Bennett Trust are thanked for grant support. Many biochemical collaborators are thanked for their generous provision of samples, and instrument scientists at the SRS, ISIS and ILL provided invaluable support.

References

[1] Perkins, S. J., Ashton, A. W., Boehm, M. K., Chamberlain, D. (1998) *Int. J. Biolog. Macromo*l. 22, 1-16.

[2] Perkins, S. J., Ullman, C. G., Brissett, N. C., Chamberlain, D., Boehm, M. K. (1998) *Immunol. Reviews*, 163, 237-250.

[3] Perkins, S. J. (2000) In *Protein-Ligand Interactions: A Practical Approach* (Eds. B. Chowdhry and S. E. Harding) 1, 223-262.

[4] Smith, K. F., Harrison, R. A. & Perkins, S. J. (1990) *Biochem. J.* 267, 203-212.

[5] Perkins, S. J., Smith, K. F., Kilpatrick, J. M., Volanakis, J. E., Sim, R. B. (1993) *Biochem. J.* 295, 87-99.

[6] Ashton, A. W., Boehm, M. K., Gallimore, J. R., Pepys, M. B., Perkins, S. J. (1997) *J. Mol. Biol.* 272, 408-422.

[7] Perkins, S. J., Nealis, A. S., Sutton, B. J., Feinstein, A. (1991) *J. Mol. Biol.* 221, 1345-1366.

[8] Mayans, M. O., Coadwell, W. J., Beale, D., Symons, D. B. A., Perkins, S. J. (1995) *Biochem. J.* 311, 283-291.

[9] Beavil, A. J., Young, R. J., Sutton, B. J., Perkins, S. J. (1995) *Biochemistry*, 34, 14449-14461.

[10] Boehm, M. K., Mayans, M. O., Thornton, J. D., Begent, R. H. J., Keep, P. A., Perkins, S. J. (1996) *J. Mol. Biol.* 259, 718-736.

[11] Ashton, A. W., Boehm, M. K., Johnson, D. J. D., Kemball-Cook, G., Perkins, S. J. (1998) Biochemistry, 37, 8208-8217.

[12] Chamberlain, D., Ullman, C. G., Perkins, S. J. (1998) *Biochemistry*, 37, 13918-13929.

[13] Chamberlain, D., O'Hara, B. P., Wilson, S. A., Pearl, L. H., Perkins, S. J. (1997) *Biochemistry*, 36, 8020-8029.

[14] Chamberlain, D., Keeley, A., Aslam, M., Arenas-Licea, J., Brown, T., Tsaneva, I. R., Perkins, S. J. (1998) *J. Mol. Biol.* 284, 385- 400.

[15] Lee, Y.-C., Boehm, M. K., Perkins, S. J. (2001) In preparation.

[16] Boehm, M. K., Perkins, S. J. (2000) *FEBS*

Letters 475, 11-16.
[17] Boehm, M. K., Woof, J. M., Kerr, M. A., Perkins, S. J. (1999) *J. Mol. Biol*. 286, 1421-1447.
[18] Aslam, M., Perkins, S. J. (2001) Submitted.

Fibre Diffraction Using the BioCAT Facility at the Advanced Photon Source

T.C. Irving* and R. F. Fischetti.

The Biophysics Collaborative Access Team (BioCAT), Dept of Biological Chemical, and Physical Sciences, Illinois Institute Of Technology, Chicago, IL, 60616 USA.

***Corresponding author: T.C. Irving (312) 567-3489 Fax: (312) 567-3494 e-mail: irving@biocat1.iit.edu**

The BioCAT undulator-based beamline at the Advanced Photon Source (APS), Argonne IL, USA is a state-of-the-art instrument for biological non-crystalline diffraction and X-ray absorption spectroscopy that is generally available to the international scientific community. The design features of this instrument and the unique source properties of the APS allow collection of fibre diffraction patterns of exceptional quality from complex, weakly diffracting biological systems. The small focal spots achievable with this instrument (~40 x 200 microns) has allowed excellent discrimination of fine detail in fibre patterns from muscle and connective tissue as well as detection of weak diffraction features in the presence of large backgrounds. The high X-ray flux of the instrument (~1.5 x 10^{13} photons/s at 12 keV) permits dynamical experiments on these systems with very fast time resolution.

Introduction

The Biophysics Collaborative Access Team (BioCAT) is a US National Institutes of Health - Supported Research Center dedicated to structural studies of partially ordered biological materials using small-angle X-ray diffraction (SAXS), small-angle solution scattering (SAS), and x-ray absorption (XAS) spectroscopy at the Advanced Photon Source (APS) Argonne National Labs, Argonne, IL. The BioCAT facility is open to all researchers on the basis of peer reviewed beam time proposals. Central to the facility is an undulator-based beamline located on Sector 18 at the APS. First monochromatic light from this instrument was achieved in September of 1997. Since then, in collaboration with a number of external groups, we have collected a considerable body of data, most of it in the area of small-angle fibre diffraction. Here we present some of these diffraction images obtained from a variety of complex biological tissues that demonstrate the utility of this instrument for obtaining diffraction patterns of exceptionally high quality with very short exposure times.

The BioCAT Undulator Beamline

The BioCAT undulator beamline has been described in detail elsewhere [1]. Briefly, the APS Undulator "A" [2] was chosen as a source of very intense monochromatic radiation in the 3.2 - 13 keV range (1^{st} harmonic, 9.6-39 keV 3^{rd} harmonic). This photon source has very low angular divergence (16 micro-radian vertical and 56 micro-radian horizontal FWHM at time of writing) with source sizes approximately 50 µm and 850 µm FWHM. The beamline contains two independent double-crystal monochromator assemblies, one equipped with Si (111) crystals, the other equipped with a Si (400) crystals. Both first crystals are liquid nitrogen-cooled. The range of operation with Si (111) crystals is designed to be between 3.2 keV to15.1 keV, with an energy resolution (DE/E) of approximately 2×10^{-4}. The range of operation of the (400) crystals is from 8.0 to 35.0 keV with significantly higher energy resolution. By using the (800) reflection from the crystal and the seventh harmonic of the undulator, energies of up to 70 keV are accessible. The second crystal of either monochromator can be sagittally bent to provide horizontal focussing of the beam independently of any vertical focussing. Downstream of the monochromators is a 1 meter long, downward deflecting, grazing-incidence mirror for harmonic rejection and vertical focussing. The mirror can be used either flat or elliptically bent to allow vertical focussing independently of any horizontal focussing. The placement of the two focussing optics yields maximum theoretical geometric demagnification factors of about 7:1 in the horizontal and 11:1 in the vertical. The convergence angles will range from about 130 microradians vertically and 300 microradians horizontally (focussed at the sample at the end of the 5.7 m beam pipe) to 70 microradians vertically and 200 microradians horizontally. This optical arrangement allows for great flexibility in determining the beam dimensions at the sample and detector to permit optimal matching of the beam dimensions to the sample and desired resolution of diffraction features in the detector plane. Downstream of the mirror are horizontal and vertical collimation slits (range .020 - 6 mm) that are used to define the beam.

The experimental enclosure measures 12 m x 5 m x 3.3 m tall, in order to allow ample room for exotic experiments and to accommodate long cameras (~8m maximum) for small-angle experiments. Within this enclosure is a 1.2 x 1.5 m motorized optical table used for most spectroscopy experiments as well as diffraction experiments using short cameras. Downstream of this table is a 7 x 1.5 m vibration isolation table which is used for most small-angle diffraction and scattering experiments. Such experiments with up to 6 m camera lengths can be accommodated entirely on this one table. The small-angle diffraction camera includes one pair of guard slits that can be positioned at various positions along the beam axis on the 7 m optical table with a minimum separation of the guard and collimation slits of 3 m. Two detectors are currently available for fibre diffraction applications. The first is a Fuji BAS2500 off-line image Plate Scanner which is capable of scanning with either 100 or 50 micron pixels using a16 bit (log) ADC system. The second is a 1024 x 1024 pixel, 60 mm active area, CCD detector optimized for small angle diffraction and scattering developed in collaboration with Dr. Walter Phillips' group, Brandeis University. A second 4k x 7k, 50 x 80 mm active area CCD detector, also developed by the Brandeis group, will be commissioned early in 2001.

Results

The observed size of the unfocussed monochromatic beam at the sample position is typically about 1.2 x 4.3 mm (FWHM). Currently, observed flux is typically 1.5-2.0 x 10^{13} ph/s @100 mA and 12 keV (Si(111) double crystal mono energy resolution). Comparable intensities can be obtained over the entire accessible range of 4-70 keV. Simply collimating this beam to the desired size can provide useful intensities for experiments requiring very good angular resolution. Most experiments, however, have used the double-focussing capability. With a 2m small-angle camera we have observed focal spots smaller than 0.04 x0.2 mm (FWHM). At the shortest possible focal distance, we have observed a vertical beam profile of ~0.017 mm (FWHM). Trimming the incident beam by 10-20% is usually sufficient to obtain a clean, well-collimated beam allowing most of the source intensity to be delivered to the sample.

Using these optics with the small-angle-camera, in collaboration with a number of outside user groups, we have examined a number of muscle and connective-tissue systems. All of these systems benefit greatly from the very small focal spot and the low beam divergence delivered by this beamline. Figure 1 shows an expanded view of a diffraction pattern from an isometrically contracting frog sartorius muscle (taken in collaboration with H.E. Huxley and M. Reconditi, Brandeis University and University of Florence) obtained with a 5.7 m camera. This shows the fine detail on the meridian and the layer lines achievable with this optical arrangement where the focal spot size (~70 x 250 µm) is similar to the pixel size (60 µm). The fine vertical collimation allows very good resolution on diffraction features in the meridional direction. In this example, it allows resolution of the substructure in the well-known 14.5 nm (m3) meridional reflection from striated muscle. The m3 is a fairly broad reflection due to the axial projection of the myosin heads (the enzymatic part of the myosin molecule responsible, in concert with actin, for motion in muscle) onto the fibre axis. Since muscle thick filaments are bipolar structures, there will be interference due to myosin heads on opposite ends of the thick filament (~800 nm)(3). The resulting pattern will be exquisitely sensitive to changes of myosin head orientation along the fibre axis since the muscle itself is being used as an interferometer. Experiments are ongoing with both the Huxley group and the M. Irving (Kings College London)/V. Lombardi (Florence) collaboration leading independent efforts. The fine focus and good resolution of our CCD detector have been highly advantageous for these studies.

Another area where this high degree of angular resolution is of great utility is in discriminating fine detail in the presence of high backgrounds. We (in collaboration with D. Maughan University of Vermont, see reference [4]) recently showed that it was possible to obtain good quality diffraction patterns from the indirect flight muscle (IFM) of living fruit flies with 2 ms time resolution, enough to resolve structural changes during the ~200 Hz wing beat cycle. This system is attractive not only because it allows studies *in vivo*, but, because of the ease of genetic manipulation of this organism, it allows the power of modern molecular genetics to bear on structural studies of muscle. In these experiments the beam traversed not only the IFM but the chitin shell of the thorax and probably the legs as well. Figure 2 shows: (a) a raw pattern where only the very strongest reflections are easily seen and (b) a background subtracted image (using the XFIX program from the CCP13 suite assuming a radially symmetric background) where the layer lines are clearly resolved.

Since we typically perform our SAXS experiments at the relatively high beam energy of 12 kev (1.03 A) it is possible to obtain diffraction patterns from relatively thick specimens. In collaboration with J. Mollenhauer, University of Jena, and C. Muehleman, Rush University, we have exploited this ability, along with the excellent focal properties of the beamline, to obtain X-ray patterns from human ankle cartilage in order to examine the structural arrangement of collagen fibres as a function of location in the cartilage. For this work we were able to use samples ~ 10 mm wide by 1.5 mm high by ~ 5 mm thick. These thick, minimally processed, samples reduced the danger of preparative artifacts, thus providing a good indication of the average orientation of the collagen fibres with respect to depth in the tissue. Figure 3 shows a panel of images showing the change in orientation and degree of ordering with depth in normal ankle cartilage. We have now completed a study (in preparation for publication) of spatially resolved (~0.1 mm) collagen fibre orientations in normal cartilage and in cartilage damaged due to trauma and/or osteoarthritis.

Conclusions and future developments

The BioCAT undulator beamline has been shown to be an excellent instrument for static and time-resolved small-angle fibre diffraction. It is now being widely used by the muscle and connective tissue community. The APS will be reducing the horizontal emittance of the source with the goal of reducing the horizontal source size by a factor of 2. This will reduce our focal spot sizes accordingly with no loss of flux. We are starting to set up for conventional high-resolution fibre diffraction of, for example, filamentous viruses with the first experiments scheduled for the first quarter of 2001. We expect that the high flux densities available will be advantageous for the study of small oriented regions The small source size and very low angular divergence of the undulator source also make it ideal for micro-diffraction experiments using zone-plates or Kirkpatrick-Baez mirrors to achieve focal spots of sub-micron dimensions. We plan to test a zone plate with a 0.3 micron focal spot with ~ 1 milliradian convergence angle in the summer of 2001. This would allow *in situ* small-angle diffraction experiments to very high spatial resolution in

Interference from myosin heads on opposite sides of A-band

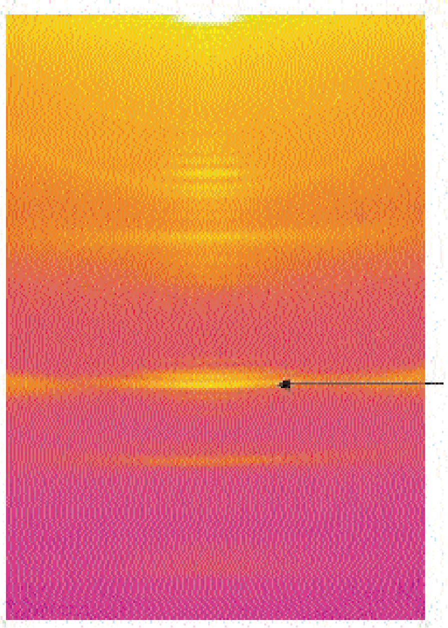

Fine structure in the 145 Å reflection from frog muscle showing > 8000 Å order to order resolution

Figure 1: Close-up view of a diffraction pattern from an isometrically contracting frog sartorius muscle showing the fine detail on the meridian and the layer-lines that can be obtained with the biocat undulator based beamline and the fuji bas2500 detector with bas v imaging plates. Note the fine structure in the 145 Å reflection showing the high order to order resolution. (Focal spot size ~0.040 x 0.2 mm, total flux 1 x 10^{13} photons/s).

complex biological tissues.

Acknowledgements

We would like to thank Drs. H.E. Huxley, M. Reconditi, D. Maughan, J. Mollenhauer, M. Aurich and C. Muehleman for permission to show their unpublished data. We would also like to thank all the BioCAT staff for their help in developing this facility. Use of the Advanced Photon Source was supported by the U.S. Department of Energy, Basic Energy Science, Office of Energy Research, under Contract No. W-31-109-Eng-38. BioCAT is a NIH-Supported Research Center, under cooperative agreement #RR08630

References

[1] Irving, T.C., Fischetti, R., Rosenbaum, G. & Bunker, G.B. (2000). Fibre Diffraction Using the BioCAT Undulator Beamline at the Advanced Photon Source. *Nuclear Instruments and Methods(A)* 448:250-254.

[2] Lai, B., Khounsary, A., Savoy, R., Moog, L. & Gluskin, G. (1993) "Undulator A Characteristics and Specifications" *ANL/APS TB-3*

[3] Huxley, H.E., Reconditi, M., Stewart, A. & Irving, T.C. (2000). Interference Changes on the 14.5 nm Reflection during rapid length changes. *Biophys. J.* 78:134a. (abstract)

[4] Irving, T.C. & Maughan, D.W. (2000). In vivo X-ray diffraction of indirect flight muscle from Drosophila melanogaster. *Biophys. J.* 78:2511-2515.

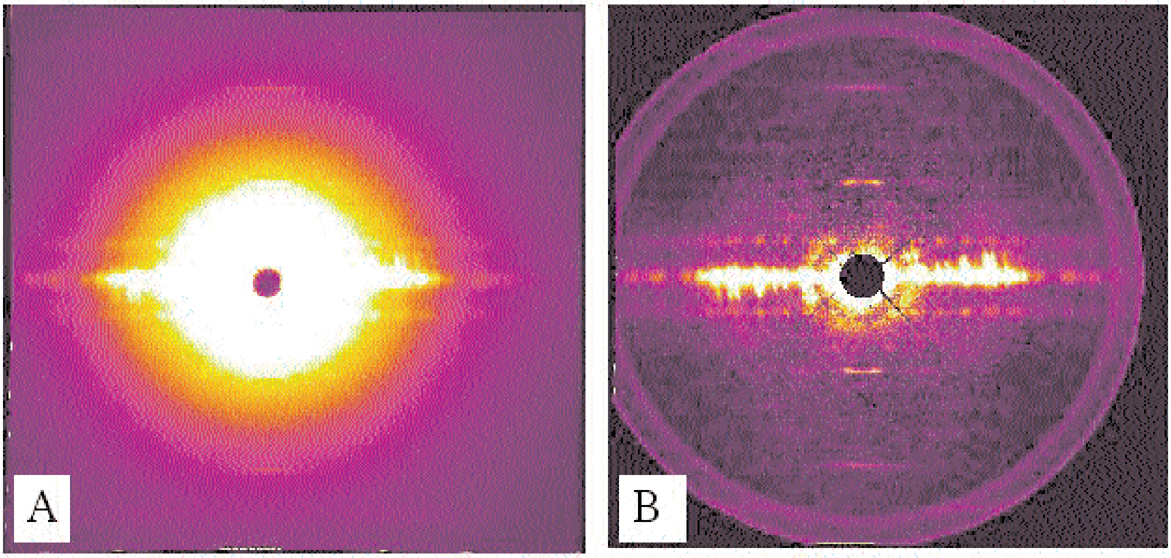

Figure 2: Diffraction pattern from the indirect flight muscle of a live fruit fly: (A) A raw image showing the high background obscuring the main diffraction feastures; (B) The same image from which a radially symmetric background was subtracted using XFIX to show the layer-lines. The set of spots at an angle to the equator come from a different set of muscles.

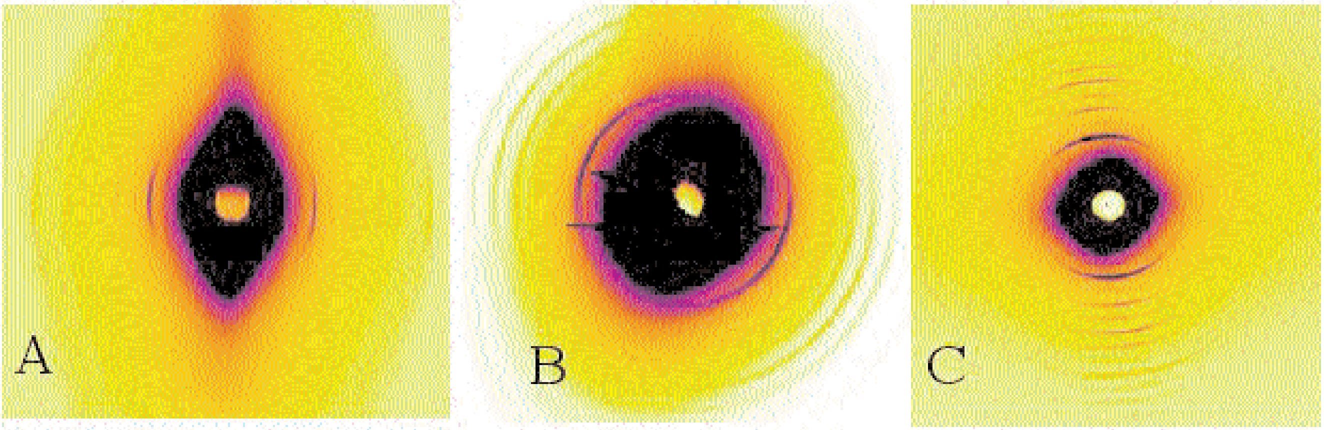

Figure 3: Three diffraction patterns from human articular cartilage showing the change in collagen fibre orientations as a function of depth: (A) Superficial layer where fibres are horizontal; (B) Middle layer where fibres are isotropically orientated and (C) the deep layer where they are oriented perpendicularly.

X-ray diffraction study of silicon oxycarbide glasses

H. Brequel, S. Enzo

Dipartimento di Chimica Via Vienna, 2 07100 Sassari (Italy)

Silicon oxycarbide compounds are promising materials with potentially improved properties compared to classical ceramics. They are amorphous and similar to silica, but with some oxygen atoms substituted by carbon. In order to better control the insertion of carbon atoms in the network, the Sol-Gel method was chosen as an alternative to the classical high temperature synthesis. Here, the mixture is made of two precursors with different content of Si-O and Si-C bonds: methyldiethoxysilane $HSi(OEt)_2CH_3$ (MDES) and triethoxysilane $HSi(OEt)_3$ (TREOS). Each precursor leads to interconnected units with 2 (DH) and 3 (TH) silicon – oxygen bonds in the gel, respectively. During the hydrolysis and the condensation process there is no decomposition or loss of the carbon functional group, so that the final composition of the polysiloxane network is closely related to the initial atomic ratios (O/Si) and (C/Si). Subsequently, a pyrolysis under inert atmosphere is performed at various temperatures between 1000°C and 1500°C in order to remove the organic part of the material. This leads to a glass or partially amorphous ceramic. The structure of the materials obtained is investigated by X-ray diffraction techniques. When the materials are totally amorphous, the Radial Distribution Function approach is carried out from XRD patterns. On the other hand, the Rietveld method is used to fit the patterns when crystalline species are arising (high temperature of pyrolysis). This work is done under the European TMR contract # FMRX-CT98-0161, « Oxycarbide glasses » network.

Mesh Intermediate Phases in Surfactant-Water Mixtures

Marc Leaver*, Mike Holmes, Andrew Fogden(#) and Smita Puntambekar

Centre for Materials Science, Department of Physics, Astronomy and Mathematics, University of Central Lancashire, Preston, PR1 2HE,Lancashire, United Kingdom

(#)Physical Chemistry 1, Chemical Centre, Lund University, S-221 00 Lund, Sweden

Concentrated mixtures of amphiphiles and water can exhibit a number of liquid crystalline phases. The number, complexity and structure of the phases that are formed depend on the structure of the amphiphile in addition to the temperature and composition of the system. Whilst the structure of many of the liquid crystalline phases are delineated, a number remain a challenge. One such phase is the 'intermediate phase'. The structural units for such phases usually possess non-uniform interfacial curvature and are stable at amphiphile concentrations between that of the hexagonal and lamellar phases. In this presentation the structure of mesh intermediate phases formed in binary surfactant water systems will be discussed. Experimental results, from a number of techniques, will be presented to determine the stability range and structure of such phases formed in model non-ionic and ionic fluorocarbon surfactant systems.Having established the structure of the phase models for the structure of the phase are presented.

Daresbury Analytical Research & Technology Service

E.J. MacLean, J.M. Charnock, S.M. Slawson, R.W. Strange,E.Towns-Andrews

CLRC Daresbury Laboratory, Daresbury, Warrington, Cheshire, WA4 4AD

Daresbury Analytical Research and Technology Service (DARTS) offers tailored data collection and analysis services for academic and industrial users of the Synchrotron Radiation Source (SRS) at Daresbury Laboratory. The service provides a host of analytical techniques extending from hard X-ray to infrared for investigation of material science problems. The Service makes use of the myriad of techniques available using synchrotron radiation (SR) including: • protein crystallography • infrared microscopy • powder diffraction (including grazing incidence and reflectivity) • "micro-crystallography" • X-ray absorption spectroscopy • small and wide angle X-ray scattering • circular dichroism. By employing a range of techniques, it is possible to look at many different types of materials using the DARTS service such as polymers, inorganic samples, proteins, cells, glasses, mixed phases and formulated mixtures.

The formation of polymer-polymer interfaces

D.G.Bucknall*, S.Butler, J.S.Higgins

Dept Chemical Engineering, Imperial College, London *Dept of Materials, University of Oxford

The reinforcement of interfaces between polymeric materials, either by interdiffusion across the interface, or by the use of compatibilisers such as copolymers, raises interesting questions in fundamental polymer science, while being of considerable technological importance. Many artefacts made from polymers are moulded at elevated temperatures. The utility of the final article depends on the strength of the bond formed when two flowing and cooling fronts meet at a joint or seam. Understanding the interdiffusion of polymer molecules and hence the time dependent structure of the forming interface, is key to understanding its subsequent mechanical strength. Compatibilisers are added to otherwise immiscible polymers during processing in order to strengthen the material at internal interfaces which would otherwise be weak. This is aimed at making useful new materials and exploiting synergies between the properties of the different species. One modern technique which has provided key information about polymer interfaces is neutron reflection. We report results from interfaces between miscible and immiscible polymer layers with and without the addition of copolymers. Recent data have been obtained in real time as the interfaces form without the need for quenching.

A Study of Structural Development and Morphology during Crystallization of Linear Hydrogenated Polybutadienes using Small & Wide-angle X-Ray Scattering (SAXS/WAXS) and DSC Techniques

E.L.Heeley, C.M.Fernyhough, A.Pryke, W.Bras*, R.J.Hanson & A.J.Ryan

Department of Chemistry, University of Sheffield, Sheffield, S3 7HF, UK

*ESRF, BP220, F-38043. Grenoble Cedex, France

Many semi-crystalline polymers are used in countless areas of everyday life. The overall structure of these polymers controls the aesthetic and mechanical properties of the material, which invariably affects its end use. The production of such polymeric materials requires much physical and chemical optimisation pertaining to its application. Thus, it is necessary to understand and develop further, a complete picture of the material's properties and relate this to its structural morphology. The structural morphology of a polymer can be described and controlled by its molecular crystallization. This is inherent from its chemical construction and mode of processing. The structural development in polymers during crystallization is generally well understood regarding the growth of crystals and several theories have been conceived to describe this over the last forty years(1). However, one area of crystallization kinetics which is vaguely understood, is that concerning the primary nucleation process prior to the growth period. Reasons for this lack of understanding lie in the difficulties of obtaining experimental data to support and expand pre-existing theories(2). Fortunately, polymer nucleation and crystallization takes place at a molecular level, which can be appropriately studied by X-ray scattering techniques. Here, experimental determination of nucleation in crystallizable linear hydrogenated polybutadienes has been studied with the aid of time-resolved X-ray scattering methods and Differential Scanning Calorimetry (DSC). Several linear polybutadienes (Mw 2-500k) were synthesized with controlled molecular architecture, using anionic methodology(3) and subsequently hydrogenated to give samples having a narrow molecular weight distribution. The crystallization and melting point information was then determined for each sample using classical laboratory DSC techniques. From this several isothermal crystallization temperatures were chosen in the sample melt for X-ray measurements. Time-resolved Small- and Wide- Angle X-ray Scattering (SAXS/WAXS) and DSC experiments were all performed at the European Synchrotron Radiation Facility (ESRF), France or the Daresbury Synchrotron Radiation Source (SRS), UK. Here, several polymer samples were crystallized in the melt at various temperatures whilst the SAXS/WAXS data were obtained. The SAXS/WAXS data collected provides an insight into the macro- and micro-molecular structure during the crystallization of the polymer sample. The SAXS details information on the long range structural ordering having associated density changes, whereas WAXS probes the ordering at an atomic level. Here, it has been possible to study the primary nucleation of crystallization, in terms of the spinodal decomposition theory described by Cahn-Hilliard(4) from the X-ray scattering data obtained. This has been seen with the hydrogenated polybutadienes studied during crystallization in the melt, when density fluctuations give rise to SAXS peaks during an induction period but, no WAXS Bragg peaks accompany these. The results indicate that crystallization in the melt consists of an induction period where large scale ordering persists prior to crystal growth. Evaluating such data will enable a complete picture of crystallization and associated kinetics to be determined. In turn this will provide valuable information in potentially controlling the final morphology and physical properties of a polymer material in terms of its specific end use.

[1] Billmeyer, F.W. '*Textbook of PolymerScience*' 1984, 3rd edition, Wiley Interscience.
[2] Ryan, A.J., Fairclough, J.P.A., Terrill, N.J., Olmsted, P.D. & Poon, W.C.K. *Faraday Discuss*., 1999, 112, 13.
[3] Rachapudy, H., Smith, G.G., Raju, V.R. & Graessley, W.W. *Polym. Sci., Polym. Phys. Edn*. 1979, 17, 1211.
[4] Cahn, J.W. & Hilliard, J.E. *J. Chem. Phys*., 1958,28, 25.

Reaction Kinetics and Morphology Development in Flexible Polyurethane Foam

Wu Li, Ellen L Heeley, Anthony J Ryan

Department of Chemistry, University of Sheffield, Sheffield S3 7HF

Flexible polyurethane foams are formed from the simultaneous exothermic reaction between a diisocyanate with a polyether polyol and water. The morphology of these foams is determined by the competition between the polymerisation and the microphase separation of the ‘hard’ and ‘soft’ segments. The hard-segments are formed by the water and diisocyanate reaction producing a polyurea, whereas the soft-segments are formed by the polyether polyol chains. Adiabatic temperature rise measurement (ATR) and forced-adiabatic FT-IR spectroscopy (FT-IR) have been employed to simultaneously monitor polymerisation on a toluene diisocyanate (TDI) based flexible polyurethane foam system, varying the content of surfactant and catalyst. The decay of isocyanate is correlated to the polymerisation kinetics. There is a good correlation between the conversion of isocyanate calculated from ATR and FT-IR data. As the catalyst concentration in the formulation is increased, it has been observed that the overall relative rate of reaction increases. However, the overall relative rates of reaction are the same among the foaming systems with different surfactant concentration. Forced-adiabatic, time-resolved synchrotron small angle X-rays scattering (SAXS) has been employed to investigate the dynamics of microphase separation during the fast bulk copolymerisation. Initially, there is little scattering (homogeneous liquid), and the peak that starts to grow at $q^*=0.06$ Å^{-1} after 81 seconds is evidence for the structural development in the sample. The peak position does not change during the whole process. Microphase separation was observed to occur at a critical conversion of isocyanate functional groups and is shown to follow the kinetics associated with spinodal decomposition. The presence of covalent cross-links is observed to delay the microphase separation of the urea hard-segments. Dynamic rheological measurements have been conducted during the bulk copolymerisation via a vane rheometer. The increase of the modulus of the foaming mixture is resulted from the microphase separation of the hard-segment.

Fibre diffraction and diversity in filamentous plant virus structure

Gerald Stubbs, Greg Ferrell, Mitzi Reams, Nicholas Fletcher

Vanderbilt University

Fibre diffraction has a long history of successful structural analysis of tobamoviruses such as tobacco mosaic virus. Nevertheless, studies of other filamentous plant viruses have been fraught with difficulties. In general, these difficulties stem from specimen preparation rather than the inherent complexity of the viral structures. In some cases it is difficult to obtain sufficient quantities of virions. The members of some virus groups are notoriously difficult to handle in solution. Even when these problems are solved or not present, virions are often difficult to orient. The flexibility of the virions in many groups has contributed to orientation problems. Structure determination at atomic resolution has been completed for four tobamoviruses and partially refined structures have been obtained for two others. Although no molecular details have yet been elucidated, fibre diffraction studies of tobraviruses, hordeiviruses, and potexviruses have been described by various groups. Our current work is focussed on the potexviruses, and we are also attempting to obtain diffraction data from tobraviruses and potyviruses.

A High-angle X-ray Diffraction Study of Collagen Fibre Structure in uniaxially Pre-strained Leather

C. Boote[1], M. Otunga[2], E.J. Sturrock[2], G.Attenburrow[2], K.M. Meek[1]

[1] Dept. of Optometry and Vision Sciences, Cardiff University, Redwood Building, King Edward VII Avenue, PO Box 905, Cardiff CF10 3YJ, Wales UK.

[2] The Leather Sellers Centre, University College Northampton, Park Campus, Boughton Green Road, Northampton NN2 7AL, UK.

A structural investigation into the fibrous collagen assembly which constitutes leather is presented. High-angle X-ray fibre diffraction patterns from uniaxially pre-strained bovine leather samples have been recorded on beamline 7.2 at the Daresbury SRS. The orientation of collagen fibres has been estimated from the azimuthal intensity distribution of the annular reflection deriving from the regular spacing of molecules within collagen fibrils. The X-ray data is presented along with mechanical data previously recorded in order to deduce the influence of industrial pre-straining on the strength, and hence quality, of the material during manufacture, and their relationship to the fibrous microstructure.

New approaches and programs for non-crystalline diffraction data analysis

Dmitri Svergun

European Molecular Biology Laboratory, Hamburg Outstation, EMBL c/o DESY, Notkestrasse 85, 22603 Hamburg, Germany, and

Institute of Crystallography, Leninsky pr., 59, 117333 Moscow, Russia

Advanced methods for the interpteration of scattering from different types of disperse systems are presented. For monodisperse systems, ab initio low resolution shape determination methods using envelope functions and dummy atoms are compared. The algorithms for computation of the scattering profiles from atomic models accounting for the hydration shell and for rigid body refinement are described. The methods to analyse the internal structure of particles by simultaneous fit of contrast variation data are presented. For polydisperse systems, the algorithms to interpret scattering from mixtures of particles of different types are described. In a linear case, they permit e.g. determination of the oligomer content in protein solutions. In a general case, a constrained non-linear optimisation is employed to find polydispersity and volume fractions and interactions between the components. The above methods are integrated into a program suite for advanced data analysis at the EMBL, Hamburg Outstation and are coupled with three dimensional graphic programs on IBM-PC and major UNIX platforms. Examples of their applications to the structure analysis of bioogical macromolecules, microemulsions, and nanoparticles in polymer matrices are given.

Application of SANS in the study of a surfactant layer adsorbed on anisotropic clay particles

I. Grillo*, P. Levitz** and Th. Zemb***

*ILL, DS/LSS, Av. des Martyrs, 38042 Grenoble Cedex 9

** CNRS, CRMD, 1 bis rue de la Férollerie, 45071 Orléans Cedex 2

*** CEA Saclay, DRECAM/SCM, 91191 Gif/Yvette Cedex

D11 and D22 are the two Small-Angle Neutron Scattering facilities at the ILL with the highest flux at the sample position, in a wavelength range of 4 to 40 Å. They are mainly used for soft condensed matter and biologic studies to determine the size, shape and long-range order of small colloidal particles, proteins, polymers, fibers,… Firstly, the technical features of D11 and D22 will be described (flux, sample environments,...).Secondly, an application of SANS, for the structural characterization of a surfactant layer adsorbed on anisotropic clay particles will be presented.

Polyisocyanurates as Functional Damping Coatings

A.L. Abbott, A.J. Ryan, M.L. Turner

Department of Chemistry, University of Sheffield Dainton Building, Brook Hill Sheffield, S3 7HF

Poly(ether-isocyanurate) elastomers formed from polyethers and diisocyanates can be made with variable stiffness, or glass transition temperature, by combining rigid, three dimensional cross linked molecular structures with flexible chains. Cross linking arises from the catalysed trimerisation of isocyanate end groups to form an isocyanurate ring. The reaction between the polyether diols and excess diisocyanate to form a diisocyanate functional copolymer is used and the unreacted diisocyanate distilled off. In a thin film separation of oligomers of various lengths occurs, due to the requirement of free volume for the chain ends. Trimerisation of the end groups in the resulting mixture will lead to a graded cross link density, and thus graded stiffness properties. Materials of this type are of interest for use as vibrational dampers, since they act as constrained layer damping coatings. The coatings are characterised by rheology, reflectivity, SAXS, and FTIR microscopy.

Synchrotron X-ray diffraction studies of the mechanism of contraction in intact single fibres from skeletal muscle

Malcolm Irving

School of Biomedical Sciences, New Hunt's House, King's College London, Guy's Campus, London SE1 1UL, UK

Improvements in the brightness and collimation of available synchrotron X-ray beams over the last few years have driven three types of development in X-ray studies of the mechanism of muscle contraction. First, the brightest X-ray reflections can now be recorded from a short segment of a single muscle cell (a fibre) which is structurally homogeneous and under precise physiological control. Second, kinetic studies of changes in these reflections can be made with sub-millisecond time resolution, which is fast enough to isolate the structural transitions that drive force generation in muscle. Third, fine structure of the X-ray reflections arising from interference between the two arrays of myosin molecules in each muscle sarcomere can be resolved; this interference effect allows Ångstrom-scale motions of the myosin molecules to be measured. Crystallographic studies have produced atomic models for the contractile proteins actin and myosin, and for the conformational change in myosin that is thought to drive force generation. These atomic models have been used to interpret fibre diffraction data, and have led to a detailed model for the mechanism of the myosin motor in muscle. Examples of these developments will be presented using X-ray data collected at beamline 16.1 at CLRC Daresbury, and ID2-SAXS at ESRF Grenoble, as part of a long-term collaboration with the group of V. Lombardi and G. Piazzesi (Università di Firenze) and of M.A. Ferenczi (National Institute for Medical Research, London).

Influence of flow and deformation on block copolymer melts

Frank S. Bates

Department of Chemical Engineering and Materials Science, University of Minnesota, Minneapolis MN 55455

The macroscopic state of order in block copolymers can be influenced by flow and deformation. A plethora of experimental studies have documented the effects of flow geometry, strain amplitude, strain rate, proximity to the order-disorder transition, and molecular architecture on the state of alignment of lamellae, cylindrical and other block copolymer morphologies when subjected to steady and oscillatory deformation. This lecture will focus on model linear block copolymers near the order-disorder transition (ODT) temperature. Diblock, triblock and pentablock copolymer melts have been investigated using in-situ large amplitude shear with simultaneous small-angle neutron scattering. The results of these studies clarify the role of mechanical contrast in controlling the orientation of lamellae and cylinders in the ordered state, and the shear-rate dependence of the ODT. Resulting anisotropic mechanical properties, particularly failure, of the solidified specimens confirms the importance of molecular architecture and processing conditions in this class of nanocomposites.

Crystallisation of cordiriete glass studied with SAXS and WAXS

W. Bras, M. Oversluizen, G.N. Greaves, S.M. Clark

DUBBLE CRG / ESRF Netherlands Organisation for Scientific Research

Aberystwyth University

Daresbury Laboratory

The crystallisation of glass after at high temperatures can be rather complicated depending on the composition and phase diagram of the glass. Several different crystalline structures can evolve in which it is not always clear what the order of the different events is. Moreover, the overall shape, size and growth mode of the crystallites themselves poses an interesting problem for both applied as well as fundamental physics. We have addressed these issues by using high temperature SAXS and WAXS.

Collagen Organisation in the Corneas of Developing Chicks

Veronique Siegler, Keith Meek, and Andrew Quantock

Cardiff University

One important aspect of the cornea's ultrastructure that is thought to influence transparency is the mode of packing of its constituent collagen fibrils. X-ray diffraction studies of developing chick corneas show a general trend for more mature corneas to have more closely packed collagen; the mean centre-to-centre collagen fibril spacing a week before hatching (when the cornea is hazy) being approximately 20% higher than a day or two before hatching (when the cornea is transparent). The level of corneal hydration also drops during development, and our measurements show that the bulk of this tends to take place 3 to 5 days before hatching. X-ray diffraction studies of developing chick corneas should provide us with a better appreciation of the spatial arrangement of collagen during tissue maturation, compaction and transparency acquisition.

The Synthesis of Model Hydrogenated Polybutadienes and their Crystallisation Behaviour

C.M. Fernyhough, E.L. Heeley, A. Pryke, A.J. Ryan, R.N. Young

Department of Chemistry, University of Sheffield, Brookhill, Sheffield. S3 7HF

By synthesising polymers using "living" techniques, control can be exerted over various parameters such as molecular mass, polydispersity, architecture and microstructure. Butadiene can be polymerised anionically then hydrogenated to give a semi-crystalline polymer, analogous to poly(ethylene-co-butene). Initially, linear hydrogenated polybutadienes (hPBd) have been synthesised. They have polydispersities of <1.05 and predetermined molecular weights ranging from 2,200g/mol to 500,000g/mol. hPBds with "comb" structure have also been produced in order to investigate the effects of long-chain branching i.e. by varying the length and number of branches, the crystallisation behaviour may be altered. Preliminary experiments have been performed using Differential Scanning Calorimetry (DSC) and the results of isothermal crystallisation have been used to devise experiments using simultaneous SAXS/WAXS/DSC to probe long-range structural changes prior to nucleation.

Crystal structure studies on cellulose polymorphs

Yoshiharu NISHIYAMA, Paul LANGAN*, Masahisa WASA, Henri CHANZY**

The University of Tokyo (Japan)

* Los Alamos National Laboratory (U.S.A)

** CERMAV / CNRS (France)

We are involved in a long-term project to determine precisely the molecular and crystal and structure of the main cellulose polymorphs. For native cellulose or cellulose I, we have selected specimens having large crystalline domains and developed a method to extract the cellulose crystals and re-orient them uniaxially for X-ray fibre diffraction recording. We used cellulose from (i) the tests of Halocynthia roretzi (a sea animal) corresponding to 1b allomorph (ii) the cell wall of Cladophora wrightiana (a sea weed) corresponding to Ia+Ib allomorphs and the cell wall of Glaucocystis nostochinearum (a micro alga) corresponding to the pure Ia allomorph. As these samples presented some uniplanar axial orientation, a method was developed to derive the orientation function of the crystals with the goal of obtaining a reliable diffracted intensity data set for structure refinement. Cellulose II resulted either from the alkali treatment of cellulose I (mercerization) or the regeneration of cellulose solutions. Other highly oriented specimens included the preparation of cellulose III-I and cellulose III-II resulting from a high-pressure ammonia treatment of respectively Cladophora and cellulose II. The samples of cellulose II had conventional fibre symmetry and from their fibre diagrams we could extract the diffraction intensities using the CCP13 software suite. Combining the phases resulting from the X-ray refinement with the amplitudes from neutron diffraction data followed by Fourier analysis resulted in the positioning of the hydrogen atoms involved in the H-bondings.

Low-angle X-Ray Diffraction Studies of the Corneas of Transgenic, Lumican-Deficient Mice

Andrew J. Quantock, Keith M. Meek, Jennifer Paul,* Shukti Chakravarti*

Cardiff University

* Case Western Reserve University, Cleveland, Ohio.

An electron microscopic study of the hazy corneas of mice homozygous for a null mutation in lumican, an important corneal proteoglycan, has reported that the lateral fusion of collagen fibrils may locally increase the interfibrillar space (Chakravarti et al. J Biol Chem 1998;141:1277-86). To examine the extent of this, we studied the corneas of lumican knockout mice by X-ray diffraction. Low-angle X-ray patterns from 6-month-old, wild-type corneas contained well-defined interfibrillar reflections. X-ray patterns from 6-month-old mutants, on the other hand, contained no appreciable interfibrillar reflection. The absence of well-defined interfibrillar reflections in the corneas of lumican-deficient mice thus implies widespread loss of order.

Investigation of the morphology of thin films prepared from solutions of block copolymers and their blends

C.L.O. Salou, A.J. Ryan and J.P.A. Fairclough

University of Sheffield, Chemistry Department

Diblock copolymers upon cooling (from the melt) or upon solvent evaporation (from solution) exhibit different microphase-separated morphologies including spheres, hexagonally packed cylinders and lamellar structures. The relative volume fraction of each block along with the Flory-Huggins interaction parameter (χ) and the degree of polymerisation dictates the phase separation.

For this project, the lamellar morphology is of interest. It requires using materials with the volume fraction of one block being $0.4<\phi< 0.6$, to obtain alternating layers. If asymmetric starting materials are used, it is possible to obtain a lamellar morphology by preparing blends with homopolymer(s). In these blends, the free energy is reduced when the homopolymers segregate to the appropriate domains of the ordered structure reducing the number of unfavorable segmental A/B contact. The microdomains swell in order to accommodate the homopolymers resulting in transitions from one type of microstructure to another in the process[1].

Solutions of commercially available diblock copolymers, polystyrene-polybutadiene (PS-b-PB) or polystyrene-polyisoprene (PS-b-PI), with homopolymer(s) were prepared in toluene. Four polymers are used in this study; an asymmetric PS-b-PB (~83,000 g.mol^{-1},ϕ_{PS}=0.36), a symmetric PS-b-PB (~300,000 g.mol^{-1},ϕ_{H} PS= 0.46), and two PS-b-PI (600,000 g.mol^{-1}, ϕ_{H}~0.4 and 0.5). The homopolymer(s) was added to the diblock copolymers in order to obtain series of samples with different volume fractions of homopolymer but with symmetrical morphology (i.e., $0.4<\phi_{PS}<0.6$). The solutions were spin-cast onto polished silicon wafers, covered with a native oxide layer. The uniformed thin films were investigated by X-ray reflectivity to determine their total film thickness and by Neutron reflectivity to determine the lamellar spacing. The same solutions were also used to cast films using a draw bar. These films were embedded into epoxy and once polished, the samples were used for AFM and ESEM works. Such techniques are used to image the ordering of the microdomains within the films. From the evaporated solutions, bulk samples were prepared and used to determine the d-spacing by Small Angle X-ray Scattering, and by Transmission Electron Microscopy.

From this work, it was shown that the d-spacing increased upon increase in volume fraction of homopolymer in the blends. Nevertheless, from our neutron reflectivity results it was suggested that the addition of homopolymer to the diblock copolymer was limited. Above a certain value the once flat interfaces were distorted. This problem could be overcome by using a block copolymer with higher molecular weight, giving a repulsion criterion α close to zero[2].

[1] K. I. Winey et al, *Macromolecules*, 1991, 24, 6182

[2] M. W. Matsen, Private Communication

Templated crystallisation: soft phases controlling hard materials

J.P.A. Fairclough, S. Turner, S-M. Mai, C. Booth, W. Bras, I.W. Hamley, M.W. Matsen & A.J. Ryan

Department of Chemsitry, University of Sheffield, Sheffield, S3 7HF.

Throughout nature, the structure of hard materials eg bone, is controlled by a soft template. We have examined crystallisation in shear oriented block copolymers, where a soft phase of microphase separated melt controls the preferred direction of crystallisation. In lamella phases, the comparison is simple and direct over a range of molecular weight and domain sizes. For hexagonal arranged cylindrical systems and for cubic gyroid structures, the choice of preferred directions is limited. We have used real time SAXS & WAXS to monitor the structure formation upon crystallisation paying particular attention to the orientation of the crystal stems with respect to the lamellar interfaces. Recent experiments at the ESRF will also be reported. The microfocus beamline was used with an X-ray spot of 10 microns. Diffraction was recorded from 500 to 1 Å on one detector from single grains of block copolymer during crystallisation.

The relationships between morphology, irradiation and the ductile-brittle transition of isotactic polypropylene

X.C. Zhang, M.F. Butler and R.E. Cameron

University of Cambridge, Department of Materials Science and Metallurgy, New Museums Site, Pembroke Street, Cambridge, CB2 3QZ

The effect of initial morphology, irradiation, and temperature on the micromechanical response of polypropylene is explored using simultaneous SAXS and tensile deformation. Several deformation mechanisms were identified including lamellar separation and shear, stable and unstable fibrillated deformation and cavitation. The ductile-brittle transition rises dramatically with irradiation, while the glass transition shows only a small increase. Changing the initial morphology moderates the effect of irradiation.

The Phase Behaviour of BEB block copolymer solutions

A. Norman*, J.P.A. Fairclough, S.C.Turner, S.Mai, C.Booth

University of Sheffield, Dept. of Chemistry University of Manchester.

*Manchester Polymer Centre

The phase behavior of a series of BnEmBn block copolymers (where B represents polyoxybutylene and E represents polyoxyethylene) in aqueous solution were studied using Tube inversion, SAXS, Optical microscopy, Light Scattering and Rheology. The B block is known to provide a unit of enhanced hydrophobicity. The solubility of the block copolymers decreases with increasing B block length, and with decreasing E block length. The phase diagrams of such systems were constructed. The various phases were recognised by their typical appearance under polarised light microscopy and by their peak ratios in the SAXS patterns. Clouding complicated the phase diagrams, which can be attributed to micellar bridging which causes an attractive interaction between micelles.

A software system for rigid body modelling of solution scattering data (software demonstration)

M.B. Kozine , D.I. Svergun *.

EMBL Hamburg Outstation, Notkestrasse 85, D-22603 Hamburg, Germany.

*Institute of Crystallography, Leninsky prospekt 59, 117333 Moscow, Russia.

A computer system for rigid body modelling against solution scattering data is presented. Fast algorithms to compute scattering from a complex of two arbitrary positioned subunits are implemented and integrated into 3D graphics program. Mutual positions and orientations of subunits (represented by low-resolution envelopes or/and by atomic models) can be determined automatically or interactively fitting the experimental scattering curve from the complex. Applications to the quaternary structure studies of some proteins are demonstrated.

X-ray fibre diffraction from F-actin at Spring-8

Toshiro Oda[1,2], Kouji Makino[2], Kazuya Hasegawa[3], Keiichi Namba[3,4] & Yuichiro Maéda[2]

[1].Max Planck Institute for medical research Jahnstrasse 29, D-69120 Heidelberg, Germany

[2].RIKEN Harima Institute at Spring-8 1-1-1 Kouto, Mikazuki, Sayo, Hyogo, 679-5198, Japan

[3].Protonic Nano-machine project, ERATO, JST 3-4, Hikaridai, Seika, Kyoto, 619-0237, Japan

[4].International Institute for advanced research, Matsushita Electric Industrial Co LTD. 3-4, Hikaridai, Seika, Kyoto, 619-0237, Japan

Actin, one of the most conserved and abundant proteins in living cells, is helically assembled into filaments (F-actin) that play the most crucial roles in events such as cell division and cell motility. F-actin has been pointed out to be a flexible filament and to have an ability of propagating structural changes along its axis. However the biophysical and biochemical meanings of these structural properties have not yet been made clear. The aims of our study are to make clear the architecture of the flexible filament with multiple conformations sensitive to the environments, and finally to find the biological significance of these properties. We have used X-ray fibre diffraction to solve the high-resolution structure of the F-actin filament. As the specimen for the method, preparation of well-oriented F-actin filament sols is essential, because the filament orientation strongly influences the validity and quality of the results. First, factors governing the filament orientation in sols were studied. The sensitive factors were found to be the filament length and the ionic strength of sols. As the practical procedures, concentration of the filaments using low speed centrifugation and application of a strong magnetic field (13.5 Tesla) worked well. Taking these factors into account, well-oriented F-actin sols were prepared, and diffraction patterns were recorded with angular distributions of filaments less than 2°. The resolution limit to which the layer-line amplitudes can be extracted from diffraction patterns is dependent on the angle of disorientation as well as the property of the diffraction camera, such as the size of the X-ray beam, its divergence, its monochromatism, and spatial resolution of the detector. Synchrotron radiation generated by undulater produces an ideal beam in all of these aspects. We collected fibre diffraction patterns using a SPring-8 beam line, BL41XU. Since this beam line is designed specifically for protein crystallography, we made a slight modification: we attached a four way guard slit to the collimator and installed a small beam stop with a helium chamber. The size of the beam was 0.1 mm x 0.1 mm and its wavelength was 1 Å. We used an image plate detector (Rigaku RAXIS-IV). Diffraction patterns of high quality, comparable to those obtained with an exposure time of 10 hours by using the Yale mirror optics on a generator, FR-C (50 kV, 70 mA), were obtained with an exposure time of 5 second. The obtained diffraction patterns showed sharp layer-lines and a very low background intensity as expected. Short exposure of strong X-ray may be advantageous in obtaining high quality diffraction patterns from oriented filament sols. We might be able to extract layer-line intensities from the diffraction patterns from F-actin out to 10 Å resolution.

The Origin of Specific Changes of Small-Angle X-ray Diffraction Pattern of hair and their Correlation with the Element Content

A.A. Vazina[1], P.M. Sergienko[1], V.S. Gerasimov[1], N.F .Lanina[1], A.M. Aksirov[1], V.N. Korneev[2], G.N. Kulipanov[3], N.A. Mezentsev[3], V.I. Kondratyev[3], V.A. Trunova[4], B.P .Tolochko[5], V.P. Letyagin[6]

(1) Institute of Theoretical and Experimental Biophysics RAS, Pushchino, Moscow Region, Russia

(2) Institute of Cell Biophysics RAS, Pushchino, Moscow Region, Russia

(3) Budker Institute of Nuclear Physics SD RAS, Novosibirsk, Russia

(4) Institute of Inorganic Chemistry, SD RAS, Novosibirsk, Russia

(5) Institute of Solid State Chemistry SD RAS, Novosibirsk, Russia

(6) Blokhin Science Center of Oncology Department of Breast Timor, Moscow

The recent correspondence from V.James *et al*., “Using hair to screen for breast cancer” (*Nature*, 1999, 398, 33-34) shows the presence of a diffuse ring in keratin fibres that corresponds to a molecular spacing of 4.44 nm. At least five teams were involved in the attempt to replicate her results. But none of all studies had been able to find the correlation between the diagnostic features mentioned in the “Nature” article and clinical knowledge of the state of patients. X-ray diffraction and fluorescent investigations of human hair with using SR (VEPP-3 Novosibirsk) have shown that the origin of the diffuse ring (4,5 nm) is not “lipid” but most likely glycoprotein. The X-ray patterns were classified into two groups according to the appearance or non-appearance of the diffuse 4,5 nm ring. X-ray patterns with the weak equatorial arc at spacing 4,5 nm were called as “no ring” and those with rings were called as “ring” one. We have shown that X-ray patterns obtained from the near-root segment of hair belong to “no ring” type of patterns always. “No ring” patterns for most donors can be transformed to “ring” patterns via intermediate ones by scanning along the sample point by point from the root region to the tip. In this case the law of conservation of integral intensity for this set of diffraction patterns wasn’t realized. There is a class of donors whose hairs always give X-ray patterns without ring throughout the hair length. We call those diffraction patterns “ring free” patterns. In this case the law of conservation of integral intensity is realized. The X-ray fluorescent element analysis study has shown: there are no changes of element contents along hair for “ring free” type donors; but there are some changes of element contents along the hair from the root region to the tip for donors with “ring” type of hair. For “ring” type of hair the distribution of element content along the hair has bimodal character: the first pool with low element content has a narrow distribution of element concentration, and the distribution for the second pool with higher element content is wider. The correlation between the character of X-ray patterns and the element contents for Ca, Sr and Br was shown: for “no ring” type - low Ca and Sr concentration and high Br concentration; for “ring” type – high Ca and Sr concentration and low Br concentration. We were lucky to show that a prolonged soaking of hairs in 1M $CaCl_2$ at pH 10-11 could transform the hair sample which initially gave a typical “ring free” X-ray pattern in such way that it was able to produce the “ring” X-ray pattern. We propose a two-component structural model of hair tissue, which consists of a flexible component of extracellular matrix (ECM) in series with an inflexible component of keratin intermediate filaments (IF). We have interpreted the weak diffuse arc at spacing 4,5 nm as arising from interference between assemblies of flexible ECM units consisted of glycoproteins that can be either fibrillar and ribbon-like or random-coil in morphology and which have low electron density. Positively charged metals can transform the configuration of glycoprotein chains due to electrostatic interaction with multiple anion groups of polysaccharide chains and this results in the increasing of electron density. So, the interaction between ECM and metals can result in the appearance of intensive diffuse ring on X-ray pattern of hair.

Microphase Separation of Triblock copolymers: Comparison with diblocks

S.C. Turner, A. J. Ryan, S. Mai, J.P.A. Fairclough, C. Booth

University of Sheffield, University of Manchester

Polymer architecture has an important role to play in understanding the microphase separation of these block copolymers. A linear diblock can passes through one interface, whereas triblock copolymers (e.g. AnBmAn or BmAnBm) have to pass through two interfaces or loop twice through the same interface, while cyclic diblock copolymers (c-AnBm) must pass twice through the same interface. Microphase separation of a linear diblock carries a much lower entropy penalty than is the case for the other three architectures. Oxyethylene/oxybutylene triblock copolymers [$B_{n/2}E_mB_{n/2}$ and $E_{m/2}B_nE_{m/2}$, E = oxyethylene, OCH_2CH_2; B = oxybutylene, $OCH_2CH(CH_2CH_3)$] were prepared and characterised in the range f_B = 0.3-0.7 at the University of Manchester. Seven of these systems were seen to exhibit microphase separation in the melt. These microphase separated states were investigated using small-angle X-ray scattering under temperature ramps, in order to determine order-disorder transitions (ODT), disorder-order transitions (DOT) and domain spacings (d-spacings) in the ordered phases.

Programs for Non-linear Modelling of the Small-Angle Scattering Data

Konarev P.V., Volkov V.V., Petoukhov M.V., Svergun D.I*.

Institute of Crystallography, Russian Academy of Science, 117333, Leninsky prospect 59, Moscow, Russia

*European Molecular Biology Laboratory, EMBL c/o DESY, Notkestraße 85, D-22603 Hamburg, Germany

Newly developed programs for non-linear fitting of small-angle scattering data from monodisperse and polydisperse systems are presented. To characterize ordering in partially ordered systems a one-dimensional peak fitting program "PEAK" with graphic interface was written. This program allows one to interactively fit peaks in the scattering curves and yields the Bragg spacing, long-range order dimension, interaction radius, degree of disorder as well as the peak area. The peak is parametrized by a Gaussian function with a constant and linear background and can be fitted both in logarithmic and absolute scale. The analysis of polydisperse multi-component systems (e.g. microemulsions) requires both size and shape fluctuations to be taken into account. The scattering intensity is decomposed into a sum of non-interacting contributions from the particles with different shape (spheres, cylinders, etc.) while the polydispersity and interference effects are considered inside each of these components. This approximation is reasonable at low and medium concentrations of particles in the system. We have developed a program "MIXT", to fit experimental data by scattering from such models and were able to quantitatively describe the composition and parameters of water-in-oil AOT microemulsions in a wide range of temperature, water and salt concentration. Relative volume fractions, average radius and its polydispersity as well as the magnitude of interaction potential for each component were obtained. The program can use spherical, cylindrical and dumb-bell particles and can be applied to various multi-component systems. A 3D display program "COMPLEX" was written to manipulate atomic and low resolution models and coupled with the programs to compute scattering intensity from complex particles and refine their relative positions by fitting the experimental scattering data, either interactively or automatically. The program runs under Windows NT, Windows95, Windows 98.

X-ray and neutron reflection studies of glass surfaces

A.C. Barnes , T Brennen, R.M. Dalgliesh, M. R. Lovell, R. M. Richardson

H H Wills Physics Laboratory, University of Bristol, Tyndall Avenue, Bristol, BS8 1TL

Specular neutron reflection has been used to depth profile water incorporation into float glass surfaces as a function of immersion time. The effective nanometre resolution of the technique, allied with the contrast variation method, has revealed the presence of two layers containing water. The first layer occurs at the glass surface and has a thickness that remains constant at 30 Å under conditions of 100% relative humidity. The second layer penetrates ever deeper into the glass as the time of immersion lengthens, and is accompanied by a loss of material from the glass itself. X-ray reflectivity measurements can also yield useful complementary information about the interfacial regions of many materials and is commonly used as an investigative tool. It is not always possible to make a unique determination of the surface structure from X-ray reflectivity because of the "phase problem" but we have shown that the wide range of reflectivity can enhance the resolution obtained from neutron reflection from gel coated glass. A very useful application of X-rays is to use X-ray induced fluorescence from glass samples to determine the distribution of specific atoms at low concentrations in the surface region. This has been used to investigate the penetration of ions that are believed to enhance durability into the glass surface. In an experiment to determine the sensitivity of this method, a number of Langmuir Blodgett multilayer structures were deposited onto perspex® substrates as a means of constructing a well characterised model system. The structures consisted of 2 layers of behenic acid deposited from pure water subphase followed by a single bilayer of behenic acid deposited from a 0.002M aqueous solution of Manganese Chloride. This single bilayer containing ions that fluoresce on exposure to 1.355 Å X-rays was then progressively buried by subsequent bilayers of behenic acid deposited from a pure water subphase. 3 samples were produced with 2,3 and 4 additional layers on top of the fluorescing layer. The measured fluorescent intensity showed the predicted variation as the manganese layer was progressively buried under more material. The results from ion penetration into glass could then be interpreted.

Recent Fibre Diffraction Studies of Complex Biological Materials using the BioCAT Undulator Beamline at the Advanced Photon Source

Tom Irving

BioCAT, CSRRI & Dept. BCPS Illinois Institute of TechnologyChicago IL USA

The combination of high flux and low angular divergence of undulator radiation from third generation synchrotron sources make them nearly ideal for studies of complex biological materials which typically involve small, weakly diffracting specimens and for dynamic studies of such systems. The BioCAT facility at the Advanced Photon Source (which has just finished its commissioning period and is now accepting outside users) uses highly demagnifying focussing optics with this kind of source to achieve very high flux densities (> 5 x10^{15} ph s^{-1} mm^{-2}) and very small focal spot sizes (< 0.04mm x 0.2 mm) which allow collection of very high quality diffraction patterns in very short times. I will give various examples of experiments that have been done which demonstrate how this new beamline has enabled new and interesting science to be done.

Highly constrained scattering modelling fits using crystal structures

Stephen J. Perkins

Department of Biochemistry and Molecular Biology, Royal Free and University College Medical School, University College London, Rowland Hill Street, London NW3 2PF, U.K.

If solution scattering data can be used to derive molecular structures, this would represent a major enhancement of the utility of this structural technique for biologists. Accordingly procedures for the extraction of molecular structures from X-ray and neutron solution scattering curves and from sedimentation coefficients by analytical ultracentrifugation will be discussed. If atomic structures are known for fragments or subunits of the large macromolecule to be investigated, these provide powerful constraints for determining what turns out to be a limited number of arrangements of these fragments or subunits within the macromolecule that are compatible with the scattering data. A good example of the possibilities offered by these modelling analyses is given by the structural analysis of IgA1 antibody. Human immunoglobulin A (IgA) is an abundant antibody that mediates immune protection at mucosal surfaces as well as in plasma. The IgA1 isotype contains two four-domain Fab fragments and a four-domain Fc fragment linked by a glycosylated hinge region made up of 23 amino acids from each of the heavy chains. Automated X-ray and neutron curve fit searches were based on homology models for the Fab and Fc fragments and hinge peptide models created by molecular dynamics. A three-dimensional search based on these identified a limited family of only about 100 IgA1 structures from 12,000 trial structures that gave good curve fits to the experimental data. These structures contained extended hinges of length about 7 nm that positioned the Fab-to-Fab centre-to-centre separation 17 nm apart while keeping the corresponding Fab-to-Fc separation at 9 nm. This shows that IgA1 has an extended T-shaped structure that is distinct from IgG antibody structures previously determined by scattering and crystallography. Other examples will be discussed, where in particular scattering modelling is able to extend the understanding of newly-determined crystal structures.

SAXS Study on Agglomeration of Nano-$MgAl_2O_4$ Spinel from Micro-Emulsion and CVD Techniques

Rudolf Winter, Michael Quinten, Andrea Dierstein, Rolf Hempelmann, Andreas Altherr, Michael Veith

Physikalische Chemie, Universitat des Saarlandes, Saarbrucken, Germany

Anorganische Chemie, Universitat des Saarlandes, Saarbrucken, Germany

Department of Physics, University of Wales Aberystwyth, Aberystwyth, Wales, UK

Nanocrystalline $MgAl_2O_4$ spinel has been prepared via a micro-emulsion synthesis route and via chemical vapour deposition. For both materials, the size and size distribution of primary particles and agglomerates and their dependence on several synthesis parameters have been determined by small-angle X-ray scattering. In both cases, the primary crystalline particles show a median diameter of well below 10nm. Contrary to XRD, in SAXS agglomerates also contribute to the scattered intensity. Therefore, we obtain scattering patterns which are consistent with a bimodal mixture of primary and agglomerate particles. The micro-emulsion route particles show a smaller particle size with slightly narrower distribution than those prepared by CVD; the agglomerates behave in the opposite manner.

X-ray Scattering from Ion Containing Polymers

T.A.Waigh[1], C.E.Williams[2], G.Grubel[3], A.Roberts[3]

[1] Polymers and Complex Fluids, University of Leeds, Leeds, LS2 9JT, UK.

[2] College de France, 11 Place Marcelin Berthelot, Paris 75005, France.

[3] ESRF, BP220, F-38043 Grenoble, France

We consider the application of X-ray scattering to two separate ion containing systems: polyelectrolytes in poor solvents and ionomeric micelles. The static incoherent X-ray scattering provides evidence for the Rayleigh charge instability in semi-dilute solutions of highly charged flexible polyelectrolytes in poor solvents. Preliminary data will be presented for the use of X-ray photon correlation spectroscopy with ionomer micelles to study their structural arrest transition at high volume fractions.

Combined X-Ray Small-Angle and Wide-Angle Scattering on Fibres with a Microbeam

Martin Mueller, Manfred Burghammer and Christian Riekel

European Synchrotron Radiation Facility, B. P. 220, F-38043 Grenoble Cedex, France

Fast scanning microdiffraction using a synchrotron radiation X-ray beam is a novel technique, which provides information about the nanostructure of a material with microscopic position resolution [1]. At the ESRF Microfocus Beamline (ID13) the undulator x-ray beam is focussed by an ellipsoidal mirror to a size of about 40 microns in diameter. With collimators, spot sizes of 5 or 10 microns at sample position are obtained. Alternatively, further focussing with a tapered glass capillary produces a 2 micron beam. A high-precision DC motor x/y translation stage allows one to perform two-dimensional scans of areas on the sample, which have been selected in advance using a calibrated optical microscope. With this set-up, experiments providing simultaneously information on two length scales are possible: (1) The sample can be scanned on the micron scale, corresponding to optical microscopy. (2) Each recorded diffraction diagram contains information on crystallographic parameters such as cell parameters, crystal size, or orientation. Introducing an additional pinhole for background reduction, simultaneous recording of small-angle and wide-angle scattering patterns on a single high-resolution CCD detector becomes possible [2]. Thus, a third intermediate length scale is accessible: (3) Mesoscopic particle and/or pore sizes as well as their shape and orientation are obtained in the same experiment [3]. Furthermore, the scattering experiments can be easily combined with X-ray fluorescence measurements. The scanning technique described is very suitable for investigations of hierarchically structured materials like polymers. Applications ranging from polymer science through high-tech carbon fibres to native cellulose fibres will be presented. The perspectives of further reducing the beam size into the sub-micrometer region are currently under investigation. In the instrumental set-up, stepping motors have to be replaced by piezo devices. Results of first experiments in the 100 nm range will be shown.

[1] C. Riekel, *Rep. Progr. Phys*. 63, 233-266 (2000)
[2] C. Riekel et al, *J. Appl. Cryst*., SAS99 proceedings, in press.
[3] M. Mueller et al, *J. Appl. Cryst*., SAS99 proceedings, in press

Modeling and analysis of disorder in fibrous systems

R.P. Millane, A. Goyal and J.L. Eads

Whistler Center for Carbohydrate Research and Computational Science and Engineering Program Purdue University West Lafayette, IN 47907-1160 USA

Natural and synthetic fibrous materials are by their very nature disordered. The disorder is often related to the functional properties of the material, and allways affects its X-ray diffraction patterns. Modeling of disorder and calculation of diffraction from such models is therefore useful in studying these materials and in analysis of their diffraction data for structure determination. Specimens that are either fully crystalline or fully non-crystalline are the easiest to deal with, since diffraction from model structures is easily calculated. For cases of intermediate order, where the molecules pack in disordered crystallites, the relationship between the structure and the diffraction data is more complicated and depends on the type and degree of disorder present. These effects are not usually accounted for in structure determination. Models of disordered polycrystalline fibers, methods for calculating their diffraction, and applications to some biopolymers will be described. Results of analysis of images of myosin filament thin sections from frog sartorius muscle (from Luther and Squire) used to study superlattice structure will also be described.

The three dimensional molecular packing structure of native type I collagen

Joseph P.R.O. Orgel*, Andrew Miller*, Tom Irving^, Robert Fischetti^, Andrew P. Hammersley**, and Tim J.Wess*.

* Department of Biological Science, University of Stirling, UK.

^ Advanced Photon Source, Argonne National Laboratory, USA.

** European Synchrotron Radiation Facility, Grenoble, France.

Collagen is the most abundant protein in mammals where it functions as the main component of the connective tissues which maintain the structural integrity of the organism. Until now, our understanding of the three dimensional molecular packing of collagen within the collagen fibril has come from modelling, based on the X-ray diffraction and electron microscopy evidence. From a recent structural solution to the phase problem of the meridional section of the fibre diagram, the conformation of the non-helical telopeptides, and the length of the telopeptide containing segment have been determined using 124 of the 140 meridional orders observed (Orgel *et al* 2000). This one dimensional study has formed the basis upon which to attempt a much more ambitious project; the separation of the overlapping Bragg reflections of the equatorial diffraction pattern of collagen, so that the phase component of the structure factors could be determined using isomorphous addition. Each collagen molecule consists of 4 segments of length D (~67nm) and a fifth of length 0.46D. Segments 1 and 5 contain the non-triple helical telopeptides which are sites of intermolecular crosslinking and which provide the structural integrity and strength of the fibrils. In the X-ray fibre diffraction pattern, the strong near-equatorial reflection at a spacing close to that expected from near neighbor molecules, was shown to be split into three strong components and this suggested a quasi-hexagonal packing of collagen molecules (Hulmes and Miller 1979). In the work presented here, we have measured the intensities of the equatorial and meridional diffraction pattern, which were then corrected for the cylindrical disorientation in reciprocal space and scaling of the native and derivative amplitude sets. These values were used to calculate the phases corresponding to each of the amplitudes and, by Fourier transformation, to calculate the electron density map. This electron density map, and the difference Fourier maps have enabled us to identify the crosslink forming molecular segments. Therefore, in addition to demonstrating the quasi-hexagonal nature of the molecular packing and orientation of the molecules relative to the unit cell axis, we have also been able to identify the key role of the telopeptide containing molecular segments in maintaining the integrity of the molecular packing structure.

[1] Orgel *et al* (2000). *Structure*. 8, 137-142
[2] Wess et al (1998). *J. Mol. Biol.* 275, 255-267.
[3] Bailey et al (1980). *Nature*. 288, 408-413 [4] Hulmes and Miller (1979). *Nature*. 282, 878-880.

Mechanical behaviour of hard alpha-keratin fibre, an X-ray diffraction study

L. Kreplak, F. Briki, J. Doucet

LURE Centre universitaire Bât. 209D, B.P. 34, 91898 Orsay Cedex, France.

Hard alpha-keratin is a protein from the intermediate filament family. The main function of these filaments is to ensure the mechanical support of the cell or of biological tissues such as skin and hair [1]. Moreover, they share a common molecular and supramolecular structure. Our aim is to correlate these structural levels with the outstanding mechanical properties of the keratin filaments. In hard alpha-keratin fibres such as hair or wool, the keratin filaments, called microfibrils, are cylindrical shaped (7.5 nm in diameter), close packed assemblies of long heterodimeric keratin molecules characterised by a double stranded α-helical coiled coil central domain [2]. Laterally the microfibrils are embedded in a sulphur-rich protein matrix forming an hexagonal paracrystal [3]. In this study, we have performed mechanical experiments combined with WAXS and SAXS. We present the mechanical stretching effects on the microfibril structure. We have observed an elastic behaviour of the coiled coil structure at low strain (beyond 3%), followed by a progressive unravelling of the coiled coil domains at higher strains. We have also observed a common behaviour of the coiled coil content, the mean distance between protein chains and the microfibril radius. The three parameters decrease with strain. Finally we show that the direct alpha-helix to beta-sheet transition postulated by previous workers [4] is not valid for our experiments which were done at low humidity conditions. Hence we propose another molecular model of keratin fibre deformation which is based on an alpha-helix to coil transition.

[1] D. A. D. Parry & P. M. Steinert, *Intermediate Filament Structure*, Springer – Verlag (1995).
[2] R. D. B. Fraser & T. P. MacRae, *Nature*, 233,138-140 (1971).
[3] F. Briki, B. Busson, & J. Doucet, *Biochimica et Biophysica Acta*, 1429, 57-68 (1998).
[4] E. G. Bendit, *Textile Research*, Journal, 30, 547-555 (1960).

Forthcoming Meetings

10th Annual Fibre Diffraction and Non-Crystalline Diffraction Workshop

June 13-15, 2001, University of Stirling

(Organised by Matthew Rodman and Trevor Forsyth)

[For further information and registration, see the web pages at

http://www.srs.dl.ac.uk/CCP13

or contact m.j.rodman@dl.ac.uk]

3rd Alpbach Workshop on Fibrous Proteins: "Coiled-Coils, Collagen and Co-Proteins"

September 16-21, 2001, Boglerhof Hotel, Alpbach, Austria

(Organised by David Parry, John Squire and Bob Goldman)

[Details from Prof. John Squire j.squire@ic.ac.uk, 0207 594 3185]

DARTS Bursaries

DARTS at Daresbury Laboratory has funded several bursaries for PhD students to attend the 10th Annual Fibre Diffraction and Non-Crystalline Diffraction Workshop at the University of Stirling (see above and inside back cover). These bursaries will cover the cost of accommodation and registration and may include a contribution to travelling expenses. An application for a bursary can be made through the web pages at

http://www.srs.dl.ac.uk/CCP13

All bursary applications must be accompanied by the submission of a poster abstract to the Workshop.

Fibre Diffraction Review: Instructions to Authors

Submitted original papers, comments/letters or meeting reports for inclusion in *Fibre Diffraction Review* are welcome.

Original Papers:

Suitable topics include technical developments (software or hardware) and new results from fibre diffraction or small-angle scattering experiments (using either X-rays or neutrons).

All papers will be refereed by at least two people (from the CCP13 Committee or their nominated referees) and may be either (a) accepted as they stand, (b) returned for rapid revision, or (c) rejected.

Meeting Reports:

Fibre Diffraction Review includes reports on relevant meetings and conferences which include an element of fibre diffraction or small-angle scattering and which will be of general interest to our readers. Such reports will often be solicited by the Editor from known meeting participants. Other potential contributors to this part of the journal should contact the Editor prior to writing their report.

Comments/Letters:

Feedback from readers about CCP13, the NCD community and about the Journal itself are welcome. These could be in the form of comments or letters to the Editor. Suitable contributions will be published in the Journal.

Advertisements:

Industrial/commercial adverts of interest to our readers are welcome. Potential advertisers should contact the Editor for details of current rates.

Submission:

Contributions should be sent to the Editor before the annual deadline (November 30th) for each issue. Contributions submitted after this date will be returned. Colour illustrations are welcome. Contributions should be submitted both in hardcopy (THREE complete copies) to the Editor and in electronic format to m.j.rodman@dl.ac.uk. Text should be in Word 6 format and illustrations should be submitted as separate files in TIFF format. The December 1999 edition of *Fibre Diffraction Review* should be used as a style-guide and can be viewed at: http://www.clrc.ac.uk/Publications/FibreDiffractionReview/Issue8/index.asp.

Reprints:

Currently it is cheaper to reproduce the whole Journal than to prepare separate reprints of each article. Those wishing to purchase multiple extra copies of the Journal at the prices detailed below should specify this when their article is submitted. Non-contributors who wish to purchase extra copies of the Journal may do so on the same terms as above by contacting the Editor before the November 30th deadline.

Extra copies:

1 copy	£10
5 copies	£40
10 copies	£60
20 copies	£100
30 copies	£140
50 copies	£200
100 copies	£300

(prices include postage and packing)

Editor's Address:

Professor John M. Squire,
Editor, *Fibre Diffraction Review*,
Biological Structure and Function Section,
Biomedical Sciences Division,
Imperial College of Science, Technology and Medicine,
London SW7 2AZ.

e-mail: j.squire@ic.ac.uk
voicemail: 0207 594 3185
FAX: 0207 594 3169

10th Annual Fibre Diffraction and Non-Crystalline Diffraction Workshop

13th-15th June 2001

University of Stirling

Speakers include:

S. Arnott FRS	ICRF / Imperial, UK
D.J. Blundell	Keele, UK
J. Bordas	Barcelona, Spain
O. Byron	Glasgow, UK
R. Chandrasekaran	Purdue, USA
A. Donald FRS	Cambridge, UK
M. Ferenczi	Mill Hill, UK
V.T. Forsyth	ILL, France / Keele, UK
P. Fratzl	Leoben, Austria
G. Fragneto	ILL, France
S. Hanna	Bristol, UK
H. Jakob	Bruker AXS, Austria
S. King	ISIS, UK
P. Laggner	Graz, Austria
K. Meek	Cardiff, UK
A. Miller	Stirling, UK
G. Mitchell	Reading, UK
K. Namba	MEIC, Japan
R. Register	Princeton, USA
C. Riekel	ESRF, France
G. Sankar	Royal Institution, UK
T. Wess	Stirling, UK

For further information and registration, see the web pages at http://www.srs.dl.ac.uk/CCP13 or contact m.j.rodman@dl.ac.uk

(supported by CCP13, DARTS and Daresbury Laboratory)

Useful World Wide Web addresses (URL)

CCP13	**http://www.srs.dl.ac.uk/CCP13**
NCD	**http://www.srs.dl.ac.uk/NCD**
SRS	**http://www.srs.dl.ac.uk**
DARTS	**http://www.darts.ac.uk**

ISSN 1463-8401